12-2020

Analytic Guidance Strategies for Passively Safe Rendezvous and Proximity Operations

Simon Shuster
Utah State University

ANALYTIC GUIDANCE STRATEGIES FOR PASSIVELY SAFE RENDEZVOUS AND PROXIMITY OPERATIONS

by

Simon Shuster

A dissertation submitted in partial fulfillment
of the requirements for the degree

of

DOCTOR OF PHILOSOPHY

in

Aerospace Engineering

Approved:

David Geller, Ph.D. Major Professor	Stephen Whitmore, Ph.D. Committee Member
Geordie Richards, Ph.D. Committee Member	Matthew Harris, Ph.D. Committee Member
Jacob Gunther, Ph.D. Committee Member	D. Richard Cutler, Ph.D. Interim Vice Provost of Graduate Studies

UTAH STATE UNIVERSITY
Logan, Utah

2020

ABSTRACT

Analytic Guidance Strategies for Passively Safe Rendezvous and Proximity Operations

by

Simon Shuster, Doctor of Philosophy

Utah State University, 2020

Major Professor: David Geller, Ph.D.
Department: Mechanical and Aerospace Engineering

A safety ellipse is a type of relative motion trajectory that is commonly used for unmanned rendezvous and proximity operations. As the name suggests, safety ellipses are passively safe relative motion trajectories, which means that their natural motion inherently maintains a low collision risk. The focus of this dissertation is the derivation, analysis, and application of guidance strategies that reconfigure, establish, and exit a safety ellipse. The guidance strategies consist of a set of Δv vectors and impulse times, all written in closed form. Through applications of optimal control theory and parameter optimization, it is shown that these maneuver sequences are fuel optimal for a range of practical safety ellipse reconfiguration, establishment, and exit scenarios. It is also shown that the resulting transfer trajectories remain passively safe across the same range of scenarios.

(179 pages)

PUBLIC ABSTRACT

Analytic Guidance Strategies for Passively Safe Rendezvous and Proximity Operations

Simon Shuster

A safety ellipse is a type of relative motion trajectory that is commonly used for unmanned rendezvous and proximity operations. As the name suggests, safety ellipses are passively safe relative motion trajectories, which means that their natural motion inherently maintains a low collision risk. The focus of this dissertation is the derivation, analysis, and application of guidance strategies that reconfigure, establish, and exit a safety ellipse. The guidance strategies consist of a set of Δv vectors and impulse times, all written in closed form. Through applications of optimal control theory and parameter optimization, it is shown that these maneuver sequences are fuel optimal for a range of practical safety ellipse reconfiguration, establishment, and exit scenarios. It is also shown that the resulting transfer trajectories remain passively safe across the same range of scenarios.

ACKNOWLEDGMENTS

I first and foremost thank my adviser, Dr. David Geller. Dr. Geller is humble, approachable, and has an infectious excitement for solving math problems–an ideal set of traits for a mentor in aerospace engineering. I'm grateful for his generous support and vibrant sense of humor.

I thank Dr. Matt Harris, Dr. Alan Lovell, and Dr. Shane Robinson, who have all had a distinct impact on my growth as an academic and problem solver.

Lastly, I thank my family and friends for their love and encouragement.

Simon Shuster

CONTENTS

LIST OF TABLES

LIST OF FIGURES

CHAPTER 1

INTRODUCTION

When a spacecraft maneuvers itself near another satellite to perform rendezvous and proximity operations (RPO), the trajectory it follows is often determined by the objectives and constraints of the mission. For example, there are a standard set of approach strategies for spacecraft that ultimately dock with the International Space Station [1–3]. For missions where the satellite of interest cannot actively communicate, requires a visual inspection, or is otherwise less conducive to RPO, a common approach procedure involves the spacecraft first establishing a relative motion trajectory called a safety ellipse [4–7]. Safety ellipses are passively safe relative motion trajectories, which means that their natural motion inherently maintains a low collision risk. Also, safety ellipses can be configured to circumnavigate the satellite of interest, making them well-suited for optical navigation and inspection.

Once a safety ellipse is established, the mission may then call for it to be reconfigured, thereby requiring changes to the relative motion trajectory. The problem of determining a series of maneuvers to bring a spacecraft from its current trajectory to a desired trajectory is generally referred to as spacecraft guidance. In addition to achieving the desired safety ellipse, viable maneuver sequences for safety ellipse transfers must be both fuel efficient and able to generate transfer trajectories that are also passively safe.

Current relative motion guidance algorithms that minimize propellant consumption and enforce safety-of-flight constraints rely on numerical optimization techniques [8–12]. These optimization problems are formulated in such a way that a solution can be efficiently computed. However, analogous to solving a nonlinear differential equation with numerical integration, the solution is specific to a particular set of boundary conditions and transfer times, and changing any of these values requires repeating the numerical solution process. The solution may also be sensitive to other factors such as discretization step size and numerical scaling.

The focus of this dissertation is the derivation, analysis, and application of analytic solutions for maneuver sequences that reconfigure, establish, and exit a safety ellipse. There are two main reconfiguration types, and they are referred to as *resizing* and *phasing*. Resizing involves changing the safety ellipse's dimensions, and phasing involves changing the spacecraft's location along the safety ellipse. The term *general reconfiguration* is used to describe a reconfiguration that combines elements of resizing and phasing, as well as any other desired changes. Mathematically, a general reconfiguration also encompasses establishing a safety ellipse, referred to as *ingress*, and exiting a safety ellipse, referred to as *egress*.

The solutions consist of closed-form expressions for the maneuver times and impulsive thrust vectors, which are more commonly known as Δv vectors. Through applications of optimal control theory and parameter optimization, it is shown that these maneuver sequences are fuel optimal (in the sense of minimizing total Δv) for a range of practical resizing, phasing, ingress, and egress scenarios. Although it is not mathematically proven, there is strong empirical evidence to suggest that the maneuver sequences are in fact globally optimal. It is also shown that the resulting transfer trajectories remain passively safe across the same range of scenarios.

The development of these maneuver sequences is somewhat unconventional in that it neither computes a solution directly from an optimization problem, nor enforces explicit path constraints to ensure passive safety. Instead, a solution is effectively hypothesized, and analysis is performed to determine when it is both optimal and passively safe. This analysis is performed analytically for *nominal* reconfigurations, which refer to simplified reconfiguration scenarios that isolate a desired change to the safety ellipse. For example, a nominal resizing scenario involves only changing the safety ellipse's dimensions, while an *off-nominal* resizing scenario involves correcting other aspects of the safety ellipse in addition to changing its dimensions (where the corrections are small relative to the size change). The maneuver sequence expressions are much more complex for off-nominal scenarios, making analytic analysis unwieldy. As a result, for off-nominal reconfigurations, optimality and passive safety are analyzed using Monte Carlo methods.

Since the guidance strategies involve relative orbital motion, a model of relative motion dynamics must be assumed. This work uses the Hill-Clohessy-Wiltshire (HCW) equations [13, 14]. Although these equations are considered to be low-fidelity in comparison to other relative motion models [15], they still provide an adequate approximation of the underlying dynamics for near-circular orbits, especially over short propagation times. The maneuver sequences require at most two orbital periods to complete, so a reasonable level of accuracy is retained. In fact, a chapter of this dissertation is dedicated to analyzing the performance of the HCW-based guidance strategies within a nonlinear orbit environment.

Optimal trajectory design using the HCW equations and impulsive maneuvers is a well-studied problem [12, 16–21]. However, to the author's knowledge, analytic solutions have only been proposed by Prussing [16, 17], Jezewski and Donaldson [18], and Ichimura and Ichikawa [21]. The solutions developed by Prussing are restricted to problems with in-plane motion and specific boundary conditions (circle-to-circle rendezvous). Jezewski and Donaldson first assume that the maneuver sequence consists of two impulses that occur at the initial and final times and then solve for the time between them that minimizes the combined Δv. By assuming two impulses, this solution overlooks other possible transfer trajectories that require less Δv. Also, although the authors claim the method is analytic, an iterative approach is needed to completely solve for the optimal solution time. Ichimura and Ichikawa effectively solve a safety ellipse resizing problem; however, they decouple in-plane and out-of-plane maneuvers, which does not truly minimize the total Δv.

The key contribution of this work is closed-form solutions for passively safe transfers between safety ellipses with Δv requirements that are equal or comparable to solutions that rely on numerical optimization methods. These proposed solutions offer a clear advantage in terms of computational efficiency. More importantly, they provide a better understanding of optimal safety ellipse transfers by showing how the maneuver locations, directions, and magnitudes depend on properties of the initial and final safety ellipses. A mission planner or operator may not directly apply the equations developed in this work, but could certainly find them valuable for informing their RPO trajectory design.

CHAPTER 2
BACKGROUND AND RELATED WORK

2.1 Rendezvous and Proximity Operations

Rendezvous and proximity operations (RPO) generally refers to the process of bringing two or more satellites near each other for the purposes of maintaining a formation, initiating a docking/attachment sequence, or conducting on-orbit activities such as inspection. RPO dates back to the mid 1960s where it played a crucial role in the space race between the Soviet Union and United Sates [22]. In more recent years, robotic (unmanned) missions involving RPO for formation flying, on-orbit servicing, and active debris removal have gained increased commercial and government interest [23, 24]. Notable upcoming missions include Restore-L [25], Robotic Servicing of Geosynchronous Satellites [26], and e.Deorbit [27].

2.1.1 Relative Motion

For RPO guidance, navigation, and control (GN&C), it is usually more convenient to approximate the motion of one satellite with respect to another instead of the motion of both satellites about their central body. The translational dynamics of one satellite with respect to another is called relative orbital motion, or just relative motion when used in the context of RPO. The reference satellite is commonly referred to as the target, chief, or client. This reference "satellite" can also be virtual, meaning that the reference is simply a point moving along a fictitious orbit. The satellite whose motion is described relative to the target is commonly referred to as the chaser, deputy, or servicer.

Relative Reference Frame

Relative motion is expressed in Hill's reference frame [13], also known as the local-vertical, local-horizontal (LVLH) frame; radial, in-track, cross-track (RIC) frame; or radial, tangential, normal (RTN) frame. This frame is shown in Figure 2.1.

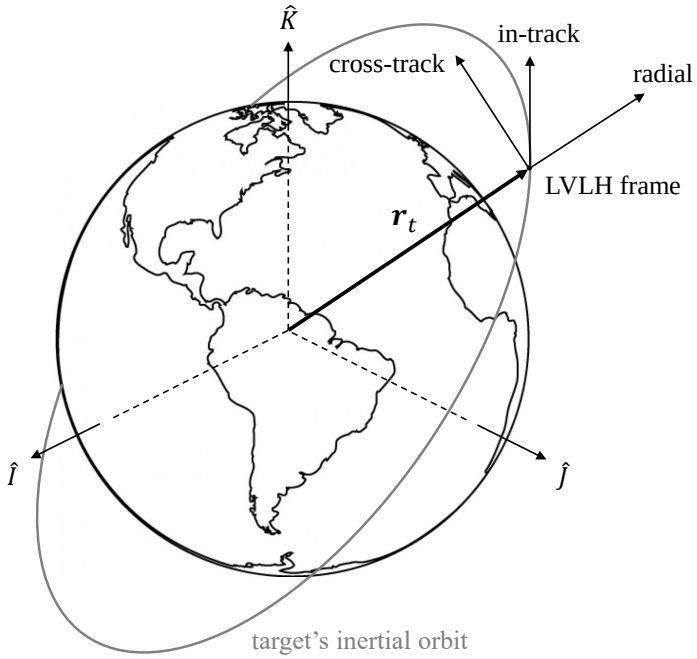

Fig. 2.1: LVLH frame illustration.

The origin of this frame coincides with the target's inertial position vector and moves with the target as it travels along its orbit. The frame's orthogonal basis aligns with the target's inertial position vector (radial), the target's inertial angular momentum vector (cross-track) and the direction that completes the triad (in-track). This means that the frame also rotates as its origin translates about the target's orbit. Mathematically, the frame's basis vectors are written as

$$\text{radial} := \hat{e}_x = \frac{\boldsymbol{r}_t}{\|\boldsymbol{r}_t\|} \tag{2.1}$$

$$\text{cross-track} := \hat{e}_z = \frac{\boldsymbol{r}_t \times \boldsymbol{v}_t}{\|\boldsymbol{r}_t \times \boldsymbol{v}_t\|} \tag{2.2}$$

$$\text{in-track} := \hat{e}_y = \hat{e}_z \times \hat{e}_x \tag{2.3}$$

where $\boldsymbol{r}_t$ and $\boldsymbol{v}_t$ are the target's inertial position and velocity vectors. When the target's orbit is circular, the in-track axis aligns with the target's inertial velocity vector.

Relative Motion Models

Relative motion models are sets of differential equations that describe relative motion. Relative motion modeling is well studied and remains an area of active interest– a survey and analysis published in 2017 documented a total of 27 models [15]. In deriving a relative motion model, assumptions must be made regarding the eccentricity of the target's orbit and the fidelity of the inertial orbital motion. This results in a general trade-off between accuracy and complexity. For a thorough description and performance analysis of the most common relative motion models, consult [15].

Under the assumption of two-body motion, a circular target orbit, and a small separation between the target and chaser relative to their distance from the central body, Clohessy and Wiltshire [14] derived a set of linear time invariant (LTI) differential equations, called the Clohessy-Wiltshire (CW) equations or Hill-Clohessy-Wiltshire (HCW) equations, that describe the motion of a relative position and velocity vector. Violating these assumptions does not immediately invalidate the equations. Instead, the accuracy of HCW motion degrades with the severity in which the underlying assumptions are violated. Although the HCW equations were initially derived for a relative state vector expressed in terms of Cartesian coordinates, it has been shown that the equations maintain their same form for curvilinear relative state representations [28–30].

This research considers relative motion trajectories described by the HCW equations. The main advantage of working with these equations is the convenience of a relatively simple LTI system. Due to its lack of complexity, HCW motion can be represented in a geometrically insightful manner, and this is shown in Section 3.1. Although the HCW equations are considered to be low-fidelity in comparison to other relative motion models [15], they still capture the dominant relative motion dynamics for near-circular target orbits, especially as the total propagation time decreases. Since the guidance strategies proposed in this work occur over at most two orbital periods, these equations retain a reasonable level of accuracy. This is verified in Chapter 11, where the performance of HCW-based guidance algorithms are analyzed within a nonlinear orbit environment.

2.1.2 Passive Safety

In the context of RPO, passive safety refers to a relative motion trajectory that maintains a low collision risk without relying on any maneuvers. Losing the ability to control a spacecraft, whether temporary or permanent, can stem from a faulty thruster system, flight computer reset, power loss, or more general system failure. This work focuses on a particular (short-term) passively safe relative motion trajectory called a safety ellipse.

Safety Ellipses

The term safety ellipse appears to first be documented by Fehse [31]. A safety ellipse is a periodic or near-periodic relative motion trajectory that phases in-plane and out-of-plane motion such that the chaser passes safely above or below the target when the vehicles have the same altitude. Another representation of this type of relative motion phasing is through eccentricity/inclination (e/i)-vector separation [32, 33]. As its name suggests, a safety ellipse is short-term passively safe. Quantifying short-term depends on the orbit environment; D'Amico and Montenbruck showed that the differential perturbations in sun-synchronous LEO cause the relative motion phasing to deteriorate from best-case (passively safe) to worst-case (passively unsafe) over several weeks [33].

A safety ellipse's (near) periodicity allows the chaser to circumnavigate the target, which provides the chaser with lighting conditions of the target that are more consistent than non-periodic relative motion trajectories. This gives safety ellipses the added benefit of being conducive to optical navigation and inspection. Implementing safety ellipses or e/i-vector separation for passively safe RPO has been proposed both conceptually and for real missions. The PRISMA and AVANTI missions, which successfully demonstrated autonomous rendezvous with a noncooperative target, used e/i-vector separation throughout their RPO phases [4–6]. The Restore-L mission will use safety ellipses for its near-field RPO [7]. Naasz [34], Gaylor and Barbee [35], and Barbee et al. [36] have also proposed safety ellipses for RPO missions involving noncooperative targets.

2.2 Relative Motion Guidance

Within a spacecraft's GN&C system, the general task of the guidance function is to compute maneuvers that bring the spacecraft from its current trajectory to a desired trajectory. Relative motion guidance simply implies that the transfer trajectory dynamics are described with a relative motion model.

This work develops guidance schemes that compute impulsive maneuvers. Mathematically, an impulsive maneuver is defined by a Δv vector, which refers to an instantaneous change in the direction and magnitude of the spacecraft's velocity. Physically, an impulsive maneuver approximates the spacecraft's state during a brief firing of its on-board thruster in which its position only slightly changes. This idealization is satisfactory for high-thrust systems with a burn time that is short compared to the coasting time of the spacecraft [37]. Through the ideal rocket equation, Δv can be directly related to the mass propellant consumption [38], which makes Δv a useful metric for analysis and planning.

Like relative motion modeling, relative motion guidance is well-studied and remains an area of active research interest. Sections 2.2.1 and 2.2.2 summarize previous work that is relevant to this dissertation. The previous works are categorized by whether the proposed solutions to their specific problem statements are either optimal or suboptimal.

2.2.1 Suboptimal Solutions

A simplistic yet effective approach to guidance problems with linear relative motion dynamics involves solving an exact system of linear equations for two impulses that occur at specified initial and final times. The linear system is formed by specifying the initial state, desired final state, and transfer time between them. This method is sometimes referred to as two-impulse targeting or Clohessy-Wiltshire targeting [14], after the authors who proposed its approach (in addition to deriving a set of fundamental relative motion equations).

Through a re-parameterization of the HCW equations, Spencer developed guidance strategies for both general rendezvous and common relative motion trajectories [39]. The strategies are based on equations that describe the effects of impulsive maneuvers of elements of the re-parameterized state vector [40]. These equations are presented in Section

3.1.1. In comparison to two-impulse targeting, Spencer's approach has two key advantages: 1) it provides additional geometric insight and more clearly shows how impulses effect characteristics of HCW motion and 2) it introduces the location of the impulse as an unknown variable, which increases the solution space. This work formalizes the theory and generalizes the application of previous papers by Lovell and Tragresser [41] and Lovell et al. [42].

2.2.2 Optimal Solutions

A number of authors have solved relative motion guidance problems using optimization theory. Here, the specific type of optimization problems are further categorized as problems that use optimal control theory, parameter optimization, or other approaches.

Optimal Control

In [16] and [17], Prussing solved trajectory optimization problems involving impulsive maneuvers and HCW dynamics. Solutions are computed using the primer vector, which is a vector whose properties conveniently encapsulate certain necessary conditions for optimality. These papers illustrate the in-plane dynamics of the primer vector to show, conceptually, how three- and four-impulse solutions are formed. The general equations required for constructing these solutions are also presented. Prussing applies this approach to develop analytic solutions for a particular class of rendezvous problems. These problems assume that both vehicles are initially in circular and coplanar orbits.

Jezewski [19] extended the applicability of primer vector theory to show how it can be used to improve the Δv cost of a transfer trajectory. For instance, this work demonstrates how to compute the time and direction of an intermediate impulse to lower the total Δv along a suboptimal transfer. Overall, the paper provides an iterative approach to trajectory planning–for example, it studies how extending the transfer time, allowing for an initial coast phase, and introducing an intermediate impulse affects the Δv of an initial two-impulse transfer for a specific rendezvous scenario.

Parameter Optimization

A more recent approach to optimal guidance is through solving parameter optimization problems, which are formulated by discretizing an optimal control problem. Parameter optimization problems that are cast as convex optimization problem–either directly or iteratively–have become especially popular because they can be efficiently solved. Parameter optimization problems can also readily implement path constraints that enforce, for example, RPO safety-of-flight. Constrained RPO trajectory planning using successive convex optimization has been extensively studied by Liu [11] and Ortolano [12], and these works represent the current state of the art for this particular topic.

Other

In [20], Carter derived necessary and sufficient conditions without relying on optimal control theory; however, the resulting derivations arrive at a primer vector analog. This work, along with other papers by Carter and Brient [43, 44], show that directly solving the general optimal N-impulse problem involving linear dynamics requires solving a system of nonlinear equations that, as the authors note, can be difficult to compute.

Ichikawa and Ichimura [21] developed an analytic maneuver sequence for what is effectively a safety ellipse resizing scenario. However, they make a key simplifying assumption: the maneuver strategy involves separate solutions for in-plane and out-of-plane maneuvers because in-plane and out-of-plane motion is decoupled. With this assumption, they compute optimal maneuver sequences for in-plane and out-of-plane motion separately.

Optimal impulsive reconfigurations have been studied by Chernick and D'Amico [45], Gaias and D'Amico [46], and Wang et al. [47]. These works all consider the relative motion guidance problem in terms of the relative state formulation developed by D'Amico [48], which provides increased fidelity over the HCW equations as it describes both the secular effects of dominant differential perturbations and the effects of a nonzero target eccentricity. To compute optimal solutions, Chernick and D'Amico apply reachable set theory, while Gaias and D'Amico and Wang et al. apply a geometric approach. However, like Ichimura and Ichikawa, these authors all solve the in-plane and out-of-plane problems separately.

CHAPTER 3
SAFETY ELLIPSE MODELING

3.1 Hill-Clohessy-Wiltshire Motion

Safety ellipses are a particular type of relative motion trajectory. In this work, relative motion is described using the HCW equations. The underlying assumptions for deriving these equations are discussed in Section 2.1.1. This section presents the original HCW equations as well as other representations of HCW motion that are especially useful for modeling safety ellipses.

In terms of the convention in equations (2.1) through (2.3) (x = radial, y = in-track, z = cross-track), the HCW equations for unforced motion are:

$$\ddot{x} - 3\Omega^2 x - 2\Omega\dot{y} = 0 \tag{3.1}$$

$$\ddot{y} + 2\Omega\dot{x} = 0 \tag{3.2}$$

$$\ddot{z} + \Omega^2 z = 0 \tag{3.3}$$

where Ω is the mean motion of the LVLH frame. For two-body motion, Ω is constant and given by

$$\Omega = \sqrt{\frac{\mu}{a_t^3}} \tag{3.4}$$

where μ is the gravitational parameter and a_t is the target's inertial semi-major axis.

Equations (3.1) through (3.3) show that in-plane motion is decoupled from out-of-plane (cross-track) motion. Unforced in-plane motion is cycloidal [49]. Unforced out-of-plane motion is a harmonic oscillator.

Use of the HCW equations for both mission planning and on-orbit targeting dates back to the Gemini program from the 1960s [50]. More recently, several authors have introduced more intuitive representations of HCW motion that are used extensively in this research.

3.1.1 Relative Orbital Elements

Lovell and Spencer derived a new set of relative states by re-parameterizing the solutions to the HCW equations [51]. The authors refer to these states as the relative orbital elements (ROEs)–not to be confused with a relative state vector by the same name developed by D'Amico [48]. The ROEs provide a geometric interpretation of relative motion that might not be readily apparent from a relative position and velocity vector. In this sense, the ROEs are analogous to the inertial orbital elements. Figure 3.1 shows the in-plane ROEs with a corresponding relative position vector, $\boldsymbol{r}_{\text{rel}}$.

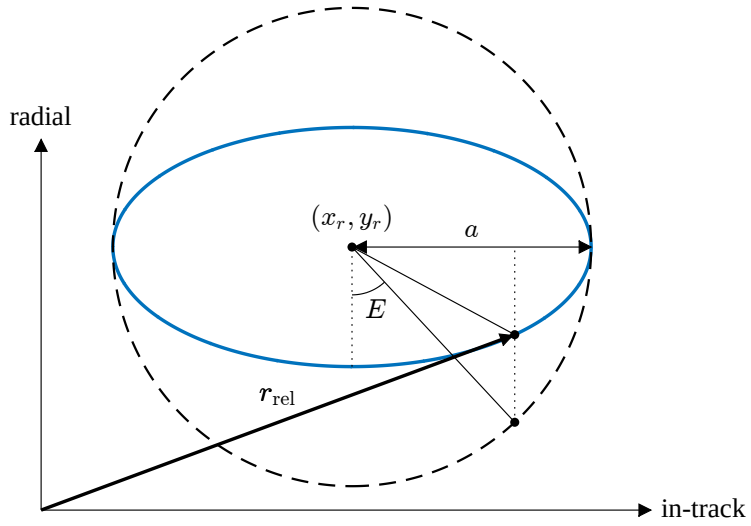

Fig. 3.1: In-plane relative orbital elements.

In-plane motion is characterized as a point moving along an instantaneous ellipse which translates with constant velocity along the in-track axis. The ellipse's semi-major axis is twice the length of its semi-minor axis, and this ratio is invariant. x_r and y_r are the radial and in-track coordinates of the ellipse's instantaneous center, a is the ellipse's in-plane semi-major axis, and E is a relative eccentric anomaly which is defined as the in-plane phase angle. Harmonic out-of-plane motion is parameterized in terms of its amplitude, A, and phase angle, ψ.

The solution to the ROE differential equations for unforced motion are

$$x_r(t) = x_{r_0} \tag{3.5}$$

$$y_r(t) = -\frac{3}{2}(\tau - \tau_0)\, x_{r_0} + y_{r_0} \tag{3.6}$$

$$a(t) = a_0 \tag{3.7}$$

$$E(t) = E_0 + \tau - \tau_0 \tag{3.8}$$

$$A(t) = A_0 \tag{3.9}$$

$$\psi(t) = \psi_0 + \tau - \tau_0 \tag{3.10}$$

where $\tau = \Omega t$. The ROE differential equations become nonlinear when a control input is introduced. From [39, 40], the effects of an impulsive Δv vector on the ROEs are

$$x_r^+ = x_r^- + \frac{2}{\Omega}\Delta v_y \tag{3.11}$$

$$y_r^+ = y_r^- - \frac{2}{\Omega}\Delta v_x \tag{3.12}$$

$$a^+ = \sqrt{\left(a^- \cos E^- + \frac{4}{\Omega}\Delta v_y\right)^2 + \left(a^- \sin E^- + \frac{2}{\Omega}\Delta v_x\right)^2} \tag{3.13}$$

$$E^+ = \text{atan2}\left(a^- \sin E^- + \frac{2}{\Omega}\Delta v_x, a^- \cos E^- + \frac{4}{\Omega}\Delta v_y\right) \tag{3.14}$$

$$A^+ = \sqrt{(A^- \sin \psi^-)^2 + \left(A^- \cos \psi^- + \frac{1}{\Omega}\Delta v_z\right)^2} \tag{3.15}$$

$$\psi^+ = \text{atan2}\left(A^- \sin \psi^-, A^- \cos \psi^- + \frac{1}{\Omega}\Delta v_z\right) \tag{3.16}$$

where '$-$' denotes a quantity immediately before the impulse and '$+$' denotes a quantity immediately after the impulse. The subscript on each Δv component denotes its direction (consistent with the convention in equations (2.1) through (2.3)).

3.1.2 Linear Relative Orbital Elements

Ortolano addressed the ROE control input nonlinearity problem by deriving a new set of states that remain LTI for forced motion yet retain some of the geometric insight from

the ROEs [12,52]. He refers to these states as the linear relative orbital elements (LROEs). The LROEs can be constructed through linear and nonlinear functions of the ROEs or, more importantly, through strictly linear combinations of the relative position and velocity. The LROE state vector is

$$\boldsymbol{x} = \begin{bmatrix} x_r & y_r & a\sin E & a\cos E & A\sin\psi & A\cos\psi \end{bmatrix} \tag{3.17}$$

The subscript 'rel' is dropped for brevity. The linear mapping from the relative position and velocity to LROEs is

$$T_{r,v}^{\text{LROE}} = \begin{bmatrix} 4 & 0 & 0 & 0 & \frac{2}{\Omega} & 0 \\ 0 & 1 & 0 & -\frac{2}{\Omega} & 0 & 0 \\ 0 & 0 & 0 & \frac{2}{\Omega} & 0 & 0 \\ 6 & 0 & 0 & 0 & \frac{4}{\Omega} & 0 \\ 0 & 0 & 1 & 0 & 0 & 0 \\ 0 & 0 & 0 & 0 & 0 & \frac{1}{\Omega} \end{bmatrix} \tag{3.18}$$

The system of differential equations describing the LROE dynamics can be written in standard state-space form:

$$\dot{\boldsymbol{x}} = F\boldsymbol{x} + G\boldsymbol{u} \tag{3.19}$$

where $\boldsymbol{u}$ is the thrust acceleration and

$$F = \Omega \begin{bmatrix} 0 & 0 & 0 & 0 & 0 & 0 \\ -\frac{3}{2} & 0 & 0 & 0 & 0 & 0 \\ 0 & 0 & 0 & 1 & 0 & 0 \\ 0 & 0 & -1 & 0 & 0 & 0 \\ 0 & 0 & 0 & 0 & 0 & 1 \\ 0 & 0 & 0 & 0 & -1 & 0 \end{bmatrix} \quad G = \frac{1}{\Omega} \begin{bmatrix} 0 & 2 & 0 \\ -2 & 0 & 0 \\ 2 & 0 & 0 \\ 0 & 4 & 0 \\ 0 & 0 & 0 \\ 0 & 0 & 1 \end{bmatrix}. \tag{3.20}$$

The solution to equation (3.19) is

$$\boldsymbol{x}(t) = \Phi\left(t, t_0\right) \boldsymbol{x}(t_0) + \int_{t_0}^{t} \Phi\left(t, s\right) G\boldsymbol{u}(s) ds \tag{3.21}$$

where the state transition matrix is

$$\Phi(t, t_0) = \begin{bmatrix} 1 & 0 & 0 & 0 & 0 & 0 \\ -\frac{3}{2}(\tau - \tau_0) & 1 & 0 & 0 & 0 & 0 \\ 0 & 0 & \cos\left(\tau - \tau_0\right) & \sin\left(\tau - \tau_0\right) & 0 & 0 \\ 0 & 0 & -\sin\left(\tau - \tau_0\right) & \cos\left(\tau - \tau_0\right) & 0 & 0 \\ 0 & 0 & 0 & 0 & \cos\left(\tau - \tau_0\right) & \sin\left(\tau - \tau_0\right) \\ 0 & 0 & 0 & 0 & -\sin\left(\tau - \tau_0\right) & \cos\left(\tau - \tau_0\right) \end{bmatrix} \tag{3.22}$$

The LROEs are a particularly useful representation due to their geometric connection to the ROEs and LTI structure. In Chapters 7 through 10, this ultimately allows for analytic expressions that relate a maneuver sequence's necessary conditions for optimality to ROEs of the initial and final safety ellipses. Additionally, numerical validation using convex optimization can be readily applied as a result of the LROE's linear dynamics.

3.2 Safety Ellipse Characteristics

A safety ellipse is defined as an HCW relative motion trajectory with the following properties:

1) Periodic or near-periodic in-plane motion.

2) Nonzero out-of-plane motion.

3) Phasing of in-plane and out-of-plane motion such that the chaser intersects the target's orbit plane near the points of largest radial separation.

Another way of stating property 3 is that a safety ellipse phases in-plane and out-of-plane motion such that the chaser passes above or below the in-track axis near its locations

of largest cross-track separation. The phasing between in-plane and out-of-plane motion defines the safety ellipse's orientation. An example of an ideally oriented safety ellipse, centered about the origin of the LVLH frame, is shown in Figure 3.2.

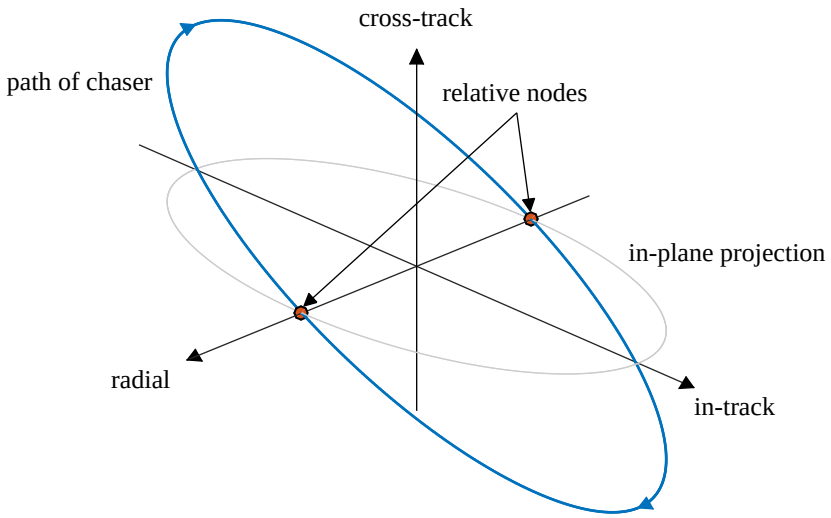

Fig. 3.2: An example of an ideally oriented safety ellipse centered about the LVLH frame.

This orientation is ideal because the location where the altitudes of the chaser and target are equal correspond to the points of largest cross-track separation. Instead of intersecting the in-track axis, the chaser passes above or below it. Among other effects, perturbations within a real-world orbit environment cause the safety ellipse to drift back and forth along the in-track axis; maintaining this orientation greatly reduces the chance of a collision.

The safety ellipse's orientation is described in terms of a relative phase angle, γ, which measures the relative in-plane eccentric anomaly between the negative radial axis and the relative ascending node. The geometry of the eccentric anomaly measurement is identical for γ and E (see Figures 3.1 and A.1). Mathematically, γ is expressed as

$$\gamma = E - \psi \tag{3.23}$$

From equations (3.8) and (3.10)

$$\gamma = E_0 - \psi_0 = \gamma_0 \tag{3.24}$$

Equation (3.24) says that γ is constant for unforced motion. An ideal orientation has $\gamma = 0°, \pm 180°$ (Figure 3.2 shows $\gamma = \pm 180°$).

Figure 3.3 shows a projection of the motion in the radial, cross-track plane for different values of γ. For this illustration, $A/a = 0.5$. The shapes are reflected about the cross-track axis for negative values of γ.

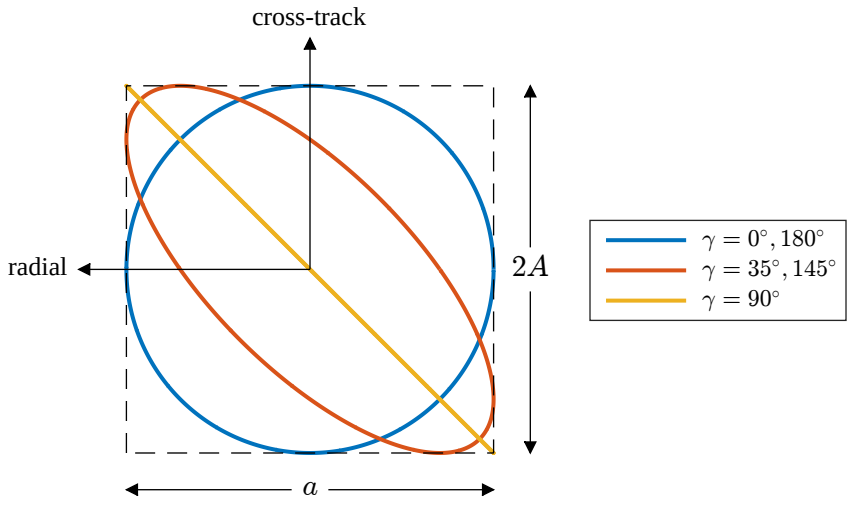

Fig. 3.3: Motion in the radial, cross-track plane for different values of γ.

As γ approaches 90°, the chaser moves closer to intersecting the in-track axis as it passes through the target's orbit plane. This type of trajectory increases the risk of a collision because the chaser lacks cross-track separation when the altitudes of the chaser and target are equal.

Figure 3.3 shows that deviating from an ideal orientation does not immediately negate passive safety. However, perturbations within a real-world orbit environment cause the relative phasing to naturally drift toward an unsafe orientation, so a tolerance is typically

placed on the allowable relative phase angle. For example, for the TanDEM-X/TerraSAR-X formation, corrective maneuvers are performed to keep its relative phase angle analog within roughly 7° of its ideal value [33].

The radial component of the instantaneous center, x_r, dictates whether in-plane motion–and in turn the safety ellipse–is periodic. For $x_r = 0$, the safety ellipse's instantaneous center is stationary and the chaser's motion is completely periodic. This is shown in Figure 3.2. For small nonzero x_r, the resulting trajectory is known as a walking safety ellipse [34], as the safety ellipse gradually drifts along the in-track axis. Figure 3.4 plots an example of a walking safety ellipse.

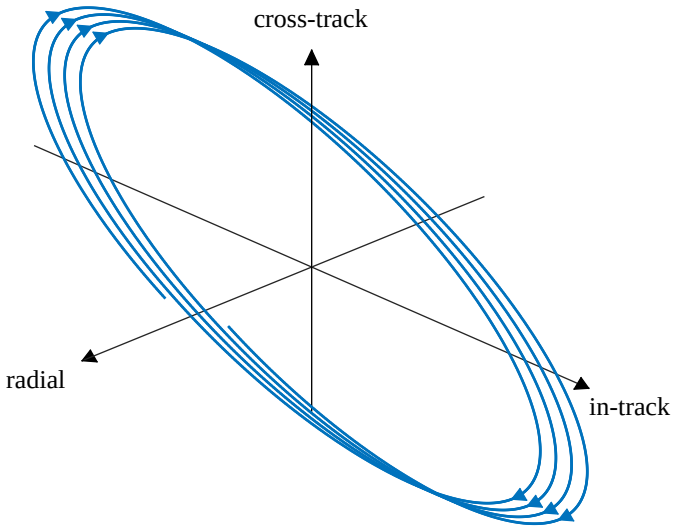

Fig. 3.4: An example of a walking safety ellipse.

The in-track component of the instantaneous center, y_r, describes the safety ellipse's in-track offset. Figure 3.5 plots an example of an offset (and stationary) safety ellipse. Since a walking safety ellipse is inherently offset (except at the instant where $y_r = 0$), the term offset will be reserved for stationary safety ellipses with nonzero y_r, unless otherwise specified.

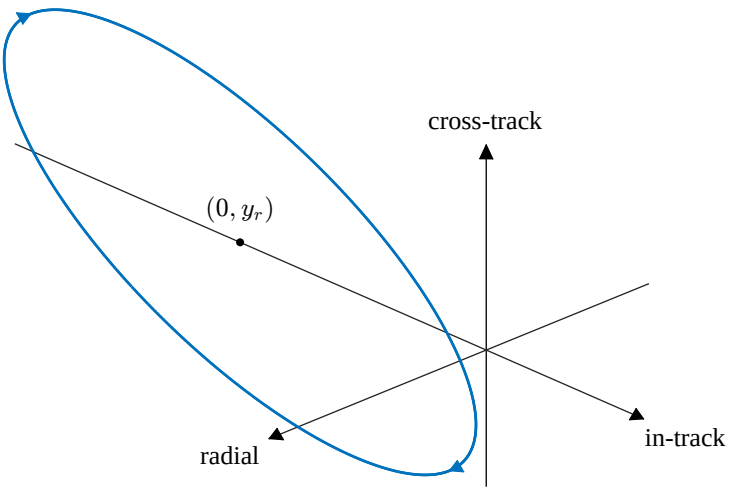

Fig. 3.5: An example of an offset safety ellipse.

To recap, a safety ellipse's degree of passive safety depends on its orientation (γ), its periodicity depends on the radial component of its instantaneous center (x_r), its in-track offset depends on the in-track component of its instantaneous center (y_r), and its dimensions depend on the in-plane semi-major axis (a) and cross-track amplitude (A).

CHAPTER 4
OPTIMAL CONTROL PROBLEM AND SECOND-ORDER CONE PROGRAM FOR A GENERAL RECONFIGURATION

4.1 Optimal Control Problem

Sections 4.1.1 and 4.1.2 formulate and analyze a general safety ellipse reconfiguration in terms of an impulsive optimal control problem. In a broad sense, optimal control theory provides a way of computing the most efficient control function that achieves a desired state given the motion governed by a set of differential equations. Within the context of this work, the objective is to find the minimum total characteristic velocity of a sequence of Δv vectors that brings the chaser from its initial relative motion trajectory to a final desired relative motion trajectory.

Section 4.1.1 formulates an optimal control problem that encompasses safety ellipse resizing, phasing, ingress and egress, as each scenario has the same minimum Δv objective and LTI dynamics. Three sets of terminal constraints are considered. All sets specify the instantaneous center, in-plane semi-major axis, and cross-track amplitude at the final time. One problem specifies desired changes to both the in-plane and out-of-plane phase angles. This is the standard reconfiguration problem that is analyzed in Chapters 7 through 9 for resizing, phasing, and ingress scenarios. A separate set of terminal constraints is formulated for safety ellipse egress. This is because the egress scenarios considered in this work result in phase angles that become undefined after the final maneuver (see Chapter 10). The remaining set of terminal constraints is formulated for a problem that leaves the individual phase angles free but specifies the final relative phase angle. This problem is analyzed in Chapter 7 for a special case of nominal safety ellipse resizing.

Section 4.1.2 presents the necessary conditions for optimality. Some of these conditions are expressed in terms of the primer vector, which is a vector whose properties conve-

niently encapsulate certain necessary conditions. The section concludes with a lemma that shows that an extremal of the fixed-final-time problem is also an extremal of the free-final-time problem. This means that if a maneuver sequence satisfies the terminal constraints, costate dynamics, and primer vector conditions, the necessary conditions associated with the free-time problem are satisfied as well. The lemma remains valid for each set of terminal constraints.

4.1.1 Formulation

A free-final-time optimal control problem is formulated for the general safety ellipse reconfiguration. The cost functional describing propellant consumption over time is

$$J = \int_{t_0}^{t_f} \|\boldsymbol{u}(s)\| ds \tag{4.1}$$

For a control profile with impulsive Δv vectors, the thrust acceleration can be written as

$$\boldsymbol{u}(t) = \sum_{k=1}^{n} \Delta \boldsymbol{v}(t_k)\delta(t - t_k) \tag{4.2}$$

where n is the number of impulses, t_k is the time of the kth maneuver, and $\delta(\cdot)$ is the Dirac delta function. The optimal control problem is

$$\begin{aligned} \text{minimize} \quad & J \\ \text{subject to} \quad & \dot{\boldsymbol{x}} = F\boldsymbol{x} + G\boldsymbol{u} \\ & \boldsymbol{x}(t_0) = \boldsymbol{x}_0 \\ & \boldsymbol{\varphi}(t_f, \boldsymbol{x}(t_f)) = \boldsymbol{0} \end{aligned} \tag{4.3}$$

where F and G are given in equation (3.19). The differential equations must be interpreted in its integrated form since the control is impulsive. As a result, the state jumps at each impulse time. The initial state is constrained to be a fixed point on the safety ellipse, which

is given by

$$\boldsymbol{x}_0 = \begin{bmatrix} x_{r_0} & y_{r_0} & a_0 \sin E_0 & a_0 \cos E_0 & A_0 \sin \psi_0 & A_0 \cos \psi_0 \end{bmatrix}^T \tag{4.4}$$

Constrained Individual Phase Angles

When both the in-plane and out-of-plane phase angles are constrained, there are six terminal constraints:

$$\boldsymbol{\varphi}(t_f, \boldsymbol{x}(t_f)) = \begin{bmatrix} \varphi_1 & \dots & \varphi_6 \end{bmatrix}^T \tag{4.5}$$

These constraints specify the chaser's desired location along the final safety ellipse as a function of the final time. Each scalar constraint is written as

$$\varphi_1 = x_1(t_f) - x_{r_0} - \Delta x_r \tag{4.6}$$

$$\varphi_2 = x_2(t_f) + \frac{3}{2}(\tau_f - \tau_0)\, x_{r_0} - y_{r_0} - \Delta y_r \tag{4.7}$$

$$\varphi_3 = x_3^2(t_f) + x_4^2(t_f) - a_f^2 \tag{4.8}$$

$$\varphi_4 = \text{atan2}\left(x_3(t_f), x_4(t_f)\right) - E_0 - (\tau_f - \tau_0) - \Delta E \tag{4.9}$$

$$\varphi_5 = x_5^2(t_f) + x_6^2(t_f) - A_f^2 \tag{4.10}$$

$$\varphi_6 = \text{atan2}\left(x_5(t_f), x_6(t_f)\right) - \psi_0 - (\tau_f - \tau_0) - \Delta\psi \tag{4.11}$$

where Δx_r, Δy_r, ΔE, and $\Delta\psi$ are desired changes to the unforced ROEs.

Equation (4.6) constrains the final radial component of the instantaneous center to equal its value at the final time under coasting motion plus a desired change. From equation (3.5), x_r remains constant under coasting motion, so its value at the final time is equal to its initial value. Equation (4.7) constrains the final in-track component of the instantaneous center to equal its value at the final time under coasting motion plus a desired change. Equation (4.8) specifies the final in-plane semi-major axis. Equation (4.9) constrains the final in-plane phase angle to equal its value at the final time under coasting motion plus a desired change. Equation (4.10) specifies the final cross-track amplitude. Equation (4.11) constrains the final cross-track phase angle to equal its value at the final time under coasting

motion plus a desired change.

The partial derivatives of $\boldsymbol{\varphi}$ with respect to t and $\boldsymbol{x}$ are

$$\boldsymbol{\varphi}_t = \begin{bmatrix} 0 & \frac{3}{2}\Omega x_1 & 0 & -\Omega & 0 & \Omega \end{bmatrix}^T \tag{4.12}$$

$$\boldsymbol{\varphi}_x = \begin{bmatrix} 1 & 0 & 0 & 0 & 0 & 0 \\ 0 & 1 & 0 & 0 & 0 & 0 \\ 0 & 0 & 2x_3 & \frac{x_4}{x_3^2+x_4^2} & 0 & 0 \\ 0 & 0 & 2x_4 & -\frac{x_3}{x_3^2+x_4^2} & 0 & 0 \\ 0 & 0 & 0 & 0 & 2x_5 & \frac{x_6}{x_5^2+x_6^2} \\ 0 & 0 & 0 & 0 & 2x_6 & -\frac{x_5}{x_5^2+x_6^2} \end{bmatrix} \tag{4.13}$$

Equations (4.12) and (4.13) are used in Section 4.1.2.

Safety Ellipse Egress

For the safety ellipse egress scenarios considered in this work, both the in-plane semi-major axis and cross-track amplitude become zero immediately after the final maneuver. This leads to undefined phase angles, which means that the previous terminal constraint function cannot be applied ($\boldsymbol{\varphi}_x$ in equation (4.13) becomes singular when $a(t_f) = 0$ or $A(t_f) = 0$). A different set of terminal constraints is defined for this particular reconfiguration scenario. Each scalar constraint is written as

$$\varphi_1 = x_1(t_f) - x_{r_0} - \Delta x_r \tag{4.14}$$

$$\varphi_2 = x_2(t_f) + \frac{3}{2}(\tau_f - \tau_0)x_{r_0} - y_{r_0} - \Delta y_r \tag{4.15}$$

$$\varphi_3 = x_3(t_f) \tag{4.16}$$

$$\varphi_4 = x_4(t_f) \tag{4.17}$$

$$\varphi_5 = x_5(t_f) \tag{4.18}$$

$$\varphi_6 = x_6(t_f) \tag{4.19}$$

The constraints on the instantaneous center in equations (4.14) and (4.15) are identical to the constraints in equations (4.6) and (4.7). Equations (4.16) through (4.19) constrain the LROE elements that involve the safety ellipse's dimensions to equal zero at the final time.

The partial derivatives of $\boldsymbol{\varphi}$ with respect to t and $\boldsymbol{x}$ are

$$\boldsymbol{\varphi}_t = \begin{bmatrix} 0 & \frac{3}{2}\Omega x_1 & 0 & 0 & 0 & 0 \end{bmatrix}^T \tag{4.20}$$

$$\boldsymbol{\varphi}_x = \begin{bmatrix} 1 & 0 & 0 & 0 & 0 & 0 \\ 0 & 1 & 0 & 0 & 0 & 0 \\ 0 & 0 & 1 & 0 & 0 & 0 \\ 0 & 0 & 0 & 1 & 0 & 0 \\ 0 & 0 & 0 & 0 & 1 & 0 \\ 0 & 0 & 0 & 0 & 0 & 1 \end{bmatrix} \tag{4.21}$$

Equations (4.20) and (4.21) are used in Section 4.1.2.

Unconstrained Individual Phase Angles

A more relaxed reconfiguration problem is formed when the in-plane and out-of-plane phase angles are free, but the relative phase angle is constrained. This results in five terminal constraints

$$\boldsymbol{\varphi}(t_f, \boldsymbol{x}(t_f)) = \begin{bmatrix} \varphi_1 & \dots & \varphi_5 \end{bmatrix}^T \tag{4.22}$$

These constraints specify a final safety ellipse but not the chaser's specific location along it. Each scalar constraint is written as

$$\varphi_1 = x_1(t_f) - x_{r_0} - \Delta x_r \tag{4.23}$$

$$\varphi_2 = x_2(t_f) + \frac{3}{2}(\tau_f - \tau_0)\, x_{r_0} - y_{r_0} - \Delta y_r \tag{4.24}$$

$$\varphi_3 = x_3^2(t_f) + x_4^2(t_f) - a_f^2 \tag{4.25}$$

$$\varphi_4 = x_5^2(t_f) + x_6^2(t_f) - A_f^2 \tag{4.26}$$

$$\varphi_5 = \text{atan2}(x_3(t_f), x_4(t_f)) - \text{atan2}(x_5(t_f), x_6(t_f)) - \gamma_f \tag{4.27}$$

where γ_f is the final desired relative phase angle. The constraints in equations (4.23) through (4.26) are identical to the constraints in equations (4.6), (4.7), (4.8), and (4.10). Equation (4.27) constrains the difference between the final in-plane and out-of-plane phase angles to equal γ_f.

The partial derivatives of $\boldsymbol{\varphi}$ with respect to t and $\boldsymbol{x}$ are

$$\boldsymbol{\varphi}_t = \begin{bmatrix} 0 & \frac{3}{2}\Omega x_1 & 0 & 0 & 0 \end{bmatrix}^T \tag{4.28}$$

$$\boldsymbol{\varphi}_x = \begin{bmatrix} 1 & 0 & 0 & 0 & 0 \\ 0 & 1 & 0 & 0 & 0 \\ 0 & 0 & 2x_3 & 0 & \frac{x_4}{x_3^2+x_4^2} \\ 0 & 0 & 2x_4 & 0 & -\frac{x_3}{x_3^2+x_4^2} \\ 0 & 0 & 0 & 2x_5 & -\frac{x_6}{x_5^2+x_6^2} \\ 0 & 0 & 0 & 2x_6 & \frac{x_5}{x_5^2+x_6^2} \end{bmatrix} \tag{4.29}$$

Equations (4.28) and (4.29) are used in Section 4.1.2.

4.1.2 Analysis and Necessary Conditions

The Hamiltonian is

$$H = \|\boldsymbol{u}\| + \boldsymbol{\lambda}^T(F\boldsymbol{x} + G\boldsymbol{u}) \tag{4.30}$$

where the abnormal multiplier is assumed to equal 1 [53]. On an optimal trajectory, the dynamics of the costate vector are

$$\dot{\boldsymbol{\lambda}} = -F^T\boldsymbol{\lambda} \tag{4.31}$$

The solution to equation (4.31) is

$$\boldsymbol{\lambda}(t) = \Psi(t, t_0)\boldsymbol{\lambda}_0 \tag{4.32}$$

where [54, 55]

$$\Psi(t, t_0) = \Phi^T(t_0, t) \tag{4.33}$$

At the final time, the transversality conditions are

$$\boldsymbol{\lambda}(t_f) = \boldsymbol{\varphi}_x(t_f, \boldsymbol{x}(t_f))\boldsymbol{\nu} \tag{4.34}$$

$$H(t_f) = -\boldsymbol{\nu}^T \boldsymbol{\varphi}_t(t_f, \boldsymbol{x}(t_f)) \tag{4.35}$$

where $\boldsymbol{\nu}$ is a vector of multipliers associated with the final time. Excluding the special reconfiguration case where the individual phase angles are unconstrained, the matrix $\boldsymbol{\varphi}_x(t_f, x(t_f))$ is full rank, therefore a one-to-one mapping exists between $\boldsymbol{\lambda}(t_f)$ and $\boldsymbol{\nu}$, and $\boldsymbol{\nu}$ can be readily computed once $\boldsymbol{\lambda}$ is known. The computation of $\boldsymbol{\nu}$ for unconstrained individual phase angles in addressed in Section 5.2.4. The primer vector for an optimal control problem with linear dynamics [44, 55] is

$$\boldsymbol{p} = -G^T \boldsymbol{\lambda} \tag{4.36}$$

Certain necessary conditions for an optimal impulsive transfer trajectory are expressed in terms of the primer vector, which was first developed by Lawden [56] and formalized by a number of authors including Neustadt [57] and Rishel [58]. These conditions are [55, 59]:

1) The primer vector and its first time derivative must be continuous everywhere.

2) Impulses occur at instants at which $p = 1$.

3) At all times along the trajectory where maneuvers do not occur, $p \leq 1$.

4) At each impulse time the control impulse is applied in the direction of the primer vector.

5) As a consequence of conditions 2 and 3, $\dot{\boldsymbol{p}}^T \boldsymbol{p} = 0$ at all impulses.

For fixed-time problems, primer vector condition 5 applies only to interior impulses (those that do not occur at t_0 or t_f). However, the proposed problem has a free final time. An extremal for this problem must satisfy the terminal constraints, equations (4.31), (4.34),

and (4.35), and the primer vector conditions. If the final time is fixed, equation (4.35) is no longer necessary. It is now shown that fixed-time and free-time extremals are equivalent.

Lemma 1: Any extremal of the fixed-final-time problem is also an extremal of the free-final-time problem.

Let $(\boldsymbol{x}, \boldsymbol{u}, \boldsymbol{\lambda})$ be an extremal with a fixed final time t_f. By direct computation

$$\boldsymbol{\varphi}_x^T(\boldsymbol{x}(t_f))F\boldsymbol{x}(t_f) + \boldsymbol{\varphi}_t(\boldsymbol{x}(t_f)) = \mathbf{0} \tag{4.37}$$

Equation (4.37) holds for each set of terminal constraints assuming that $\boldsymbol{x}(t_f)$ satisfies the terminal constraints. As equations (4.12), (4.13), (4.28), (4.29), (4.20), and (4.21) show, $\boldsymbol{\varphi}_t$ and $\boldsymbol{\varphi}_x$ are not explicit functions of time, so this argument is dropped. Premultiplying by $\boldsymbol{\nu}^T$ results in

$$\boldsymbol{\nu}^T[\boldsymbol{\varphi}_x^T(\boldsymbol{x}(t_f))F\boldsymbol{x}(t_f) + \boldsymbol{\varphi}_t(\boldsymbol{x}(t_f))] = 0 \tag{4.38}$$

or

$$[\boldsymbol{\varphi}_x(\boldsymbol{x}(t_f))\boldsymbol{\nu}]^T F\boldsymbol{x}(t_f) = -\boldsymbol{\nu}^T\boldsymbol{\varphi}_t(\boldsymbol{x}(t_f)) \tag{4.39}$$

Applying the transversality condition in equation (4.34) shows that

$$\boldsymbol{\lambda}^T(t_f)F\boldsymbol{x}(t_f) = -\boldsymbol{\nu}^T\boldsymbol{\varphi}_t(\boldsymbol{x}(t_f)) \tag{4.40}$$

Along any extremal the Hamiltonian is

$$H = \boldsymbol{\lambda}^T F\boldsymbol{x} \tag{4.41}$$

Substituting equation (4.41) into equation (4.40) leads to

$$H(t_f) = \boldsymbol{\nu}^T\boldsymbol{\varphi}_t(\boldsymbol{x}(t_f)) \tag{4.42}$$

which satisfies the free-final-time transversality conditions. □

In Chapters 5 and 6, the proposed maneuver sequences are derived to satisfy the terminal constraints and costate dynamics. Lemma 1 implies that if the maneuver sequence also satisfies the primer vector conditions, an extremal to problem (4.3) is found. Lemma 1 does not imply, however, that for a given reconfiguration scenario, the total Δv is independent of the transfer time. For example, if a safety ellipse reconfiguration solution that satisfies the necessary conditions has a transfer time of 0.01 orbits, Lemma 1 merely indicates that the solution is also a local extremal for the free-time problem–a solution requiring less Δv could certainly be found by extending the transfer time.

4.2 Second-Order Cone Program

This section formulates a general safety ellipse reconfiguration as a parameter optimization problem. The parameter optimization problem is effectively a discretized version of the optimal control problem. It involves minimizing a function of a discretized set of control variables subject to equality constraints that enforce the system's discretized dynamics. For this problem, Δv vectors are equally spaced across a fixed transfer time. The objective function is the total characteristic velocity, which is consistent with the optimal control problem.

The resulting optimization problem has particular types of convex objective and constraint functions that allows it to be converted into a second-order cone program (SOCP). SOCPs are a class of convex programs. Like all convex programs, a solution to an SOCP is guaranteed to be globally optimal [60]. Also, SOCPs can be readily solved using freely available software packages; this work uses CVX to parse the problem and SDPT3 to compute a solution [61, 62]. This makes an SOCP a useful tool to both validate and compare against analytic results.

Converting the optimal control problem in equation (4.3) into a parameter optimization problem requires discretizing the dynamics, specifying a final time, and specifying a final state such that the terminal constraints are satisfied. The final time is set to multiple orbit periods to emulate the free-time problem [63]. The discrete-time version of the cost function

for impulsive maneuvers is

$$J_d = \sum_{k=0}^{n} \|\Delta \boldsymbol{v}_k\| \tag{4.43}$$

where n is the number of discretization steps. The discrete-time dynamics from a time step index t_k to a time step index t_{k+1} are

$$\boldsymbol{x}(t_{k+1}) = \Phi(t_{k+1}, t_k)\boldsymbol{x}(t_k) + \Phi(t_{k+1}, t_k)G\Delta \boldsymbol{v}_k \tag{4.44}$$

At a final time index t_n, the dynamic are written as

$$\boldsymbol{x}(t_n) = \Phi(t_n, t_0)\boldsymbol{x}(t_0) + \sum_{k=0}^{n} \Phi(t_n, t_k)G\Delta \boldsymbol{v}_k \tag{4.45}$$

When the final time and final state are fixed, minimizing J_d subject to affine state dynamics results in a convex optimization problem. This convex program is

$$\begin{aligned} &\text{minimize} && J_d \\ &\text{subject to} && B\boldsymbol{z} = \boldsymbol{c} \end{aligned} \tag{4.46}$$

where

$$\boldsymbol{z} = \begin{bmatrix} \Delta \boldsymbol{v}_0^T & \dots & \Delta \boldsymbol{v}_k^T & \dots & \Delta \boldsymbol{v}_n^T \end{bmatrix}^T \tag{4.47}$$

$$B = \begin{bmatrix} \Phi(t_n, t_0)G & \dots & \Phi(t_k, t_0)G & \dots & G \end{bmatrix} \tag{4.48}$$

$$\boldsymbol{c} = \boldsymbol{x}_n - \Phi(t_n, t_0)\boldsymbol{x}_0 \tag{4.49}$$

The objective function is written in terms of the optimization vector, $\boldsymbol{z}$, as

$$J_d = \sum_{k=0}^{n} \|M_{\Delta \boldsymbol{v}_k}\boldsymbol{z}\| \tag{4.50}$$

where $M_{\Delta \boldsymbol{v}_k}$ selects the kth $\Delta \boldsymbol{v}$ vector from $\boldsymbol{z}$:

$$M_{\Delta \boldsymbol{v}_k} = \begin{bmatrix} 0_{3\times3} & \dots & I_{3\times3} & \dots & 0_{3\times3} \end{bmatrix} \tag{4.51}$$

It is shown in [64] that norm minimization problems, including problems that involve minimizing the sum of norms, can be formed as SOCPs. This results in

$$\begin{aligned} &\text{minimize} && \boldsymbol{f}^T \bar{\boldsymbol{z}} \\ &\text{subject to} && B\bar{\boldsymbol{z}} = \boldsymbol{c} \\ & && \|\bar{M}_{\Delta \boldsymbol{v}_k} \bar{\boldsymbol{z}}\| \leq \boldsymbol{n}_{\Gamma_k}^T \bar{\boldsymbol{z}},\ k = 0, \dots, n \end{aligned} \tag{4.52}$$

where

$$\boldsymbol{f} = \begin{bmatrix} \mathbf{0}_{1\times3(n+1)} & \mathbf{1}_{1\times(n+1)} \end{bmatrix}^T \tag{4.53}$$

$$\bar{\boldsymbol{z}} = \begin{bmatrix} \Delta \boldsymbol{v}_0^T & \dots & \Delta \boldsymbol{v}_k^T & \dots & \Delta \boldsymbol{v}_n^T & \Gamma_0 & \dots & \Gamma_k & \dots & \Gamma_n \end{bmatrix}^T \tag{4.54}$$

$$\bar{M}_{\Delta \boldsymbol{v}_k} = \begin{bmatrix} 0_{3\times3} & \dots & I_{3\times3} & \dots & 0_{3\times3} & 0_{3\times(n+1)} \end{bmatrix} \tag{4.55}$$

$$\boldsymbol{n}_{\Gamma_k} = \begin{bmatrix} \mathbf{0}_{1\times3(n+1)} & 0 & \dots & 1 & \dots & 0 \end{bmatrix}^T \tag{4.56}$$

The optimization problem in equation (4.52) has a linear objective function, affine equality constraints, and second-order-cone inequality constraints.

CHAPTER 5

DERIVATIONS AND ANALYSIS FOR A GENERAL RECONFIGURATION

5.1 Maneuver Sequence

Sections 5.1.1 through 5.1.4 derive expressions for the maneuvers times and Δv vectors for a three-impulse maneuver sequence that performs a general reconfiguration, which encompasses resizing, phasing, and any other changes to the safety ellipse. The derivation assumes that the maneuvers are separated by a half-orbit period. This pattern was observed for solutions to problem (4.46) for transfer times over one orbit period. It has also been identified by previous authors as an optimal maneuver profile for reconfigurations that are strictly in-plane [21, 46, 47].

Section 5.1.2 derives the maneuver times. Due to the dynamics of cross-track motion and separation between each maneuver, the first cross-track maneuver is constrained to occur at a precise location along the initial relative motion trajectory (with the second and third maneuvers following in half-orbit-period increments). In-plane and out-of-plane maneuvers are coupled, which means that the maneuver times are entirely dependent on desired changes to cross-track motion.

Section 5.1.3 shows that for the primer vector to equal unit magnitude and point in the direction of each impulse (primer vector conditions 2 and 4), a solution for the costate exists when the maneuvers are colinear, with the second maneuver pointing opposite the first and third maneuvers. The colinearity property is then applied in Section 5.1.4 to compute the maneuver scale factors, which are directly related to the magnitudes of each Δv vector. The maneuver scale factors are governed by desired changes to the safety ellipse's instantaneous center.

Section 5.1.5 shows the conditions under which a solution for the initial costate no longer exists. Instantaneous center changes that are large relative to the reconfiguration can

result in a maneuver pointing opposite the direction required for an initial costate solution. With an undefined initial costate, the necessary conditions are ultimately violated.

5.1.1 Preliminary Equations

Assuming a half-orbit-period separation between maneuvers, the in-plane semi-major axis, in-plane phase angle, cross-track amplitude, and cross-track phase angle immediately after the third maneuver are written as functions of their respective values immediately before the first maneuver and each Δv component:

$$a_3^+ = \sqrt{\left(a_1^- \cos E_1^- + \frac{4}{\Omega}\left(\Delta v_{y_1} - \Delta v_{y_2} + \Delta v_{y_3}\right)\right)^2 + \left(a_1^- \sin E_1^- + \frac{2}{\Omega}\left(\Delta v_{x_1} - \Delta v_{x_2} + \Delta v_{x_3}\right)\right)^2} \tag{5.1}$$

$$E_3^+ = \text{atan2}\left(a_1^- \sin E_1^- + \frac{2}{\Omega}\left(\Delta v_{x_1} - \Delta v_{x_2} + \Delta v_{x_3}\right), a_1^- \cos E_1^- + \frac{4}{\Omega}\left(\Delta v_{y_1} - \Delta v_{y_2} + \Delta v_{y_3}\right)\right) \tag{5.2}$$

$$A_3^+ = \sqrt{\left(A_1^- \sin \psi_1^-\right)^2 + \left(A_1^- \cos \psi_1^- + \frac{1}{\Omega}\left(\Delta v_{z_1} - \Delta v_{z_2} + \Delta v_{z_3}\right)\right)^2} \tag{5.3}$$

$$\psi_3^+ = \text{atan2}\left(A_1^- \sin \psi_1^-, A_1^- \cos \psi_1^- + \frac{1}{\Omega}\left(\Delta v_{z_1} - \Delta v_{z_2} + \Delta v_{z_3}\right)\right) \tag{5.4}$$

where the '$-$' superscript denotes a value immediately before the impulse and the '$+$' superscript denotes a value immediately after the impulse. The subscript on the ROEs denotes the maneuver number. For each Δv component, the inner subscript denotes the maneuver direction and the outer subscript denotes the maneuver number. Equations (5.1) through (5.4) are derived from successive application of equations (3.13) through (3.16), which describe the effect of a single Δv on the ROEs. For unforced HCW motion, the in-plane semi-major axis and cross-track amplitude remain constant for coasting motion, therefore

$$a_1^- = a_0 \tag{5.5}$$

$$A_1^- = A_0 \tag{5.6}$$

To satisfy the terminal constraints in equations (4.8) through (4.11), the in-plane semi-major

axis, in-plane phase angle, cross-track amplitude, and cross-track phase angle immediately after the third maneuver are

$$a_3^+ = a_f \tag{5.7}$$

$$E_3^+ = E_1^- + 2\pi + \Delta E \tag{5.8}$$

$$A_3^+ = A_f \tag{5.9}$$

$$\psi_3^+ = \psi_1^- + 2\pi + \Delta\psi \tag{5.10}$$

The following auxiliary variables are defined for each Δv component:

$$\Delta\tilde{v}_x := \Delta v_{x_1} - \Delta v_{x_2} + \Delta v_{x_3} \tag{5.11}$$

$$\Delta\tilde{v}_y := \Delta v_{y_1} - \Delta v_{y_2} + \Delta v_{y_3} \tag{5.12}$$

$$\Delta\tilde{v}_z := \Delta v_{z_1} - \Delta v_{z_2} + \Delta v_{z_3} \tag{5.13}$$

A vector form of equations (5.11) through (5.13) is also defined:

$$\Delta\tilde{\boldsymbol{v}} := \begin{bmatrix} \Delta\tilde{v}_x & \Delta\tilde{v}_y & \Delta\tilde{v}_z \end{bmatrix}^T \tag{5.14}$$

Equation (5.14) can also be expressed as

$$\Delta\tilde{\boldsymbol{v}} = \Delta\boldsymbol{v}_1 - \Delta\boldsymbol{v}_2 + \Delta\boldsymbol{v}_3 \tag{5.15}$$

Substituting equations (5.7) through (5.13) into equations (5.1) through (5.4) results in

$$a_f = \sqrt{\left(a_0 \cos E_1^- + \frac{4}{\Omega}\Delta\tilde{v}_y\right)^2 + \left(a_0 \sin E_1^- + \frac{2}{\Omega}\Delta\tilde{v}_x\right)^2} \tag{5.16}$$

$$E_1^- + 2\pi + \Delta E = \operatorname{atan2}\left(a_0 \sin E_1^- + \frac{2}{\Omega}\Delta\tilde{v}_x, a_0 \cos E_1^- + \frac{4}{\Omega}\Delta\tilde{v}_y\right) \tag{5.17}$$

$$A_f = \sqrt{\left(A_0 \sin\psi_1^-\right)^2 + \left(A_0 \cos\psi_1^- + \frac{1}{\Omega}\Delta\tilde{v}_z\right)^2} \tag{5.18}$$

$$\psi_1^- + 2\pi + \Delta\psi = \operatorname{atan2}\left(A_0 \sin\psi_1^-, A_0 \cos\psi_1^- + \frac{1}{\Omega}\Delta\tilde{v}_z\right) \tag{5.19}$$

5.1.2 Maneuver Times

Equations (5.18) and (5.19) have two unknowns, ψ_1^- and $\Delta\tilde{v}_z$. Solving for ψ_1^- determines the cross-track phase angle immediately before the first maneuver. The cross-track phase angle directly relates to normalized time for coasting HCW motion via equation (3.10). Therefore, the time of the first maneuver can be computed by determining ψ_1^-. Since the spacing of the second and third maneuvers is fixed, all maneuver times can be computed by solving for ψ_1^-.

The derivation of maneuver times begins with determining ψ_1^- through equations (5.18) and (5.19). Equation (5.19) is rewritten as

$$A_0 \sin\psi_1^- = \tan\left(\psi_1^- + \Delta\psi\right)\left(A_0\cos\psi_1^- + \frac{1}{\Omega}\Delta\tilde{v}_z\right) \tag{5.20}$$

Substituting equation (5.20) into equation (5.18) results in

$$A_f = \sqrt{\sec^2\left(\psi_1^- + \Delta\psi\right)\left(A_0\cos\psi_1^- + \frac{1}{\Omega}\Delta\tilde{v}_z\right)^2} \tag{5.21}$$

Equation (5.21) is rewritten as

$$A_0\cos\psi_1^- + \frac{1}{\Omega}\Delta\tilde{v}_z = \pm A_f\cos\left(\psi_1^- + \Delta\psi\right) \tag{5.22}$$

Substituting equation (5.22) back into equation (5.20) results in

$$A_0\sin\psi_1^- = \pm A_f\sin\left(\psi_1^- + \Delta\psi\right) \tag{5.23}$$

To resolve the sign ambiguity in equations (5.22) and (5.23), they are substituted into equation (5.19), which leads to

$$\psi_1^- + \Delta\psi = \text{atan2}\left(\pm\sin\left(\psi_1^- + \Delta\psi\right), \pm\cos\left(\psi_1^- + \Delta\psi\right)\right) \tag{5.24}$$

Equation (5.24) is valid when the signs of the atan2 arguments are positive. Equation (5.23) becomes

$$A_0 \sin \psi_1^- = A_f \sin (\psi_1^- + \Delta\psi) \tag{5.25}$$

Equation (5.25) is rewritten as

$$(A_0 - A_f \cos \Delta\psi) \sin \psi_1^- = A_f \sin \Delta\psi \cos \psi_1^- \tag{5.26}$$

Solving equation (5.26) for ψ_1^-, an expression for the cross-track phase angle immediately before the first maneuver in terms of all known parameters is

$$\psi_1^- = \arctan \left(\frac{A_f \sin \Delta\psi}{A_0 - A_f \cos \Delta\psi} \right) + N\pi,\ N \in \mathbb{Z} \tag{5.27}$$

where $\mathbb{Z}$ is the set of all integers.

From equation (3.10), the normalized time of the first maneuver is

$$\tau_1 = \tau_0 + \psi_1^- - \psi_0 \tag{5.28}$$

Computing the normalized wait time until the first maneuver requires two steps. First, the quantity $\Delta\tau_1$ is computed, which is defined as the difference between τ_1 and τ_0 for ψ_1^- evaluated about $N = 0$:

$$\Delta\tau_1 := \psi_1^-\big|_{N=0} - \psi_0 \tag{5.29}$$

By definition, $\psi_0 \in [-\pi, \pi]$ (ψ is computed using the atan2 function [51]), $\psi_1^-\big|_{N=0} \in [-\frac{\pi}{2}, \frac{\pi}{2}]$, and $\Delta\tau_1 \in [-\frac{3\pi}{2}, \frac{3\pi}{2}]$. Physically, $\Delta\tau_1 < 0$ indicates that the opportunity to maneuver has already occurred, and $\Delta\tau_1 > \pi$ indicates that the opportunity to maneuver is over a half-orbit period away. To account for these instances, ψ_1^- is then incremented or decremented by an integer multiple of π by setting $N \neq 0$. The normalized wait time until the first

maneuver is defined as

$$\tau_{\text{wait}} := \begin{cases} \Delta\tau_1 + 2\pi & \Delta\tau_1 < -\pi \\ \Delta\tau_1 + \pi & -\pi \leq \Delta\tau_1 < 0 \\ \Delta\tau_1 & 0 \leq \Delta\tau_1 < \pi \\ \Delta\tau_1 - \pi & \pi \leq \Delta\tau_1 \end{cases} \tag{5.30}$$

Equation (5.30) ensures $\tau_{\text{wait}} \in [0, \pi)$, which says that, without violating equation (5.27), an opportunity to initiate the maneuver sequence occurs every half-orbit period. The normalized time of the kth maneuver is

$$\tau_k = \tau_{\text{wait}} + \tau_0 + (k-1)\pi \tag{5.31}$$

Equation (5.31) says that the longest possible duration between the initial time and the third maneuver is 1.5 orbits. The final time is

$$\tau_f = \tau_3 + \Delta\tau_f \tag{5.32}$$

Equation (5.32) says that if $\Delta\tau_f > 0$, the chaser coasts to its desired final state.

5.1.3 Maneuver Direction

Existence of a Costate Solution

For the primer vector to equal unit magnitude and point in the direction of the kth impulse, the following equation must hold:

$$\boldsymbol{p}_k = \Delta\hat{\boldsymbol{v}}_k \tag{5.33}$$

where $\Delta\hat{\boldsymbol{v}}_k$ denotes a unit vector pointing in the direction of the kth impulse. Using equations (4.32) and (4.36), equation (5.33) can be rewritten in terms of the costate at the initial

time:

$$G^T \Psi(\tau_k, \tau_0) \boldsymbol{\lambda}_0 = -\Delta \hat{\boldsymbol{v}}_k \tag{5.34}$$

Applying equation (5.34) to each maneuver results in the linear system

$$\Lambda \boldsymbol{\lambda}_0 = \boldsymbol{g} \tag{5.35}$$

where

$$\Lambda = \begin{bmatrix} G^T \Psi(\tau_1, \tau_0) \\ G^T \Psi(\tau_2, \tau_0) \\ G^T \Psi(\tau_3, \tau_0) \end{bmatrix}, \quad \boldsymbol{g} = \begin{bmatrix} -\Delta \hat{\boldsymbol{v}}_1 \\ -\Delta \hat{\boldsymbol{v}}_2 \\ -\Delta \hat{\boldsymbol{v}}_3 \end{bmatrix} \tag{5.36}$$

Lemma 2: For maneuvers that are separated by a half-orbit period, a solution for $\boldsymbol{\lambda}_0$ exists when the maneuvers are colinear, with the second maneuver pointing opposite the first and third maneuvers.

Proof: The augmented matrix $[\Lambda \vdots \boldsymbol{g}]$ for the system in equation (5.35) is

$$[\Lambda \vdots \boldsymbol{g}] = \frac{1}{\Omega} \begin{bmatrix} 0 & -2 & 2\mathrm{c}(\tau_{\text{wait}}) & 2\mathrm{s}(\tau_{\text{wait}}) & 0 & 0 & -\Omega\Delta\hat{v}_{x_1} \\ 2 & 3\tau_{\text{wait}} & -4\mathrm{s}(\tau_{\text{wait}}) & 4\mathrm{c}(\tau_{\text{wait}}) & 0 & 0 & -\Omega\Delta\hat{v}_{y_1} \\ 0 & 0 & 0 & 0 & -\mathrm{s}(\tau_{\text{wait}}) & \mathrm{c}(\tau_{\text{wait}}) & -\Omega\Delta\hat{v}_{z_1} \\ 0 & -2 & -2\mathrm{c}(\tau_{\text{wait}}) & -2\mathrm{s}(\tau_{\text{wait}}) & 0 & 0 & -\Omega\Delta\hat{v}_{x_2} \\ 2 & 3\tau_{\text{wait}} + 3\pi & 4\mathrm{s}(\tau_{\text{wait}}) & -4\mathrm{c}(\tau_{\text{wait}}) & 0 & 0 & -\Omega\Delta\hat{v}_{y_2} \\ 0 & 0 & 0 & 0 & \mathrm{s}(\tau_{\text{wait}}) & -\mathrm{c}(\tau_{\text{wait}}) & -\Omega\Delta\hat{v}_{z_2} \\ 0 & -2 & 2\mathrm{c}(\tau_{\text{wait}}) & 2\mathrm{s}(\tau_{\text{wait}}) & 0 & 0 & -\Omega\Delta\hat{v}_{x_3} \\ 2 & 3\tau_{\text{wait}} + 6\pi & -4\mathrm{s}(\tau_{\text{wait}}) & 4\mathrm{c}(\tau_{\text{wait}}) & 0 & 0 & -\Omega\Delta\hat{v}_{y_3} \\ 0 & 0 & 0 & 0 & -\mathrm{s}(\tau_{\text{wait}}) & \mathrm{c}(\tau_{\text{wait}}) & -\Omega\Delta\hat{v}_{z_3} \end{bmatrix} \tag{5.37}$$

where $\mathrm{c}(\cdot)$ and $\mathrm{s}(\cdot)$ denote $\cos(\cdot)$ and $\sin(\cdot)$. A solution to equation (5.35) for $\boldsymbol{\lambda}_0$ exists only if $\boldsymbol{g}$ lies in the column space of Λ. Equation (5.37) shows that $\boldsymbol{g}$ lies in the column space of

Λ only if

$$\Delta\hat{v}_{x_1} = \Delta\hat{v}_{x_3} \tag{5.38}$$

$$\Delta\hat{v}_{z_1} = \Delta\hat{v}_{z_3} = -\Delta\hat{v}_{z_2} \tag{5.39}$$

For two unit vectors $\hat{\boldsymbol{a}}$ and $\hat{\boldsymbol{b}}$ with $\hat{a}_x = \hat{b}_x$ and $\hat{a}_z = \hat{b}_z$

$$\hat{a}_y^2 = \hat{b}_y^2 \tag{5.40}$$

Equation (5.40) says that $\Delta\hat{v}_{y_1} = \pm\Delta\hat{v}_{y_3}$. If $\Delta\hat{v}_{y_1} = \Delta\hat{v}_{y_3}$, then $\boldsymbol{g}$ is not a linear combination of the second column of Λ and $\Delta\hat{\boldsymbol{v}}_1 = \Delta\hat{\boldsymbol{v}}_3$. If $\boldsymbol{g}$ is also not a linear combination of the first column of Λ, then $\Delta\hat{\boldsymbol{v}}_1 = -\Delta\hat{\boldsymbol{v}}_2$, and a solution for $\boldsymbol{\lambda}_0$ exits. □

Colinear Maneuvers

The kth impulse is written as

$$\Delta\boldsymbol{v}_k = \alpha_k \Delta\hat{\boldsymbol{v}} \tag{5.41}$$

where α_k is the scale factor of the kth maneuver and $\Delta\hat{\boldsymbol{v}}$ is a unit vector pointing along a line common to all three maneuvers. Substituting equation (5.41) into equation (5.15) results in

$$\Delta\tilde{\boldsymbol{v}} = (\alpha_1 - \alpha_2 + \alpha_3)\Delta\hat{\boldsymbol{v}} \tag{5.42}$$

The magnitude of $\Delta\tilde{\boldsymbol{v}}$ is

$$\|\Delta\tilde{\boldsymbol{v}}\| = |\alpha_1 - \alpha_2 + \alpha_3| \tag{5.43}$$

Equations (5.42) and (5.43) show that $\Delta\tilde{\boldsymbol{v}}$ and $\Delta\hat{\boldsymbol{v}}$ point in the same direction:

$$\Delta\hat{\boldsymbol{v}} = \frac{\Delta\tilde{\boldsymbol{v}}}{\|\Delta\tilde{\boldsymbol{v}}\|} \tag{5.44}$$

Therefore the maneuver direction is known once $\Delta\tilde{\boldsymbol{v}}$ is computed.

Computation of $\Delta\tilde{v}$

Computing the elements of $\Delta\tilde{\boldsymbol{v}}$ requires revisiting equations (5.16), (5.17), (5.22), and (5.27). First equations (5.16) and (5.17) are solved for $\Delta\tilde{v}_x$ and $\Delta\tilde{v}_y$. Equation (5.17) is rewritten as

$$a_0 \sin E_1^- + \frac{2}{\Omega}\Delta\tilde{v}_x = \tan(E_1^- + \Delta E)\left(a_0 \cos E_1^- + \frac{4}{\Omega}\Delta\tilde{v}_y\right) \tag{5.45}$$

Substituting equation (5.45) into equation (5.16) results in

$$a_f = \sqrt{\sec^2(E_1^- + \Delta E)\left(a_0 \cos E_1^- + \frac{4}{\Omega}\Delta\tilde{v}_y\right)^2} \tag{5.46}$$

Equation (5.46) is rewritten as

$$a_0 \cos E_1^- + \frac{4}{\Omega}\Delta\tilde{v}_y = \pm a_f \cos\left(E_1^- + \Delta E\right) \tag{5.47}$$

Substituting equation (5.47) into equation (5.45) results in

$$a_0 \sin E_1^- + \frac{2}{\Omega}\Delta\tilde{v}_x = \pm a_f \sin\left(E_1^- + \Delta E\right) \tag{5.48}$$

To resolve the sign ambiguity in equations (5.47) and (5.48), they are substituted into equation (5.17), which leads to

$$E_1^- + \Delta E = \text{atan2}\left(\pm\sin\left(E_1^- + \Delta E\right), \pm\cos\left(E_1^- + \Delta E\right)\right) \tag{5.49}$$

Equation (5.17) is valid when the signs of the atan2 arguments are positive. Equations (5.48) and (5.47) become

$$\Delta\tilde{v}_x = \frac{\Omega}{2}\left(a_f \sin\left(E_1^- + \Delta E\right) - a_0 \sin E_1^-\right) \tag{5.50}$$

$$\Delta\tilde{v}_y = \frac{\Omega}{4}\left(a_f \cos\left(E_1^- + \Delta E\right) - a_0 \cos E_1^-\right) \tag{5.51}$$

where

$$E_1^- = \psi_1^- + \gamma_0 \tag{5.52}$$

Substituting equation (5.52) into equations (5.50) and (5.51), expressions for $\Delta\tilde{v}_x$ and $\Delta\tilde{v}_y$ in terms of all known parameters are

$$\Delta\tilde{v}_x = \frac{\Omega}{2}\Big[\left(a_f\cos\left(\Delta E+\gamma_0\right)-a_0\cos\gamma_0\right)\sin\psi_1^- + \left(a_f\sin\left(\Delta E+\gamma_0\right)-a_0\sin\gamma_0\right)\cos\psi_1^-\Big] \tag{5.53}$$

$$\Delta\tilde{v}_y = \frac{\Omega}{4}\Big[\left(a_f\cos\left(\Delta E+\gamma_0\right)-a_0\cos\gamma_0\right)\cos\psi_1^- - \left(a_f\sin\left(\Delta E+\gamma_0\right)-a_0\sin\gamma_0\right)\sin\psi_1^-\Big] \tag{5.54}$$

Next $\Delta\tilde{v}_z$ is written in terms of all known parameters. Equation (5.22) is rewritten as

$$\Delta\tilde{v}_z = \Omega\left(A_f\cos\left(\psi_1^- + \Delta\psi\right) - A_0\cos\psi_1^-\right) \tag{5.55}$$

where the sign ambiguity is resolved from the conclusion following equation (5.24). Expanding equation (5.55) and rearranging terms results in

$$\Delta\tilde{v}_z = -\Omega\left(\left(A_0 - A_f\cos\Delta\psi\right)\cos\psi_1^- + A_f\sin\Delta\psi\sin\psi_1^-\right) \tag{5.56}$$

Simplifying equation (5.56) relies on the trigonometric identities

$$\cos\psi_1^- = \pm\frac{A_0 - A_f\cos\Delta\psi}{\sqrt{\left(A_0 - A_f\cos\Delta\psi\right)^2 + A_f^2\sin^2\Delta\psi}} \tag{5.57}$$

$$\sin\psi_1^- = \pm\frac{A_f\sin\Delta\psi}{\sqrt{\left(A_0 - A_f\cos\Delta\psi\right)^2 + A_f^2\sin^2\Delta\psi}} \tag{5.58}$$

which follow from equation (5.27).

Simplifying equation (5.56) with the identities in equations (5.57) and (5.58) requires resolving sign ambiguities. To do this, two assumptions are made: 1) the denominators of equations (5.57) and (5.58) are positive, and 2) $\psi_1^- \in [-\pi/2, \pi/2]$ (any modification to

ψ_1^- when computing τ_{wait} is accounted for later). Under these assumptions, the '$\pm$' symbol in equations (5.57) and (5.58) is required to account for the signs of the numerators. For example, $\cos\psi_1^-$ is always positive for $\psi_1^- \in [-\pi/2, \pi/2]$; however, $A_0 - A_f \cos\Delta\psi$ may be negative, requiring a sign change. All possible scenarios are examined for the signs of the numerators of equations (5.57) and (5.58) and their effect on the sign of equation (5.56). Table 5.1 lists the signs of the numerators, range of ψ_1^-, signs of $\cos\psi_1^-$ and $\sin\psi_1^-$, and sign of $\Delta\tilde{v}_z$

Table 5.1: Signs of the numerators of equations (5.57) and (5.58), range of ψ_1^-, signs of $\cos\psi_1^-$ and $\sin\psi_1^-$, and the resulting sign of $\Delta\tilde{v}_z$.

$\text{sgn}(A_0 - A_f\cos\Delta\psi)$	$\text{sgn}(\sin\Delta\psi)$	$\mathcal{R}(\psi_1^-)$	$\text{sgn}(\cos\psi_1^-)$	$\text{sgn}(\sin\psi_1^-)$	$\text{sgn}(\Delta\tilde{v}_z)$
1	1	$(0, \pi/2)$	1	1	-1
1	-1	$(-\pi/2, 0)$	1	-1	-1
-1	-1	$(0, \pi/2)$	1	1	1
-1	1	$(-\pi/2, 0)$	1	-1	1
0	1	$\pi/2$	0	1	-1
0	-1	$-\pi/2$	0	-1	-1
1	0	0	1	0	-1
-1	0	0	1	0	1

Table 5.1 shows that the sign of $\Delta\tilde{v}_z$ directly relates to the sign of $A_0 - A_f\cos\Delta\psi$. Equation (5.55) becomes

$$\Delta\tilde{v}_z = \eta_1\Omega\sqrt{(A_0 - A_f\cos\Delta\psi)^2 + A_f^2\sin^2\Delta\psi} \tag{5.59}$$

where

$$\eta_1 = \begin{cases} -1 & A_0 - A_f\cos\Delta\psi \geq 0 \\ 1 & A_0 - A_f\cos\Delta\psi < 0 \end{cases} \tag{5.60}$$

From equation (5.30), to account for instances where $\Delta\tau_1$ is either negative or greater

than a half-orbit period, ψ_1^- is either incremented or decremented by an integer multiple of π, which flips the sign of $\Delta\tilde{v}_z$ (see equation (5.56)). Considering these cases, η_2 is introduced, which emulates a sign function based on the value of $\Delta\tau_1$:

$$\eta_2 = \begin{cases} 1 & \Delta\tau_1 < -\pi \\ -1 & -\pi \leq \Delta\tau_1 < 0 \\ 1 & 0 \leq \Delta\tau_1 < \pi \\ -1 & \pi \leq \Delta\tau_1 \end{cases} \tag{5.61}$$

Equation (5.59) is simplified as

$$\Delta\tilde{v}_z = \eta\Omega\sqrt{A_0^2 - 2A_0A_f\cos\Delta\psi + A_f^2} \tag{5.62}$$

where $\eta = \eta_1\eta_2$. Equation (5.62) assumes that the square root returns a positive value, leaving the sign determination to η_1 and η_2.

Applying the trig identities of equations (5.57) and (5.58) to equations (5.53) and (5.54) and using the information from Table 5.1 leads to

$$\Delta\tilde{v}_x = \frac{\Omega^2}{2\Delta\tilde{v}_z}\Big[a_0A_0\sin\gamma_0 - a_fA_0\sin(\Delta E + \gamma_0) + a_0A_f\sin(\Delta\psi - \gamma_0) + a_fA_f\sin\gamma_f\Big] \tag{5.63}$$

$$\Delta\tilde{v}_y = \frac{\Omega^2}{4\Delta\tilde{v}_z}\Big[a_0A_0\cos\gamma_0 - a_fA_0\cos(\Delta E + \gamma_0) - a_0A_f\cos(\Delta\psi - \gamma_0) + a_fA_f\cos\gamma_f\Big] \tag{5.64}$$

where

$$\gamma_f = \gamma_0 + \Delta E - \Delta\psi \tag{5.65}$$

Equations (5.63) and (5.64) are implicit functions of η as they both contain a $\Delta\tilde{v}_z$ term. Equations (5.62) through (5.64) determine the elements of $\Delta\tilde{\boldsymbol{v}}$ and, from equation (5.44), the colinear maneuver direction $\Delta\hat{\boldsymbol{v}}$.

Scaling Property

Equations (5.62) through (5.64) show that the maneuver direction is a function of the independent variables a_0, a_f, A_0, A_f, γ_0, ΔE, and $\Delta\psi$. If the initial and final safety ellipses are scaled by a common factor ρ, the in-plane semi-major axes and cross-track amplitudes can be written as

$$a_0 = \rho a_0', \; a_f = \rho a_f', \; A_0 = \rho A_0', \; A_f = \rho A_f' \tag{5.66}$$

Substituting equation (5.66) into equations (5.62) through (5.64), $\Delta\tilde{\boldsymbol{v}}$ becomes

$$\Delta\tilde{\boldsymbol{v}} = \rho\Delta\tilde{\boldsymbol{v}}' \tag{5.67}$$

Equation (5.67) says that for a particular γ_0, ΔE, and $\Delta\psi$, equally scaling the dimensions of the initial and final safety ellipses has no effect on the maneuver direction.

5.1.4 Maneuver Scale Factors

Section 5.1.3 showed that each Δv vector can be expressed as a scale factor multiplied by a colinear direction, and this direction can be computed from all known parameters. Therefore, the maneuver sequence is completely solved once the scale factors in equation (5.41) are known. The absolute value of α_k is equivalent to the magnitude of $\Delta\boldsymbol{v}_k$

From the LROE state dynamics in equation (3.21), achieving a desired final state with three impulses can be written as

$$\boldsymbol{x}^{\text{des}}(t_f) = \Phi(t_f, t_0)\boldsymbol{x}(t_0) + \sum_{k=1}^{3} \Phi(t_f, t_k) G \Delta\boldsymbol{v}_k \tag{5.68}$$

The terminal constraints in Section 4.1.1 are linear in the elements that describe the safety ellipse's instantaneous center. Isolating these elements from equation (5.68) and rearranging terms, a linear system is formed that relates each impulse to the forced and unforced motion

of the instantaneous center at the final time:

$$\begin{bmatrix} 0 & 2 & 0 & 2 & 0 & 2 \\ -2 & -3(\tau_f - \tau_1) & -2 & -3(\tau_f - \tau_2) & -2 & -3(\tau_f - \tau_3) \end{bmatrix} \begin{bmatrix} \Delta v_{x_1} \\ \Delta v_{y_1} \\ \Delta v_{x_2} \\ \Delta v_{y_2} \\ \Delta v_{x_3} \\ \Delta v_{y_3} \end{bmatrix} = \Omega \begin{bmatrix} \Delta x_r \\ \Delta y_r \end{bmatrix} \tag{5.69}$$

where, from equations (4.6) and (4.7),

$$\Delta x_r = x_r(t_f) - x_{r_0} \tag{5.70}$$

$$\Delta y_r = y_r(t_f) + \frac{3}{2}(\tau_f - \tau_0)\, x_{r_0} - y_{r_0} \tag{5.71}$$

The system in equation (5.69) is rewritten considering equation (5.41) and augmented with equation (5.43) to form

$$P\boldsymbol{\alpha} = \boldsymbol{q} \tag{5.72}$$

where

$$P = \begin{bmatrix} 2\Delta\hat{v}_y & 2\Delta\hat{v}_y & 2\Delta\hat{v}_y \\ -2\Delta\hat{v}_x - 3(\tau_f - \tau_1)\Delta\hat{v}_y & -2\Delta\hat{v}_x - 3(\tau_f - \tau_2)\Delta\hat{v}_y & -2\Delta\hat{v}_x - 3(\tau_f - \tau_3)\Delta\hat{v}_y \\ 1 & -1 & 1 \end{bmatrix} \tag{5.73}$$

$$\boldsymbol{q} = \begin{bmatrix} \Omega\Delta x_r & \Omega\Delta y_r & \|\Delta\tilde{\boldsymbol{v}}\| \end{bmatrix}^T \tag{5.74}$$

$$\boldsymbol{\alpha} = \begin{bmatrix} \alpha_1 & \alpha_2 & \alpha_3 \end{bmatrix}^T \tag{5.75}$$

The first two rows of P and $\boldsymbol{q}$ describe the instantaneous center dynamics in equation (5.69). The third row enforces the magnitude of $\Delta\tilde{\boldsymbol{v}}$ described in equation (5.43). To remove the nonlinearity in equation (5.43), it is assumed that $\operatorname{sgn}(\alpha_1 - \alpha_2 + \alpha_3) = 1$. This assumption

is justified in Chapters 7 through 10.

The scale factors are computed by

$$\boldsymbol{\alpha} = P^{-1}\boldsymbol{q} \tag{5.76}$$

where

$$P^{-1} = \begin{bmatrix} -\dfrac{4\Delta\hat{v}_x + 3\big(2(\tau_f - \tau_3) + \pi\big)\Delta\hat{v}_y}{24\pi\Delta\hat{v}_y^2} & -\dfrac{1}{6\pi\Delta\hat{v}_y} & \dfrac{1}{4} \\ \dfrac{1}{4\Delta\hat{v}_y} & 0 & -\dfrac{1}{2} \\ \dfrac{4\Delta\hat{v}_x + 3\big(2(\tau_f - \tau_2) + \pi\big)\Delta\hat{v}_y}{24\pi\Delta\hat{v}_y^2} & \dfrac{1}{6\pi\Delta\hat{v}_y} & \dfrac{1}{4} \end{bmatrix} \tag{5.77}$$

P becomes singular when $\Delta\hat{v}_y = 0$. Solving equation (5.76), the scale factors are

$$\alpha_1 = \|\Delta\tilde{\boldsymbol{v}}\| \left(-\frac{\Omega}{24\pi\Delta\tilde{v}_y^2} \Big[4\Delta\tilde{v}_x + \big(6(\tau_f - \tau_3) + 3\pi\big)\Delta\tilde{v}_y \Big] \Delta x_r - \frac{\Omega}{6\pi\Delta\tilde{v}_y}\Delta y_r + \frac{1}{4} \right) \tag{5.78}$$

$$\alpha_2 = \|\Delta\tilde{\boldsymbol{v}}\| \left(\frac{\Omega}{4\Delta\tilde{v}_y}\Delta x_r - \frac{1}{2} \right) \tag{5.79}$$

$$\alpha_3 = \|\Delta\tilde{\boldsymbol{v}}\| \left(\frac{\Omega}{24\pi\Delta\tilde{v}_y^2} \Big[4\Delta\tilde{v}_x + \big(6(\tau_f - \tau_3) + 9\pi\big)\Delta\tilde{v}_y \Big] \Delta x_r + \frac{\Omega}{6\pi\Delta\tilde{v}_y}\Delta y_r + \frac{1}{4} \right) \tag{5.80}$$

If the reconfiguration results in a final safety ellipse that is stationary ($x_{r_f} = 0$), equations (5.78) through (5.80) become

$$\alpha_1 = \|\Delta\tilde{\boldsymbol{v}}\| \left(\frac{\Omega}{\Delta\tilde{v}_y} \left[\left(\frac{\Delta\tilde{v}_x}{6\pi\Delta\tilde{v}_y} - \frac{3}{8} \right) x_{r_1}^- - \frac{1}{6\pi}\Delta y_{r_1}^- \right] + \frac{1}{4} \right) \tag{5.81}$$

$$\alpha_2 = \|\Delta\tilde{\boldsymbol{v}}\| \left(-\frac{\Omega}{4\Delta\tilde{v}_y} x_{r_1}^- - \frac{1}{2} \right) \tag{5.82}$$

$$\alpha_3 = \|\Delta\tilde{\boldsymbol{v}}\| \left(-\frac{\Omega}{\Delta\tilde{v}_y} \left[\left(\frac{\Delta\tilde{v}_x}{6\pi\Delta\tilde{v}_y} - \frac{1}{8} \right) x_{r_1}^- - \frac{1}{6\pi}\Delta y_{r_1}^- \right] + \frac{1}{4} \right) \tag{5.83}$$

where

$$x_{r_1}^- = x_{r_0} \tag{5.84}$$

$$\Delta y_{r_1}^- = y_{r_f} - y_{r_1}^- \tag{5.85}$$

$x_{r_1}^-$ and $y_{r_1}^-$ are the components of the instantaneous center immediately before the first maneuver. Using equation (3.6), equation (5.85) can also be written as

$$\Delta y_{r_1}^- = y_{r_f} + \frac{3}{2}\left(\tau_1 - \tau_0\right) x_{r_0} - y_{r_0} \tag{5.86}$$

5.1.5 Violation of Necessary Conditions

Revisiting equation (5.38) and (5.39), a solution for the initial costate exists only if

$$\Delta\hat{v}_{x_1} = \Delta\hat{v}_{x_3} \tag{5.87}$$

$$\Delta\hat{v}_{z_1} = \Delta\hat{v}_{z_3} = -\Delta\hat{v}_{z_2} \tag{5.88}$$

Therefore, a solution for the initial costate does not exist for any of the following conditions:

1) $\text{sgn}(\alpha_1) \neq \text{sgn}(\alpha_3)$

2) $\text{sgn}(\alpha_1) = \text{sgn}(\alpha_3) = \text{sgn}(\alpha_2)$

When $\Delta x_r = \Delta y_r = 0$, the signs of α_1, α_2, and α_3 are

$$\text{sgn}(\alpha_1) = \text{sgn}(\alpha_3) = 1,\ \text{sgn}(\alpha_2) = -1 \tag{5.89}$$

Therefore, from equations (5.81) through (5.83), if $x_{r_f} = 0$, a solution for the initial costate exists when

$$\frac{\Omega}{\Delta\tilde{v}_y}\left[\left(\frac{3}{8} - \frac{\Delta\tilde{v}_x}{6\pi\Delta\tilde{v}_y}\right) x_{r_1}^- + \frac{1}{6\pi}\Delta y_{r_1}^-\right] < \frac{1}{4} \tag{5.90}$$

$$\frac{\Omega}{\Delta\tilde{v}_y} x_{r_1}^- > -2 \tag{5.91}$$

$$\frac{\Omega}{\Delta\tilde{v}_y}\left[\left(\frac{1}{8} - \frac{\Delta\tilde{v}_x}{6\pi\Delta\tilde{v}_y}\right) x_{r_1}^- + \frac{1}{6\pi}\Delta y_{r_1}^-\right] > -\frac{1}{4} \tag{5.92}$$

Equations (5.90) through (5.92) are used in Chapters 7 through 10 to approximate how large an instantaneous center change can be incorporated into a reconfiguration without violating the necessary conditions for optimality.

5.2 Costate and Primer Vector

Sections 5.2.1 through 5.2.4 derive expressions for the costate and primer vector associated with the maneuver sequence. Section 5.2.1 computes a general costate and primer vector using the solution for the initial costate from Section 5.1.3. Due to the separation between each maneuver, there is an ambiguity in the costate elements associated with cross-track motion, and this ambiguity carries over to the primer vector.

Section 5.2.2 shows how the cross-track ambiguity can be resolved by applying primer vector condition 5 (see Section 4.1.2). This approach is valid for typical reconfiguration scenarios with constrained individual phase angles (i.e., specified ΔE and $\Delta\psi$), as well as safety ellipse egress. The resulting primer vector satisfies necessary conditions 1, 2, 4, and 5. It is then shown in Section 5.2.3 that satisfying the remaining primer vector condition depends on the radial and cross-track components of the maneuver direction.

Section 5.2.4 shows that for a reconfiguration scenario where the individual phase angles are unspecified but the relative phase angle is constrained, the cross-track ambiguity can be resolved through a linear system formed using the transversality conditions associated with the final costate. This solution is used to analyze a special case of nominal safety ellipse resizing discussed in Chapter 7.

5.2.1 General Solution

From the solution to equation (5.35) proposed in Lemma 2, the costate at the initial time is

$$\boldsymbol{\lambda}_0 = -\Omega \begin{bmatrix} 0 \\ 0 \\ \frac{1}{2}\Delta\hat{v}_x \cos\left(\tau_{\text{wait}}\right) - \frac{1}{4}\Delta\hat{v}_y \sin\left(\tau_{\text{wait}}\right) \\ \frac{1}{4}\Delta\hat{v}_y \cos\left(\tau_{\text{wait}}\right) + \frac{1}{2}\Delta\hat{v}_x \sin\left(\tau_{\text{wait}}\right) \\ \lambda_{5_0} \\ \Delta\hat{v}_z \sec\left(\tau_{\text{wait}}\right) + \lambda_{5_0} \tan\left(\tau_{\text{wait}}\right) \end{bmatrix} \tag{5.93}$$

Here the maneuver subscript is dropped because the maneuvers are colinear. The subscripts on λ_{5_0} denote the fifth element at the initial time. The costate elements associated with the

instantaneous center are zero. There is an ambiguity in the last two elements of $\boldsymbol{\lambda}_0$ because $\text{rank}(\Lambda) = 5$. From equation (4.32), the costate at an arbitrary time is

$$\boldsymbol{\lambda} = -\Omega \begin{bmatrix} 0 \\ 0 \\ \frac{1}{2}\Delta\hat{v}_x \cos(\tau - \tau_1) + \frac{1}{4}\Delta\hat{v}_y \sin(\tau - \tau_1) \\ \frac{1}{4}\Delta\hat{v}_y \cos(\tau - \tau_1) - \frac{1}{2}\Delta\hat{v}_x \sin(\tau - \tau_1) \\ \lambda_{5_0}\big(\cos(\tau_0 - \tau) - \sin(\tau_0 - \tau)\tan(\tau_{\text{wait}})\big) - \Delta\hat{v}_z \sin(\tau_0 - \tau)\sec(\tau_{\text{wait}}) \\ \lambda_{5_0}\big(\sin(\tau_0 - \tau) + \cos(\tau_0 - \tau)\tan(\tau_{\text{wait}})\big) + \Delta\hat{v}_z \cos(\tau_0 - \tau)\sec(\tau_{\text{wait}}) \end{bmatrix} \tag{5.94}$$

The cross-track elements in equation (5.94) can be reduced further, resulting in

$$\boldsymbol{\lambda} = -\Omega \begin{bmatrix} 0 \\ 0 \\ \frac{1}{2}\Delta\hat{v}_x \cos(\tau - \tau_1) + \frac{1}{4}\Delta\hat{v}_y \sin(\tau - \tau_1) \\ \frac{1}{4}\Delta\hat{v}_y \cos(\tau - \tau_1) - \frac{1}{2}\Delta\hat{v}_x \sin(\tau - \tau_1) \\ \big(\lambda_{5_0} \cos(\tau_1 - \tau) - \Delta\hat{v}_z \sin(\tau_0 - \tau)\big)\sec(\tau_{\text{wait}}) \\ \big(\lambda_{5_0} \sin(\tau_1 - \tau) + \Delta\hat{v}_z \cos(\tau_0 - \tau)\big)\sec(\tau_{\text{wait}}) \end{bmatrix} \tag{5.95}$$

From equation (4.36), the primer vector is

$$\boldsymbol{p} = \begin{bmatrix} \Delta\hat{v}_x \cos(\tau - \tau_1) + \frac{1}{2}\Delta\hat{v}_y \sin(\tau - \tau_1) \\ \Delta\hat{v}_y \cos(\tau - \tau_1) - 2\Delta\hat{v}_x \sin(\tau - \tau_1) \\ \big(\lambda_{5_0} \sin(\tau_1 - \tau) + \Delta\hat{v}_z \cos(\tau_0 - \tau)\big)\sec(\tau_{\text{wait}}) \end{bmatrix} \tag{5.96}$$

It will be shown that the solutions for λ_{5_0} cancel out the the secant function in the third element of $\boldsymbol{p}$. The primer vector at the impulse times $\tau = \tau_k$ has unit magnitude and points in the direction of the maneuvers:

$$\boldsymbol{p}_1 = \boldsymbol{p}_3 = \begin{bmatrix} \Delta\hat{v}_x & \Delta\hat{v}_y & \Delta\hat{v}_z \end{bmatrix}^T \tag{5.97}$$

$$\boldsymbol{p}_2 = -\boldsymbol{p}_1 \tag{5.98}$$

5.2.2 Computation of λ_{5_0}

The time derivative of the primer vector is

$$\dot{\boldsymbol{p}} = \Omega \begin{bmatrix} \frac{1}{2}\Delta\hat{v}_y \cos(\tau - \tau_1) - \Delta\hat{v}_x \sin(\tau - \tau_1) \\ -\Delta\hat{v}_y \sin(\tau - \tau_1) - 2\Delta\hat{v}_x \cos(\tau - \tau_1) \\ \big(\Delta\hat{v}_z \sin(\tau_0 - \tau) - \lambda_{5_0} \cos(\tau_1 - \tau)\big) \sec(\tau_{\text{wait}}) \end{bmatrix} \tag{5.99}$$

The time derivative of the primer vector at each impulse time is

$$\dot{\boldsymbol{p}}_1 = \dot{\boldsymbol{p}}_3 = \Omega \begin{bmatrix} \frac{1}{2}\Delta\hat{v}_y & -2\Delta\hat{v}_x & -\Delta\hat{v}_z \tan(\tau_{\text{wait}}) - \lambda_{5_0} \sec(\tau_{\text{wait}}) \end{bmatrix}^T \tag{5.100}$$

$$\dot{\boldsymbol{p}}_2 = -\dot{\boldsymbol{p}}_1 \tag{5.101}$$

The inner product of $\dot{\boldsymbol{p}}_k$ and $\boldsymbol{p}_k$ is

$$\dot{\boldsymbol{p}}_k^T \boldsymbol{p}_k = -\frac{3}{2}\Omega\Delta\hat{v}_x\Delta\hat{v}_y - \Omega\Delta\hat{v}_z\big(\Delta\hat{v}_z \tan(\tau_{\text{wait}}) + \lambda_{5_0} \sec(\tau_{\text{wait}})\big) \tag{5.102}$$

To satisfy primer vector necessary condition 5 ($\dot{\boldsymbol{p}}_k^T \boldsymbol{p}_k = 0$)

$$\lambda_{5_0} = -\Delta\hat{v}_z \sin(\tau_{\text{wait}}) - \frac{3}{2}\frac{\Delta\hat{v}_x\Delta\hat{v}_y}{\Delta\hat{v}_z} \cos(\tau_{\text{wait}}) \tag{5.103}$$

5.2.3 Violation of Necessary Conditions

The primer vector satisfies necessary conditions 1, 2, 4, and 5. Necessary condition 3, which states that $p \leq 1$ at all times along the trajectory where maneuvers do not occur, is analyzed in the remainder of this section.

Substituting equation (5.103) into equation (5.96), the primer vector becomes

$$\boldsymbol{p} = \begin{bmatrix} \Delta\hat{v}_x \cos(\tau - \tau_1) + \frac{1}{2}\Delta\hat{v}_y \sin(\tau - \tau_1) \\ \Delta\hat{v}_y \cos(\tau - \tau_1) - 2\Delta\hat{v}_x \sin(\tau - \tau_1) \\ \Delta\hat{v}_z \cos(\tau - \tau_1) + \frac{3}{2}\frac{\Delta\hat{v}_x\Delta\hat{v}_y}{\Delta\hat{v}_z} \sin(\tau - \tau_1) \end{bmatrix} \tag{5.104}$$

The square of the magnitude of the primer vector is

$$\|\boldsymbol{p}\|^2 = 1 + \sin^2(\tau - \tau_1)\left(3\Delta\hat{v}_x^2 - \frac{3}{4}\Delta\hat{v}_y^2 - \Delta\hat{v}_z^2 + \frac{9}{4}\frac{\Delta\hat{v}_x^2\Delta\hat{v}_y^2}{\Delta\hat{v}_z^2}\right) \tag{5.105}$$

The condition $p \leq 1$ is satisfied when

$$3\Delta\hat{v}_x^2 - \frac{3}{4}\Delta\hat{v}_y^2 - \Delta\hat{v}_z^2 + \frac{9}{4}\frac{\Delta\hat{v}_x^2\Delta\hat{v}_y^2}{\Delta\hat{v}_z^2} \leq 0 \tag{5.106}$$

Equation (5.106) is rewritten as

$$\Delta\hat{v}_z^4 + \Delta\hat{v}_z^2\left(\frac{3}{4}\Delta\hat{v}_y^2 - 3\Delta\hat{v}_x^2\right) - \frac{9}{4}\Delta\hat{v}_x^2\Delta\hat{v}_y^2 \geq 0 \tag{5.107}$$

which is factored as

$$\underbrace{\left(\Delta\hat{v}_z^2 - 3\Delta\hat{v}_x^2\right)}_{R_1}\underbrace{\left(\Delta\hat{v}_z^2 + \frac{3}{4}\Delta\hat{v}_y^2\right)}_{R_2} \geq 0 \tag{5.108}$$

R_2 is always positive, therefore equation (5.108) holds only when $R_1 \geq 0$, or

$$\Delta\hat{v}_z^2 \geq 3\Delta\hat{v}_x^2 \tag{5.109}$$

When equation (5.109) is true, the primer vector necessary conditions are satisfied.

5.2.4 Computation of λ_{5_0} for Unconstrained Individual Phase Angles

Revisiting equation (4.34), one transversality condition is

$$\boldsymbol{\lambda}(t_f) = \boldsymbol{\varphi}_x(t_f, \boldsymbol{x}(t_f))\boldsymbol{\nu} \tag{5.110}$$

For reconfiguration scenarios where the in-plane and out-of-plane phase angles are either specified or undefined at the final time, a one-to-one mapping exists between $\boldsymbol{\lambda}(t_f)$ and $\boldsymbol{\nu}$. For reconfiguration scenarios where only the relative phase angle is specified, equation (5.110) becomes overdetermined ($\boldsymbol{\varphi}_x$ is shown in equation (4.29)). However, this linear

system can be used to solve for λ_{5_0}. From equation (5.95), the costate at the final time is

$$\boldsymbol{\lambda}(t_f) = -\Omega \begin{bmatrix} 0 \\ 0 \\ \frac{1}{2}\Delta\hat{v}_x \cos(\tau_f - \tau_1) + \frac{1}{4}\Delta\hat{v}_y \sin(\tau_f - \tau_1) \\ \frac{1}{4}\Delta\hat{v}_y \cos(\tau_f - \tau_1) - \frac{1}{2}\Delta\hat{v}_x \sin(\tau_f - \tau_1) \\ \big(\lambda_{5_0} \cos(\tau_1 - \tau_f) - \Delta\hat{v}_z \sin(\tau_0 - \tau_f)\big) \sec(\tau_{\text{wait}}) \\ \big(\lambda_{5_0} \sin(\tau_1 - \tau_f) + \Delta\hat{v}_z \cos(\tau_0 - \tau_f)\big) \sec(\tau_{\text{wait}}) \end{bmatrix} \tag{5.111}$$

Evaluating equation (5.110), the resulting scalar equations are

$$\lambda_{1_f} = \nu_1 \tag{5.112}$$

$$\lambda_{2_f} = \nu_2 \tag{5.113}$$

$$\lambda_{3_f} = 2\nu_3 a_f \sin E_f + \frac{\nu_5}{a_f} \cos E_f \tag{5.114}$$

$$\lambda_{4_f} = 2\nu_3 a_f \cos E_f - \frac{\nu_5}{a_f} \sin E_f \tag{5.115}$$

$$\lambda_{5_f} = 2\nu_4 A_f \sin\psi_f - \frac{\nu_5}{A_f} \sin\psi_f \tag{5.116}$$

$$\lambda_{6_f} = 2\nu_4 A_f \cos\psi_f + \frac{\nu_5}{A_f} \cos\psi_f \tag{5.117}$$

Equations (5.114) through (5.117) describe an overdetermined system for elements ν_3, ν_4, and ν_5. Substituting λ_{5_f} and λ_{6_f} from equation (5.111) into equations (5.116) and (5.117) results in

$$-\Omega\big(\lambda_{5_0} \cos(\tau_1 - \tau_f) - \Delta\hat{v}_z \sin(\tau_0 - \tau_f)\big) \sec(\tau_{\text{wait}}) = 2\nu_4 A_f \sin\psi_f - \frac{\nu_5}{A_f} \sin\psi_f \tag{5.118}$$

$$-\Omega\big(\lambda_{5_0} \sin(\tau_1 - \tau_f) + \Delta\hat{v}_z \cos(\tau_0 - \tau_f)\big) \sec(\tau_{\text{wait}}) = 2\nu_4 A_f \cos\psi_f + \frac{\nu_5}{A_f} \cos\psi_f \tag{5.119}$$

Equations (5.118) and (5.119) introduce an additional unknown variable, λ_{5_0}. A linear system is formed using equations (5.114), (5.115), (5.118), and (5.119):

$$R\bar{\boldsymbol{\nu}} = \bar{\boldsymbol{\lambda}} \tag{5.120}$$

where

$$R = \begin{bmatrix} 2a_f \sin E_f & 0 & \frac{1}{a_f}\cos E_f & 0 \\ 2a_f \cos E_f & 0 & -\frac{1}{a_f}\sin E_f & 0 \\ 0 & 2A_f \sin\psi_f & -\frac{1}{A_f}\cos\psi_f & \Omega\cos(\tau_1-\tau_f)\sec(\tau_{\text{wait}}) \\ 0 & 2A_f\cos\psi_f & \frac{1}{A_f}\sin\psi_f & \Omega\sin(\tau_1-\tau_f)\sec(\tau_{\text{wait}}) \end{bmatrix} \tag{5.121}$$

$$\bar{\boldsymbol{\nu}} = \begin{bmatrix} \nu_3 & \nu_4 & \nu_5 & \lambda_{5_0} \end{bmatrix}^T \tag{5.122}$$

$$\bar{\boldsymbol{\lambda}} = \begin{bmatrix} \lambda_{3_f} & \lambda_{4_f} & \Omega\Delta\hat{v}_z\sin(\tau_0-\tau_f)\sec(\tau_{\text{wait}}) & -\Omega\Delta\hat{v}_z\cos(\tau_0-\tau_f)\sec(\tau_{\text{wait}}) \end{bmatrix}^T \tag{5.123}$$

The solution to equation (5.120) for λ_{5_0} is

$$\lambda_{5_0} = \sec(\psi_f+\tau_1-\tau_f)\Bigg(\Delta\hat{v}_z\sin(\psi_f+\tau_0-\tau_f) + \frac{1}{\Omega}\frac{a_f}{A_f}\left(\lambda_{3_f}\cos E_f - \lambda_{4_f}\sin E_f\right)\cos(\tau_{\text{wait}})\Bigg) \tag{5.124}$$

Substituting λ_{3_f} and λ_{4_f} from equation (5.111) into equation (5.124), λ_{5_0} becomes

$$\lambda_{5_0} = \sec(\psi_f+\tau_1-\tau_f)\Bigg(\Delta\hat{v}_z\sin(\psi_f+\tau_0-\tau_f) + \frac{1}{2}\frac{a_f}{A_f}\left[\frac{1}{2}\Delta\hat{v}_y\sin(E_f+\tau_1-\tau_f) - \Delta\hat{v}_x\cos(E_f+\tau_1-\tau_f)\right]\cos(\tau_{\text{wait}})\Bigg) \tag{5.125}$$

Using equations (4.9) and (4.11), equation (5.125) can also be written as

$$\lambda_{5_0} = \sec(\psi_1^- + \Delta\psi)\Bigg(\Delta\hat{v}_z\sin(\psi_0+\Delta\psi) + \frac{1}{2}\frac{a_f}{A_f}\left[\frac{1}{2}\Delta\hat{v}_y\sin(E_1^- + \Delta E) - \Delta\hat{v}_x\cos(E_1^- + \Delta E)\right]\cos(\tau_{\text{wait}})\Bigg) \tag{5.126}$$

Equation (5.126) is used in Chapter 7 to show when the nominal resizing maneuver sequence, which specifies an in-plane phase angle change equal to zero, is also the optimal solution to the problem where the in-plane phase angle is unconstrained.

CHAPTER 6

DERIVATIONS AND ANALYSIS FOR DECOUPLED RECONFIGURATIONS

6.1 Overview

This chapter applies principles of the general safety ellipse maneuver sequence to problems where the desired changes are either strictly in-plane or strictly out-of-plane. Like the underlying HCW dynamics, the maneuver sequences are decoupled, and they are analyzed separately in Sections 6.2 and 6.3. Although these maneuver sequences are not explicitly used in Chapters 7 through 10, the results in this chapter are useful for understanding the relationship between the primer vector necessary conditions and properties of the initial and final safety ellipses for the general maneuver sequence, which is discussed at length in Section 7.2.2.

6.2 In-Plane

This section derives and analyzes a maneuver sequence that performs a reconfiguration that is strictly in-plane. The maneuver sequence maintains the same structure as the general (coupled) reconfiguration with three colinear impulses separated by a half orbit period. Section 6.2.1 shows that satisfying the primer vector conditions requires the maneuver direction to be either purely radial or in-track. It is then shown that in-track maneuvers require less Δv to achieve a desired reconfiguration. Section 6.2.2 derives the maneuver sequence and shows that the primer vector necessary conditions are always satisfied (assuming a solution for the costate exists). The resulting maneuver sequence matches the optimal in-plane reconfigurations proposed in [21, 46, 47]. Section 6.2.3 uses Monte Carlo methods to validate optimality. Section 6.2.4 derives bounds on the allowable changes to the instantaneous center that do not affect optimality.

6.2.1 Preliminary Analysis

This preliminary analysis assumes that the in-plane phase angle is constrained (i.e., ΔE is specified). Substituting $\Delta\hat{v}_z = 0$ into equation (5.102), the inner product of $\dot{\boldsymbol{p}}_k$ and $\boldsymbol{p}_k$ for planar maneuvers is

$$\dot{\boldsymbol{p}}_k^T \boldsymbol{p}_k = \frac{3}{2}\Omega\Delta\hat{v}_x\Delta\hat{v}_y \tag{6.1}$$

Equation (6.1) says that to satisfy the primer vector conditions, either $\Delta\hat{v}_x = 0$ or $\Delta\hat{v}_y = 0$.

From equations (5.50) and (5.51), the in-plane phase angle immediately before the first maneuver is a function of $\Delta\tilde{v}_x$ and $\Delta\tilde{v}_y$. Substituting $\Delta\tilde{v}_x = 0$ into equation (5.50) and solving for E_1^- results in

$$E_1^- = \arctan\left(\frac{a_f \sin\Delta E}{a_0 - a_f\cos\Delta E}\right) + N\pi,\ N \in \mathbb{Z} \tag{6.2}$$

Substituting equation (6.2) into equation (5.51) leads to

$$\Delta\tilde{v}_y = \pm\frac{\Omega}{4}\left(a_0^2 - 2a_0a_f\cos\Delta E + a_f^2\right) \tag{6.3}$$

Taking the absolute value of equation (6.3), the total Δv using only in-track maneuvers is

$$\|\Delta\tilde{\boldsymbol{v}}\| = \frac{\Omega}{4}\sqrt{a_0^2 - 2a_0a_f\cos\Delta E + a_f^2} \tag{6.4}$$

Substituting $\Delta\tilde{v}_y = 0$ into equation (5.51) and solving for E_1^- results in

$$E_1^- = \arctan\left(\frac{a_f\cos\Delta E - a_0}{a_f\sin\Delta E}\right) + N\pi,\ N \in \mathbb{Z} \tag{6.5}$$

Substituting equation (6.5) into equation (5.50) leads to

$$\Delta\tilde{v}_x = \pm\frac{\Omega}{2}\left(a_0^2 - 2a_0a_f\cos\Delta E + a_f^2\right) \tag{6.6}$$

Taking the absolute value of equation (6.6), the total Δv using radial maneuvers is

$$\|\Delta\tilde{\boldsymbol{v}}\| = \frac{\Omega}{2}\sqrt{a_0^2 - 2a_0a_f\cos\Delta E + a_f^2} \tag{6.7}$$

Comparing equations (6.4) and (6.7), the total Δv when $\Delta\hat{v}_x = 0$ is exactly one-half the total Δv when $\Delta\hat{v}_y = 0$. Therefore, the maneuver sequence must consist of only in-track maneuvers.

6.2.2 Maneuver Sequence and Primer Vector

The in-plane phase angle immediately before the first maneuver is given in equation (6.2). The quantity $\Delta\tau_1$ for a planar reconfiguration is defined as

$$\Delta\tau_1 := E_1^- - E_0 \tag{6.8}$$

τ_{wait} and τ_1 through τ_f all follow from equations (5.30) through (5.32). Determining the sign of equation (6.3) follows the same process outlined in Table 5.1. Equation (6.4) becomes

$$\Delta\tilde{v}_y = \eta\frac{\Omega}{4}\sqrt{a_0^2 - 2a_0a_f\cos\Delta E + a_f^2} \tag{6.9}$$

where $\eta = \eta_1\eta_2$. The equation for η_1 is the in-plane analog to equation (5.60):

$$\eta_1 = \begin{cases} -1 & a_0 - a_f\cos\Delta E \geq 0 \\ 1 & a_0 - a_f\cos\Delta E < 0 \end{cases} \tag{6.10}$$

η_2 is given in equation (5.61) (using $\Delta\tau_1$ from equation (6.8)). Equation (6.9) assumes that the square root returns a positive value, leaving the sign determination to η_1 and η_2.

The maneuver direction is

$$\Delta\hat{v}_y = \eta\begin{bmatrix}0 & 1 & 0\end{bmatrix}^T \tag{6.11}$$

The maneuver magnitudes are computed using equations (5.72) through (5.76), where P is simplified to

$$P = \begin{bmatrix} 2\eta & 2\eta & 2\eta \\ -3\eta(\tau_f - \tau_1) & -3\eta(\tau_f - \tau_2) & -3\eta(\tau_f - \tau_3) \\ 1 & -1 & 1 \end{bmatrix} \tag{6.12}$$

Substituting equation (6.11) into equation (5.96) and setting $\lambda_{5_0} = 0$, the primer vector is

$$\boldsymbol{p} = \eta \begin{bmatrix} \frac{1}{2}\sin(\tau - \tau_1) \\ \cos(\tau - \tau_1) \\ 0 \end{bmatrix} \tag{6.13}$$

The square of the magnitude of the primer vector is

$$\|\boldsymbol{p}\|^2 = \frac{1}{4}\big(1 + 3\cos^2(\tau - \tau_1)\big) \tag{6.14}$$

Equation (6.14) says that $\max(p) = 1$, which occurs at the times of the maneuvers. Therefore, all of the primer vector necessary conditions are satisfied.

6.2.3 Numerical Validation

The primer vector analysis is validated numerically using Monte Carlo methods. Each individual Monte Carlo sample is a particular in-plane reconfiguration, and the transfer trajectory is solved both numerically and analytically. The problem is solved numerically using the SOCP in equation (4.52) with a fixed final time of multiple orbit periods to emulate the free-time problem.

For this analysis, $\Delta x_r = \Delta y_r = 0$. From equation (6.9), the parameters of interest are a_0, a_f, and ΔE. Their values are drawn from uniform distributions:

$$a_0 = \mathcal{U}(0, a_0^n) \tag{6.15}$$

$$a_f = \mathcal{U}(0, a_f^n) \tag{6.16}$$

$$\Delta E = \mathcal{U}(-180^\circ, 180^\circ) \tag{6.17}$$

where $a_0^n = a_f^n = 10\,\text{km}$. The initial in-plane phase angle is also drawn from a uniform distribution to randomize the chaser's initial in-plane location along the safety ellipse.

For all Monte Carlo samples, the Δv from the analytic solution matches the Δv from the numerical solution. In fact, across 500 samples,

$$\min(\Delta v_{\text{num}}/\Delta v_{\text{ana}}) = 1.0000001 \tag{6.18}$$

due to discretization errors with the numerical optimization process.

6.2.4 Instantaneous Center Changes and Optimality

Section 5.1.5 derived bounds on the allowable changes to the instantaneous center that do not affect optimality of the general maneuver sequence. This section computes the bounds for an in-plane reconfiguration. This analysis assumes that the transfer trajectory removes the drift rate at the final time ($x_{r_f} = 0$). Substituting $\Delta\tilde{v}_x = 0$ and equation (6.9) into equations (5.90) through (5.92), a costate solution exists when

$$\pm\frac{\eta}{\alpha}\left(6x_{r_1}^- + \frac{8}{3\pi}\Delta y_{r_1}^-\right) \leq 1 \tag{6.19}$$

$$\pm\frac{\eta}{\alpha}2x_{r_1}^- \geq -1 \tag{6.20}$$

$$\pm\frac{\eta}{\alpha}\left(2x_{r_1}^- + \frac{8}{3\pi}\Delta y_{r_1}^-\right) \geq -1 \tag{6.21}$$

where

$$\alpha = \sqrt{a_0^2 - 2a_0a_f\cos\Delta E + a_f^2} \tag{6.22}$$

$x_{r_1}^-$ is the radial component of the instantaneous center immediately before first maneuver. $\Delta y_{r_1}^-$ is the difference between the desired final in-track component of the instantaneous center and its value immediately before the first maneuver.

Equations (6.19) through (6.21) define polyhedrons in $(x_{r_1}^-, \Delta y_{r_1}^-)$ space that are functions of η and α. Figure 6.1 plots these polyhedrons. They represent, for particular values of η, a region of allowable instantaneous center changes immediately before the first maneuver

that do not affect optimality of the maneuver sequence.

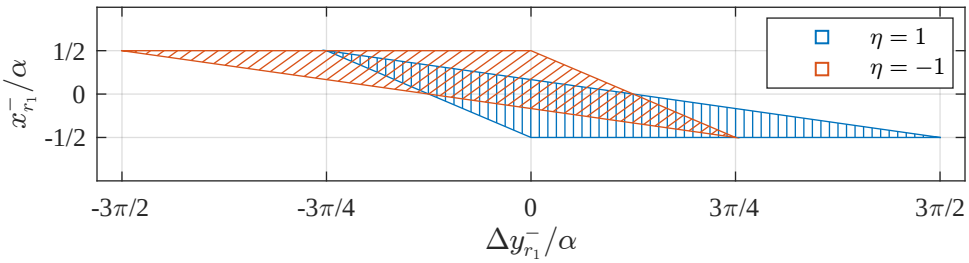

Fig. 6.1: Region representing the allowable $(x_{r_1}^-, \Delta y_{r_1}^-)$ pairs that do not affect optimality for particular values of η.

The intersection of these sets is shown in Figure 6.2. This region is independent of η.

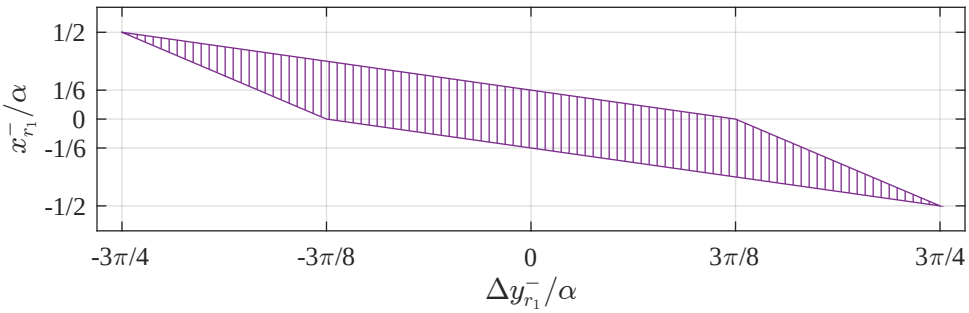

Fig. 6.2: Region representing the allowable $(x_{r_1}^-, \Delta y_{r_1}^-)$ pairs that do not affect optimality.

Figure 6.2 shows that the allowable instantaneous center changes are proportional to α. It also shows that optimality is less sensitive to changes in y_r than x_r.

6.3 Out-of-Plane

This section derives and analyzes a maneuver sequence that performs a reconfiguration that is strictly out-of-plane. Section 6.3.1 shows that arbitrary changes to the cross-track amplitude and phase angle can be made with only one maneuver, as long as the maneuver is performed at a precise location along the trajectory. It also shows that the primer vector necessary conditions remain satisfied when the desired cross-track changes are distributed

over multiple maneuvers separated by a half orbit period. Section 6.3.2 uses Monte Carlo methods to validate optimality.

Unforced out-of-plane HCW motion is described by a harmonic oscillator, so although this maneuver sequence is presented in the context of a safety ellipse reconfiguration, it addresses the general problem of controlling a harmonic oscillator using instantaneous velocity changes.

6.3.1 Maneuver Sequence and Primer Vector

Equation (5.13) can be generalized as

$$\Delta\tilde{v}_z := \sum_{k=1}^{n}(-1)^{k-1}\Delta v_{z_k} \tag{6.23}$$

where n is the number of impulses. Setting $k = 1$, equations (5.18) and (5.19) have two unknowns, Δv_{z_1} and ψ_1^-. Therefore, only one maneuver is needed to change both cross-track parameters if it occurs at ψ_1^-. $\Delta\tilde{v}_z$ expressed in terms of desired changes to the cross-track parameters is given in equation (5.62).

With ψ_1^- computed in equation (5.27), $\Delta\tau_1$ and τ_{wait} follow from equations (5.29) and (5.30). The normalized time of the kth maneuver is given in equation (5.31). The kth maneuver is

$$\Delta\boldsymbol{v}_k = \eta(-1)^{k-1}\begin{bmatrix}0 & 0 & \frac{1}{n}\Delta\tilde{v}_z\end{bmatrix}^T \tag{6.24}$$

where $\eta = \eta_1\eta_2$. η_1 is given in equation (5.60) and η_2 is given in equation (5.61). The kth maneuver direction is

$$\Delta\hat{\boldsymbol{v}}_k = \eta(-1)^{k-1}\begin{bmatrix}0 & 0 & 1\end{bmatrix}^T \tag{6.25}$$

The initial costate is solved using the same approach as equation (5.35). The primer vector is

$$\boldsymbol{p} = \begin{bmatrix}0 & 0 & \left(\lambda_{5_0}\sin(\tau_1-\tau)+\eta\cos(\tau_0-\tau)\right)\sec(\tau_{\text{wait}})\end{bmatrix}^T \tag{6.26}$$

The primer vector at the impulse times $\tau = \tau_k$ has unit magnitude and points in the direction of the maneuvers. The time derivative of the primer vector is

$$\dot{\boldsymbol{p}} = \begin{bmatrix} 0 & 0 & \Omega\big(\eta \sin(\tau_0 - \tau) - \lambda_{5_0} \cos(\tau_1 - \tau)\big) \sec(\tau_{\text{wait}}) \end{bmatrix}^T \tag{6.27}$$

The inner product of $\dot{\boldsymbol{p}}_k$ and $\boldsymbol{p}_k$ is

$$\dot{\boldsymbol{p}}_k^T \boldsymbol{p}_k = -\eta\Omega\big(\eta \tan(\tau_{\text{wait}}) + \lambda_{5_0} \sec(\tau_{\text{wait}})\big) \tag{6.28}$$

To satisfy primer vector condition 5

$$\lambda_{5_0} = -\eta \sin(\tau_{\text{wait}}) \tag{6.29}$$

Substituting equation (6.29) into equation (6.27), the primer vector becomes

$$\boldsymbol{p} = \begin{bmatrix} 0 & 0 & \eta \cos(\tau - \tau_1) \end{bmatrix}^T \tag{6.30}$$

The magnitude of the primer vector is

$$p = |\cos(\tau - \tau_1)| \tag{6.31}$$

Equation (6.31) says that $p = 1$ only where maneuvers occur. Therefore, all of the primer vector conditions are satisfied.

6.3.2 Numerical Validation

The primer vector analysis is validated numerically using Monte Carlo methods. Each individual Monte Carlo sample is a particular cross-track reconfiguration, and the transfer trajectory is solved both numerically and analytically. The problem is solved numerically using the SOCP in equation (4.52) with a fixed final time of multiple orbit periods to emulate the free-time problem.

From equation (5.62), the parameters of interest are A_0, A_f, and $\Delta\psi$. They are all initialized with uniform distributions:

$$A_0 = \mathcal{U}(0, A_0^n) \tag{6.32}$$

$$A_f = \mathcal{U}(0, A_f^n) \tag{6.33}$$

$$\Delta\psi = \mathcal{U}(-180^\circ, 180^\circ) \tag{6.34}$$

where $A_0^n = A_f^n = 10\,\text{km}$. The initial cross-track phase angle is also initialized with a uniform distribution to randomize the chaser's initial cross-track location along the safety ellipse.

For all Monte Carlo samples, the Δv from the analytic solution matches the Δv from the numerical solution. In fact,

$$\min(\Delta v_{\text{num}}/\Delta v_{\text{ana}}) = 1.0000004 \tag{6.35}$$

due to discretization errors with the numerical optimization process.

CHAPTER 7

SAFETY ELLIPSE RESIZING

7.1 Overview

Figure 7.1 shows an example of nominal safety ellipse resizing. The maneuver sequence is indicated by the numbers above each maneuver location. Before maneuver 1, the chaser travels clockwise along the initial safety ellipse, making one revolution every orbit period. Maneuver 1 initiates the transfer trajectory. Maneuver 2 alters the transfer trajectory to make it intersect the final safety ellipse at the time of maneuver 3. Maneuver 3 establishes the final safety ellipse. The chaser remains on the final safety ellipse, traveling clockwise, until another maneuver is performed.

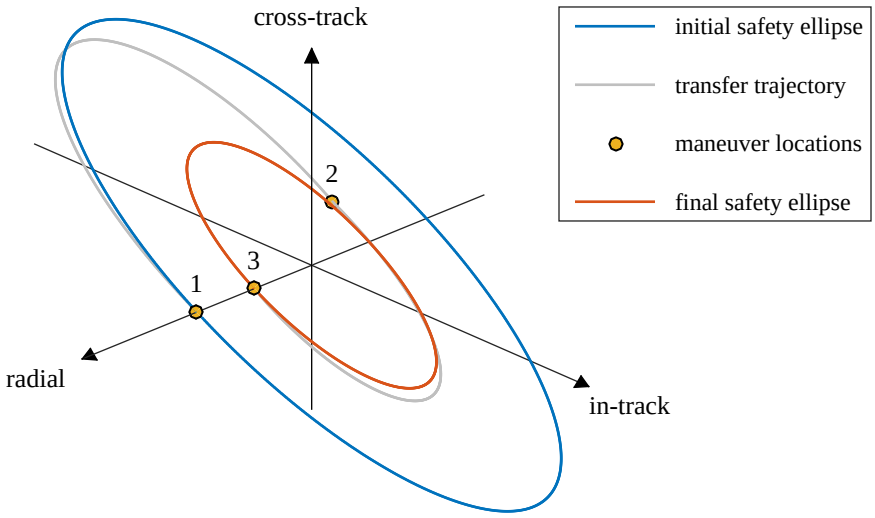

Fig. 7.1: An example of nominal safety ellipse resizing.

The objective of resizing is to make changes to the safety ellipse's dimensions that are large in comparison to changes in the safety ellipse's in-plane phasing, orientation, and

instantaneous center. This chapter analyzes the resizing problem by dividing it into two categories: nominal and off-nominal.

The nominal resizing scenario involves simplifying assumptions that lead to an idealized version of the problem. Although these assumptions remove realism, they also simplify the expressions for the Δv vectors and maneuver times to where analysis of optimality and passive safety can be performed analytically. One key result from this analysis is an equation that relates optimality to the safety ellipse's initial orientation and ratio of the desired change in cross-track amplitude to the desired change in in-plane semi-major axis. This equation is presented in Section 7.2.1 and numerically validated in Section 7.2.2. Section 7.2.3 shows that the nominal transfer trajectories are passively safe. Section 7.2.4 shows that when the initial and final ratios of the cross-track amplitude to in-plane semi-major axis are equal, the nominal maneuver sequence is also the optimal solution to the problem where the in-plane phase angle is unconstrained.

The off-nominal resizing scenario makes no simplifying assumptions. It is a general reconfiguration where the dominant component is a change in the safety ellipse's dimensions. Section 7.3.1 presents equations which approximate the allowable changes to the instantaneous center that do not affect optimality of the analytic solution. Section 7.3.2 analyzes the optimality and passive safety of off-nominal resizing scenarios using Monte Carlo methods.

7.2 Nominal

Nominal resizing is a simplified case of a general reconfiguration. It has the following characteristics:

1) The instantaneous center after the transfer trajectory is equal to the instantaneous center if no maneuvers had occurred ($\Delta x_r = 0$ and $\Delta y_r = 0$).

2) The in-plane phase angle after the transfer is equal to the in-plane phase angle if no maneuvers had occurred ($\Delta E = 0$).

3) The orientation after the transfer is equal to the orientation before the transfer ($\Delta\gamma = 0$).

7.2.1 Maneuver Sequence and Primer Vector Analysis

Substituting $\Delta x_r = \Delta y_r = \Delta E = \Delta\psi = 0$ into equations (5.60), (5.62) through (5.64), and (5.74) and (5.76), the Δv vectors are

$$\Delta\boldsymbol{v}_1 = \eta_2 \frac{\Omega}{16} \begin{bmatrix} 2\Delta a \sin\gamma_0 & \Delta a \cos\gamma_0 & 4\Delta A \end{bmatrix}^T, \; \Delta\boldsymbol{v}_2 = -2\Delta\boldsymbol{v}_1, \; \Delta\boldsymbol{v}_3 = \Delta\boldsymbol{v}_1 \tag{7.1}$$

where

$$\Delta a = a_f - a_0 \tag{7.2}$$

$$\Delta A = A_f - A_0 \tag{7.3}$$

Substituting $\Delta\psi = 0$ into equation (5.27), the cross-track phase angle immediately before the first maneuver is

$$\psi_1^- = N\pi, \; N \in \mathbb{Z} \tag{7.4}$$

Equation (7.4) says that the first maneuver occurs when the chaser crosses the target's orbital plane.

Substituting equation (7.1) into equation (5.109), the primer vector conditions are satisfied when

$$\cos^2\gamma_0 \geq 1 - \frac{4}{3}\frac{\Delta A^2}{\Delta a^2} \tag{7.5}$$

Equation (7.5) says that optimality depends on the safety ellipse's initial orientation and ratio of the desired change in cross-track amplitude to the desired change in in-plane semi-major axis. The primer vector conditions are satisfied for all orientations when

$$\frac{\Delta A}{\Delta a} \geq \frac{\sqrt{3}}{2} \tag{7.6}$$

7.2.2 Numerical Validation

The primer vector analysis is validated numerically. A family of nominal resizing cases, distinguished by different values of γ_0 and $\Delta A/\Delta a$, are solved both numerically and analytically (as equation (7.5) shows, optimality is independent of a_0 and A_0). The problem is solved numerically using the SOCP in equation (4.52) with a fixed final time of multiple orbit periods to emulate the free-time problem. Figure 7.2 shows a contour plot with level sets that represent the ratio of the Δv from the SOCP solution to the Δv from the analytic solution as a function of γ_0 and $\Delta A/\Delta a$. This plot is identical when γ_0 is shifted by $\pm 180°$.

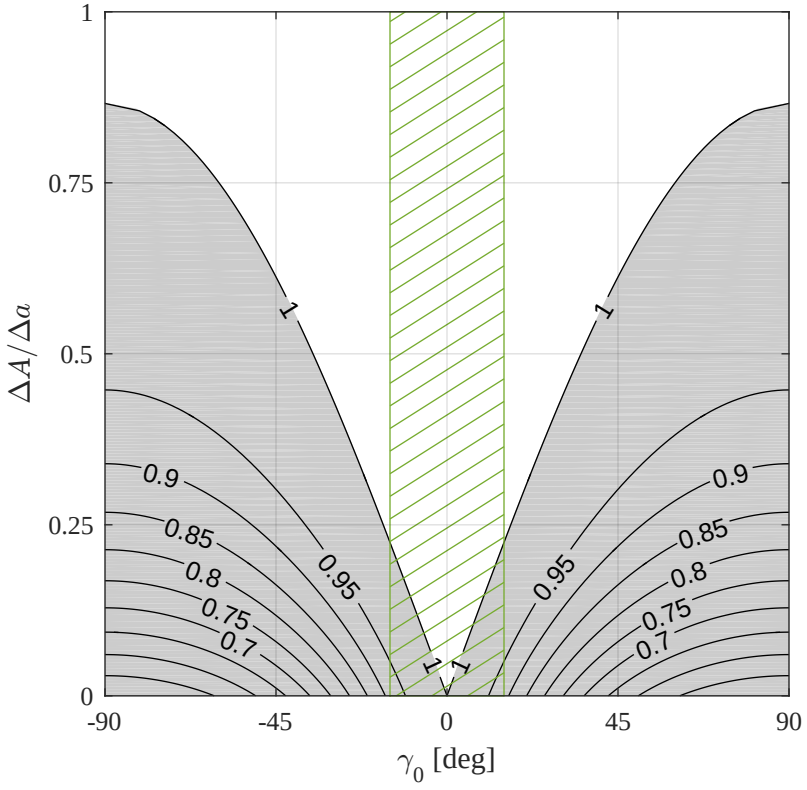

Fig. 7.2: Contours representing the ratio of the SOCP-optimal Δv to the analytic Δv as a function of γ_0 and $\Delta A/\Delta a$.

The contour line showing a 1:1 Δv ratio matches the solution to the equation

$$\cos^2 \gamma_0 = 1 - \frac{4}{3} \frac{\Delta A^2}{\Delta a^2} \tag{7.7}$$

which describes the boundary of equation (7.5). The white region outside this contour line shows the family of transfers, represented by $(\gamma_0, \Delta A/\Delta a)$ pairs, where the analytic solution is optimal. The grey region inside this contour line shows the family of transfers where analytic solution is suboptimal. The peak of this contour line occurs at $\Delta A/\Delta a = \sqrt{3}/2$, which matches equation (7.6). For an ideal orientation ($\gamma_0^{\text{ideal}} = 0°, \pm 180°$), the analytic solution is optimal for any $\Delta A/\Delta a$. The green hatched region shows what may be considered a desired operating range for the safety ellipse's orientation ($\gamma_0^{\text{ideal}} - 15° \leq \gamma_0 \leq \gamma_0^{\text{ideal}} + 15°$).

Figure 7.2 shows that as γ_0 increases, a larger $\Delta A/\Delta a$ is required for the analytic solution to remain optimal. This is due to maneuver placement. The maneuver locations are governed by desired changes to cross-track motion; for nominal resizing, the first maneuver always occurs when the chaser crosses the target's orbit plane. In-plane maneuvers are effectively coupled with an optimal cross-track maneuver sequence. Section 6.2.2 shows that the maneuver locations for an optimal in-plane transfer are, in general, different than the maneuver locations for an optimal cross-track transfer. However, they are equal when $\gamma_0 = \gamma_0^{\text{ideal}}$ and grow farther apart as γ_0 increases.

In the special case of $\gamma_0 = \gamma_0^{\text{ideal}}$, the maneuver sequence consists of strictly in-track and cross-track maneuvers. When $\gamma_0 \neq \gamma_0^{\text{ideal}}$, in-plane maneuvers require a radial component, as strictly in-track maneuvers that occur at the plane crossing cannot satisfy the terminal constraints. As γ_0 increases, so does the required radial Δv component. Radial maneuvers are less efficient than in-track maneuvers, which means that the in-plane Δv increases with γ_0 as well. The grey regions of Figure 7.2 show that instead of forcing large radial maneuvers by maneuvering at the optimal cross-track locations, a solution with a lower Δv involves changing the maneuver placement altogether.

7.2.3 Passive Safety Analysis

This section analyzes the passive safety of transfer trajectories that result from an incomplete maneuver sequence. The cases under consideration are: 1) a transfer where only the first maneuver is performed and 2) a transfer where only the first and second maneuvers are performed. These trajectories are referred to as intermediate trajectories. The ROEs of the intermediate trajectories are computed by substituting equations (7.1) and (7.4) into equations (3.11) through (3.16). For this analysis, it is assumed that the initial safety ellipse is stationary ($x_{r_0} = 0$).

The intermediate relative phase angles are

$$\gamma_k^+ = \gamma_0,\ k = 1, 2 \tag{7.8}$$

Equation (7.8) says that the maneuvers do not alter the safety ellipse's initial orientation. The intermediate in-plane semi-major axes, cross-track amplitudes, and radial components of the instantaneous center are

$$a_1^+ = a_0 + \frac{1}{4}\Delta a \tag{7.9}$$

$$a_2^+ = a_0 + \frac{3}{4}\Delta a \tag{7.10}$$

$$A_1^+ = A_0 + \frac{1}{4}\Delta A \tag{7.11}$$

$$A_2^+ = A_0 + \frac{3}{4}\Delta A \tag{7.12}$$

$$x_{r_1}^+ = \eta_2 \frac{1}{8}\Delta a \cos\gamma_0 \tag{7.13}$$

$$x_{r_2}^+ = -x_{r_1}^+ \tag{7.14}$$

From equation (A.1), the intermediate radial separations between the in-track axis and point of relative apsides are

$$d_1^+ = \frac{1}{2}\left[a_0 + \frac{1}{4}\Delta a\big(1 - \mathrm{sgn}(\Delta a)\big)\right]|\cos\gamma_0| \tag{7.15}$$

$$d_2^+ = \frac{1}{2}\left[a_0 + \frac{1}{4}\Delta a\big(3 - \mathrm{sgn}(\Delta a)\big)\right]|\cos\gamma_0| \tag{7.16}$$

When the safety ellipse is enlarged ($\Delta a > 0$, $\Delta A > 0$), a conservative keep-out region may be defined by the dimensions of the initial safety ellipse. Properties of the intermediate trajectories are

$$a_2^+ > a_1^+ > a_0 \tag{7.17}$$

$$A_2^+ > A_1^+ > A_0 \tag{7.18}$$

$$d_2^+ > d_1^+ = d_0 \tag{7.19}$$

Equations (7.17) and (7.18) indicate that the dimensions of the intermediate instantaneous ellipses are always greater than the dimensions of the initial safety ellipse, indicating that passive safety is maintained.

When the safety ellipse is reduced ($\Delta a < 0$, $\Delta A < 0$), a conservative keep-out region may be defined by the dimensions of the final safety ellipse. Properties of the intermediate trajectories are

$$a_1^+ > a_2^+ > a_f \tag{7.20}$$

$$A_1^+ > A_2^+ > A_f \tag{7.21}$$

$$d_1^+ > d_2^+ = d_f \tag{7.22}$$

Equations (7.17) and (7.18) say that the dimensions of the intermediate instantaneous ellipses are always greater than the dimensions of the final safety ellipse, indicating that passive safety is maintained.

7.2.4 A Special Case of Unconstrained In-Plane Phasing

One simplifying assumption for nominal resizing is $\Delta E = 0$. This constrains the in-plane phase angle after the transfer to equal the in-plane phase angle if no maneuvers had occurred. This section shows that when the initial and final ratios of the cross-track amplitude to in-plane semi-major axis are equal, the nominal maneuver sequence in equation (7.1) also satisfies the necessary conditions for an unconstrained ΔE. This means that

although the in-plane phase angle is allowed to be any value after the transfer, an optimal transfer occurs when $\Delta E = 0$ and equation (7.5) is satisfied.

Substituting $\Delta E = \Delta\psi = 0$ into equation (5.126), λ_{5_0} for an unconstrained ΔE is

$$\lambda_{5_0} = \sec\left(\psi_1^-\right)\left(\Delta\hat{v}_z \sin\left(\psi_0\right) + \frac{1}{2}\frac{a_f}{A_f}\left[\frac{1}{2}\Delta\hat{v}_y \sin\left(E_1^-\right) - \Delta\hat{v}_x \cos\left(E_1^-\right)\right]\cos\left(\tau_{\text{wait}}\right)\right) \tag{7.23}$$

From equation (7.4), ψ_0 and E_1^- can be written as

$$\psi_0 = -\tau_{\text{wait}} + N\pi \tag{7.24}$$

$$E_1^- = \gamma_0 + N\pi \tag{7.25}$$

Substituting equations (7.4), (7.24), and (7.25) into equation (7.23) results in

$$\lambda_{5_0} = -\Delta\hat{v}_z \sin\left(\tau_{\text{wait}}\right) + \frac{1}{2}\frac{a_f}{A_f}\left(\frac{1}{2}\Delta\hat{v}_y \sin\gamma_0 - \Delta\hat{v}_x \cos\gamma_0\right)\cos\left(\tau_{\text{wait}}\right) \tag{7.26}$$

From equation (7.1), the maneuver direction can be written as

$$\Delta\hat{\boldsymbol{v}} = \frac{\eta_2}{\|\Delta\tilde{\boldsymbol{v}}\|}\frac{1}{4}\begin{bmatrix} 2\Delta a \sin\gamma_0 & \Delta a \cos\gamma_0 & 4\Delta A \end{bmatrix}^T \tag{7.27}$$

Substituting the components of equation (7.27) into equation (7.26), λ_{5_0} for an unconstrained ΔE becomes

$$\lambda_{5_0} = \frac{\eta_2}{\|\Delta\tilde{\boldsymbol{v}}\|}\left(-\Delta A \sin\left(\tau_{\text{wait}}\right) - \frac{3}{16}\frac{a_f}{A_f}\Delta a \sin\gamma_0 \cos\gamma_0 \cos\left(\tau_{\text{wait}}\right)\right) \tag{7.28}$$

Substituting the components of equation (7.27) into equation (5.103), λ_{5_0} for a constrained ΔE is

$$\lambda_{5_0} = \frac{\eta_2}{\|\Delta\tilde{\boldsymbol{v}}\|}\left(-\Delta A \sin\left(\tau_{\text{wait}}\right) - \frac{3}{16}\frac{\Delta a^2}{\Delta A}\sin\gamma_0 \cos\gamma_0 \cos\left(\tau_{\text{wait}}\right)\right) \tag{7.29}$$

From Section 5.2, equation (7.29) results in a primer vector that satisfies the necessary conditions when equation (7.5) holds. Equations (7.28) and (7.29) are equivalent when

$$\frac{a_f}{A_f} = \frac{\Delta a}{\Delta A} \tag{7.30}$$

Equation (7.30) is true when

$$\frac{a_0}{A_0} = \frac{a_f}{A_f} \tag{7.31}$$

Therefore, satisfying equation (7.31) results in a λ_{5_0} that satisfies the primer vector conditions when equation (7.5) holds, as well as the transversality conditions for an unconstrained ΔE. This means that for an unconstrained ΔE, an optimal solution is given by the maneuver sequence in Section 7.2.1, provided equations (7.31) and (7.5) are true.

7.3 Off-Nominal

Figure 7.3 shows an example of off-nominal safety ellipse resizing. The sequence of events is the same as the description in Section 7.1. For clarity, the coasting motion of the initial safety ellipse is only plotted for three orbit periods.

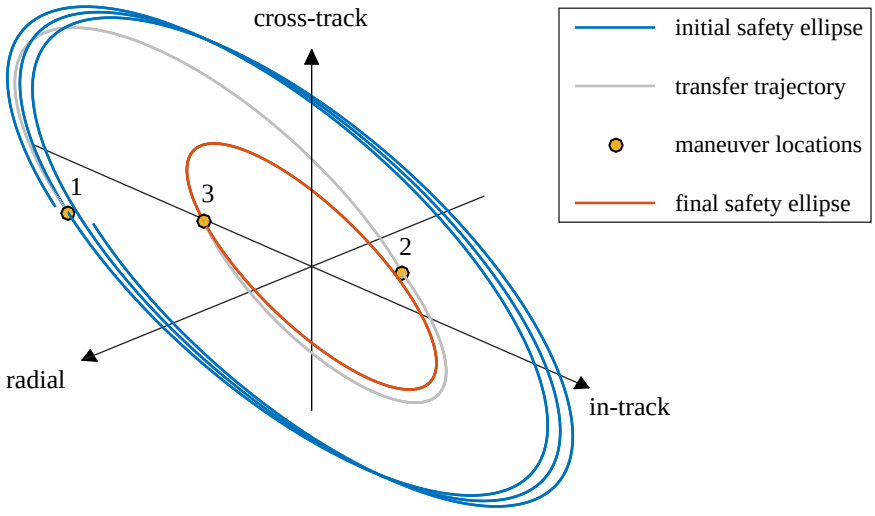

Fig. 7.3: An example of off-nominal safety ellipse resizing.

The off-nominal resizing scenario ignores the simplifying assumptions made in Section 7.2. In addition to changing the dimensions of the initial safety ellipse, the maneuver sequence makes small changes to the instantaneous center, in-plane phase angle, and orientation. Changes to the instantaneous center are most apparent in Figure 7.3; the initial safety ellipse is drifting due to a nonzero radial offset, while the final safety ellipse is stationary and centered about the origin of the LVLH frame.

7.3.1 Instantaneous Center Changes and Optimality

Section 5.1.5 derived bounds on the allowable changes to the instantaneous center that do not affect optimality for a general reconfiguration. This section approximates these bounds specifically for resizing. Approximations are made to reduce the expressions for these bounds to functions of $x_{r_1}^-$, $y_{r_1}^-$, and Δa. Due to the decoupling of in-plane and out-of-plane motion, instantaneous center changes are independent of cross-track maneuvers.

This analysis assumes that the maneuver sequence removes the drift rate at the final time ($x_{r_f} = 0$). It also assumes $\Delta E = \Delta\gamma = 0$ and $\gamma_0 = \gamma_0^{\text{ideal}}$. These assumptions lead to

$$\Delta\tilde{v}_x = 0,\ \Delta\tilde{v}_y = \pm\frac{1}{4}\eta_2\Omega\Delta a \tag{7.32}$$

The sign ambiguity in equation (7.32) is due to whether $\gamma_0^{\text{ideal}} = 0°, \pm 180°$. Substituting equation (7.32) into equations (5.90) through (5.92), a costate solution exists when

$$\pm\frac{\eta_2}{\Delta a}\left(6x_{r_1}^- + \frac{8}{3\pi}\Delta y_{r_1}^-\right) \leq 1 \tag{7.33}$$

$$\pm\frac{\eta_2}{\Delta a}2x_{r_1}^- \geq -1 \tag{7.34}$$

$$\pm\frac{\eta_2}{\Delta a}\left(2x_{r_1}^- + \frac{8}{3\pi}\Delta y_{r_1}^-\right) \geq -1 \tag{7.35}$$

$x_{r_1}^-$ is the radial component of the instantaneous center immediately before the first maneuver. $\Delta y_{r_1}^-$ is the difference between the desired final in-track component of the instantaneous center and its value immediately before the first maneuver.

Equations (7.33) through (7.35) define polyhedrons in $(x_{r_1}^-, \Delta y_{r_1}^-)$ space that are functions of η_2, γ_0^{ideal}, and Δa. Figure 7.4 plots these polyhedrons. They represent, for particular values of η_2 and γ_0^{ideal}, an approximate region of allowable instantaneous center changes immediately before the first maneuver that do not affect optimality of the analytic solution.

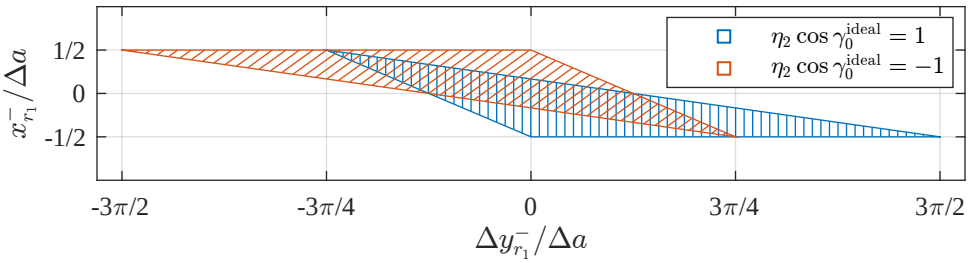

Fig. 7.4: Region approximating allowable $(x_{r_1}^-, \Delta y_{r_1}^-)$ pairs that do not affect optimality for particular values of η_2 and γ_0^{ideal}.

The intersection of these sets is shown in Figure 7.5. This region is independent of the sign of the maneuver direction.

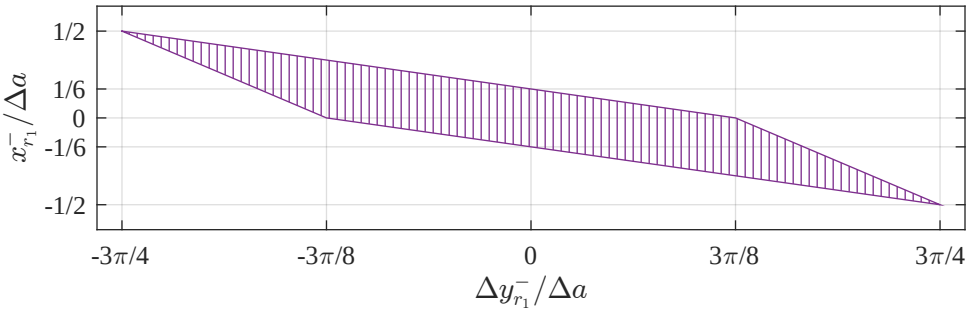

Fig. 7.5: Region approximating allowable $(x_{r_1}^-, \Delta y_{r_1}^-)$ pairs that do not affect optimality.

Figure 7.5 shows that the allowable instantaneous center changes are proportional to Δa. It also shows that optimality is less sensitive to changes in y_r than x_r.

7.3.2 Monte Carlo Analysis

Off-nominal resizing is a general reconfiguration where the dominant component is a change in the safety ellipse's dimensions. The maneuver sequence is computed using the equations in Sections 5.1.2 through 5.1.4. Compared to nominal resizing, these equations are much more difficult to analyze analytically. Instead, Monte Carlo methods are used to test optimality and passive safety. Six test cases are conducted with each test case consisting of 250 samples.

Each individual Monte Carlo sample is a particular off-nominal resizing scenario, and the transfer trajectory is computed both numerically and analytically. The problem is solved numerically using the SOCP in equation (4.52) with a fixed final time of multiple orbit periods to emulate the free-time problem.

General Setup

The Monte Carlo simulation relies on first defining an initial nominal safety ellipse. Table 7.1 lists the ROEs of the initial nominal safety ellipse that are consistent across all test cases.

Table 7.1: ROEs of the initial nominal safety ellipse for all test cases.

$x_{r_0}^n$ [m]	$y_{r_0}^n$ [m]	E_0^n [deg]	γ_0^n [deg]
0	0	$\mathcal{U}(-180, 180)$	0

The subscript 'n' denotes a nominal value. The initial nominal safety ellipse is always stationary, centered, and ideally oriented. The initial in-plane phase angle is drawn from a uniform distribution, $\mathcal{U}$, which randomizes the chaser's initial location along the safety ellipse.

The ROEs of the initial off-nominal safety ellipse are computed by adding dispersions to the ROEs of the initial nominal safety ellipse. The dispersions are drawn from zero-mean

Gaussian distributions. The ROEs of the initial off-nominal safety ellipse are

$$x_{r_0} = x_{r_0}^n + \delta x_{r_0} \tag{7.36}$$

$$y_{r_0} = y_{r_0}^n + \delta y_{r_0} \tag{7.37}$$

$$a_0 = a_0^n + \delta a_0 \tag{7.38}$$

$$E_0 = E_0^n + \delta \Delta E \tag{7.39}$$

$$A_0 = A_0^n + \delta A_0 \tag{7.40}$$

$$\gamma_0 = \gamma_0^n + \delta \gamma_0 \tag{7.41}$$

where the variable $\delta(\cdot)$ is defined as a normally distributed random variable with zero mean and a variance denoted by $\sigma_{(\cdot)}^2$:

$$\delta(\cdot) := \mathcal{N}\left(0, \sigma_{(\cdot)}^2\right) \tag{7.42}$$

From the information in Table 7.1, equations (7.36), (7.37), and (7.41) simplify to

$$x_{r_0} = \delta x_{r_0},\ y_{r_0} = \delta y_{r_0},\ \gamma_0 = \delta \gamma_0 \tag{7.43}$$

Computing a transfer trajectory requires defining a final desired safety ellipse. Table 7.2 lists the ROEs of the final desired safety ellipse that are consistent across all test cases.

Table 7.2: ROEs of the final desired safety ellipse for all test cases.

x_{r_f} [m]	y_{r_f} [m]	E_f [deg]	γ_f [deg]
0	0	E_f^n	0

The final desired safety ellipse is always stationary, centered, and ideally oriented. The variable E_f^n is defined as

$$E_f^n := E_0^n + \tau_f - \tau_0 \tag{7.44}$$

Substituting equations (7.44) and (7.39) into equation (4.9), the desired change in the in-plane phase angle is

$$\Delta E = -\delta\Delta E \tag{7.45}$$

Substituting x_{r_0} from equation (7.43) into equation (5.84), the radial component of the instantaneous center immediately before the first maneuver is

$$x_{r_1}^- = \delta x_{r_0} \tag{7.46}$$

Substituting x_{r_0} and y_{r_0} from equation (7.43) into equation (5.86) and applying the information from Table 7.2, the difference between the desired final in-track component of the instantaneous center and its value immediately before the first maneuver is

$$\Delta y_{r_1}^- = \frac{3}{2}(\tau_{\text{wait}})\delta x_{r_0} - \delta y_{r_0} \tag{7.47}$$

Test Cases

Table 7.3 lists the initial nominal and final desired in-plane semi-major axis and cross-track amplitude and the nominal ratio of the desired change in cross-track amplitude to in-plane semi-major axis for each test case.

Table 7.3: In-plane semi-major axis and cross-track amplitude values for each test case.

case #	a_0^n [m]	A_0^n [m]	a_f [m]	A_f [m]	$\Delta A^n/\Delta a^n$
1	1000	500	500	250	0.50
2	1000	500	250	250	0.33
3	1000	500	500	333	0.33
4	100	50	500	125	0.19
5	100	50	500	100	0.13
6	1000	500	750	250	1.00

The nominal changes in the in-plane semi-major axis and cross-track amplitude are

$$\Delta a^n = a_f - a_0^n,\ \Delta A^n = A_f - A_0^n \tag{7.48}$$

Table 7.4 lists the variances of the Gaussian distributions in equations (7.36) through (7.41) in terms of 3-σ values for each test case.

Table 7.4: 3-σ ROE dispersions for each test case.

case #	x_{r_0} [m]	y_{r_0} [m]	a_0 [m]	ΔE [deg]	A_0 [m]	γ_0 [deg]
1-3, 6	50	100	100	15	50	15
4, 5	5	10	10	15	5	15

The dispersions on x_{r_0}, y_{r_0}, and a_0 are proportional to a_0^n, and the dispersions on A_0 are proportional to A_0^n. In contrast, the dispersions on ΔE and γ_0 are independent of the safety ellipse's dimensions and remain constant across all test cases.

Test cases 1 through 5 focus on optimality in terms of the primer vector conditions. For nominal resizing, the primer vector conditions were shown to be a function of only γ_0 and $\Delta A/\Delta a$. Figure 7.2 also showed that there are regions in $(\gamma_0, \Delta A/\Delta a)$ space where the analytic solution is suboptimal but requires nearly the same Δv as the numerical solution. The test cases are chosen to show how additional parameters affect optimality. More importantly, they indicate whether the nominal primer vector conditions and trends shown in Figure 7.2 remain a good approximation for off-nominal scenarios.

Test case 6 focuses on the effect of instantaneous center changes on optimality. For cases 1 through 5, Δa^n is specified such that the 3-σ bounds on $x_{r_1}^-$ and $\Delta y_{r_1}^-$ are inside the region shown in Figure 7.5. For case 6, the 3-σ bounds on $x_{r_1}^-$ and $\Delta y_{r_1}^-$ exceed this region. Figure 7.6 shows the 3-σ bounds on x_r^- and Δy_r^- for $\tau_{\text{wait}} = 0$ (solid) and $\tau_{\text{wait}} = \pi$ (dashed) plotted over the approximate allowable $(x_{r_1}^-, \Delta y_{r_1}^-)$ region for test cases 1 (blue) and 6 (red). These regions are computed using Δa^n. The covariance ellipses are computed from equations (7.46) and (7.47).

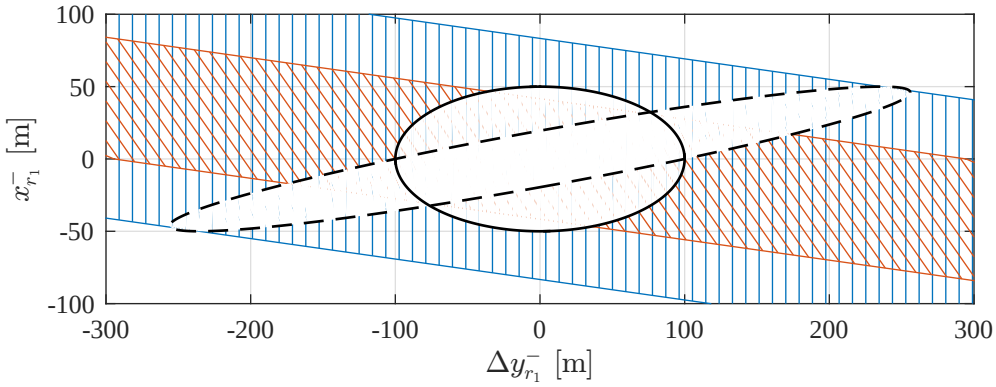

Fig. 7.6: 3-σ bounds on $x_{r_1}^-$ and $\Delta y_{r_1}^-$ for $\tau_{\text{wait}} = 0$ (solid) and $\tau_{\text{wait}} = \pi$ (dashed) plotted over the approximate allowable $(x_{r_1}^-, \Delta y_{r_1}^-)$ region for test cases 1 (blue) and 6 (red).

Figure 7.6 shows that for test case 6, a large initial radial offset is required for a sample to fall outside the $(x_{r_1}^-, \Delta y_{r_1}^-)$ region, and the combination of a large $|x_{r_0}|$ and τ_{wait} increases the likelihood of a suboptimal analytic solution.

Results

Table 7.5 lists the percentage of samples in which the analytic solution is optimal and the minimum ratio of the Δv from the SOCP solution to the Δv from the analytic solution for each test case.

Table 7.5: Percentage of optimal samples and minimum ratio of the numerical Δv to the analytic Δv for each test case.

case #	% of optimal samples	$\min(\Delta v_{\text{num}}/\Delta v_{\text{ana}})$
1	99.6	0.9996
2	98.4	0.9957
3	85.6	0.9808
4	100	1.0000
5	86.8	0.9828
6	96.8	0.7374

For test cases 1 through 5, every suboptimal sample is caused by violating the primer vector condition $p \leq 1$. The resulting Δv penalty is small–a maximum of roughly 2% across these test cases. This is consistent with the trends of Figure 7.2. Cases 2 through 4 show that the primer vector conditions are affected by parameters other than γ_0 and $\Delta A/\Delta a$. For example, $\Delta A^n/\Delta a^n$ is equal for cases 2 and 3, yet case 3 has considerably more suboptimal samples. Case 4 has a lower $\Delta A^n/\Delta a^n$ than both case 2 and 3, yet all if its samples are optimal. However, the key takeaway from cases 1 through 5 is that even though optimality is more difficult to guarantee, the suboptimal analytic solution requires nearly the same Δv as the numerical solution.

For test case 6, every suboptimal sample is caused by too large an instantaneous center correction which results in a nonexistent costate solution. The resulting Δv penalty can be much larger than in cases that violate the primer vector conditions–a maximum of roughly 25% for this test case.

Figure 7.7 shows each sample of $x_{r_1}^-$ and $\Delta y_{r_1}^-$ plotted over the region approximating their allowable values for test case 6. The markers indicate whether the analytic solution is optimal (dot = optimal, x's = suboptimal), and the colors denote the sign of the maneuver direction (black = positive, blue = negative).

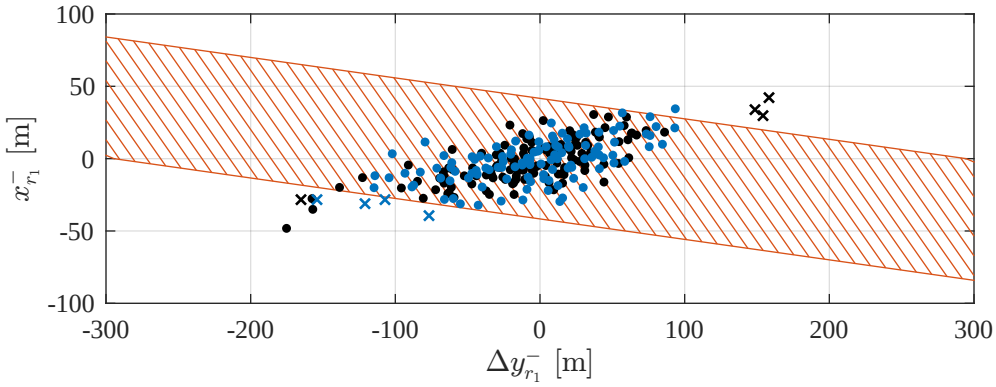

Fig. 7.7: $x_{r_1}^-$ and $\Delta y_{r_1}^-$ samples plotted over the approximate allowable $(x_{r_1}^-, \Delta y_{r_1}^-)$ region for test case 6. The markers denote optimality (dots = optimal, x's = suboptimal), and the colors denote the sign of the maneuver direction (blue = positive, black = negative).

Figure 7.7 shows that the suboptimal samples are outside the approximate allowable $(x_{r_1}^-, \Delta y_{r_1}^-)$ region. However, not all samples outside this region are suboptimal. One of the reasons for this trend is that, as Figure 7.4 shows, the $(x_{r_1}^-, \Delta y_{r_1}^-)$ region is the intersection of two larger regions that depend on the sign of the maneuver direction. This explains the correlation between the sign of the maneuver direction and whether a sample located outside the $(x_{r_1}^-, \Delta y_{r_1}^-)$ region is optimal.

Tables 7.6 and 7.7 list the minimum radial separation between the in-track axis and point of relative apsides and the maximum relative phase angle for test cases involving safety ellipse reduction (Table 7.6) and enlargement (Table 7.7).

Table 7.6: Passive safety parameters for safety ellipse reduction test cases.

case #	$\min(d_2^+/a_f)$	$\max(\lvert\gamma_2^+\rvert)$ [deg]
1	0.49	5.5°
2	0.49	7.3°
3	0.49	5.2°
6	0.47	6.6°

Table 7.7: Passive safety parameters for safety ellipse enlargement test cases.

case #	$\min(d_1^+/a_0)$	$\max(\lvert\gamma_1^+\rvert)$ [deg]
4	0.46	7.2°
5	0.47	9.9°

The results in Tables 7.6 and 7.7 show that the intermediate trajectories across all test cases are passively safe. Also, the minimum values for d_2^+/a_f and d_1^+/a_0 show close agreement to the nominal values in equations (7.19) and (7.22).

7.4 Summary

This chapter focused on safety ellipse resizing, which is a reconfiguration where the dominant component is a change in the safety ellipse's dimensions. A simplified version of the problem, referred to as nominal resizing, was first considered. The simplifying assumptions allow for an analytic analysis of optimality and passive safety. One key result from this analysis is an equation that relates optimality to the safety ellipse's initial orientation and ratio of the desired change in cross-track amplitude to the desired change in in-plane semi-major axis. This analysis also showed that the nominal transfer trajectories are passively safe. A version of the problem without simplifying assumptions, referred to as off-nominal resizing, was then considered. Monte Carlo methods were used to analyze optimality and passive safety. The results showed that the analytic solution generated both fuel-optimal and passively safe transfer trajectories for a range of practical off-nominal resizing scenarios.

CHAPTER 8

SAFETY ELLIPSE PHASING

8.1 Overview

Figure 8.1 shows an example of nominal safety ellipse phasing. The maneuver sequence is indicated by the numbers above each maneuver location. Before maneuver 1, the chaser travels clockwise along the initial safety ellipse, making one revolution every orbit period. Maneuver 1 initiates the transfer trajectory. Maneuver 2 alters the transfer trajectory to make it intersect the initial safety ellipse at the time of maneuver 3, which occurs an orbit period after maneuver 1. Maneuver 3 places the chaser back onto the initial safety ellipse ahead of point 1, the location it would have coasted to without maneuvering. The chaser remains on the safety ellipse, traveling clockwise, until another maneuver is performed.

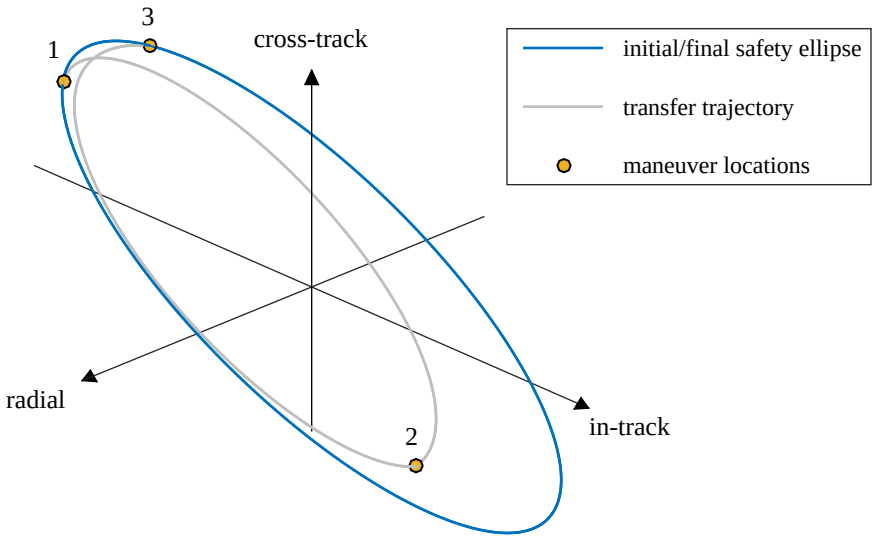

Fig. 8.1: An example of nominal safety ellipse phasing.

The objective of phasing is to make a change in the chaser's location along the safety ellipse that is large in comparison to changes in the safety ellipse's dimensions, orientation, and instantaneous center. This chapter analyzes the phasing problem by dividing it into two categories: nominal and off-nominal.

The nominal phasing scenario involves simplifying assumptions that lead to an idealized version of the problem. Although these assumptions remove realism, they also simplify the expressions for Δv vectors and maneuver times to where analysis of optimality and passive safety can be performed analytically. One key result from this analysis is an equation that relates optimality to the safety ellipse's initial orientation and initial ratio of the cross-track amplitude to in-plane semi-major axis. This equation is presented in Section 8.2.1 and numerically validated in Section 8.2.2. Section 8.2.3 shows that the nominal transfer trajectories are passively safe as long as the desired phase angle change is not near $\pm 180°$. Section 8.2.4 shows that when the initial and final ratios of the cross-track amplitude to in-plane semi-major axis are equal, the equation relating optimality to properties of the initial safety ellipse is identical to the equation in Section 8.2.1. The assumption of equal ratios describes a special case of combined phasing and resizing.

The off-nominal phasing scenario makes no simplifying assumptions. It is a general reconfiguration where the dominant component is a change in the chaser's location along the safety ellipse. Section 8.3.1 presents equations which approximate the allowable changes to the instantaneous center that do not affect optimality of the analytic solution. Section 8.3.2 analyzes the optimality and passive safety of off-nominal phasing scenarios using Monte Carlo methods.

8.2 Nominal

Nominal phasing is a simplified case of a general reconfiguration. It has the following characteristics:

1) The instantaneous center after the transfer trajectory is equal to the instantaneous center if no maneuvers had occurred ($\Delta x_r = 0$ and $\Delta y_r = 0$).

2) The dimensions after the transfer are equal to the dimensions before the transfer ($a_f = a_0$ and $A_f = A_0$).

3) The orientation after the transfer is equal to the orientation before the transfer ($\Delta\gamma = 0$).

8.2.1 Maneuver Sequence and Primer Vector Analysis

Substituting $\Delta x_r = \Delta y_r = \Delta\gamma = 0$, $a_f = a_0$, and $A_f = A_0$ into equations (5.60), (5.62) through (5.64), and (5.74) and (5.76), the Δv vectors are

$$\Delta\boldsymbol{v}_1 = -\eta_2 \frac{\Omega}{8} \left|\sin\left(\tfrac{1}{2}\Delta E\right)\right| \begin{bmatrix} 2a_0 \sin\gamma_0 & a_0\cos\gamma_0 & 4A_0 \end{bmatrix}^T, \; \Delta\boldsymbol{v}_2 = -2\Delta\boldsymbol{v}_1, \; \Delta\boldsymbol{v}_3 = \Delta\boldsymbol{v}_1 \tag{8.1}$$

Substituting $\Delta\gamma = 0$ and $A_f = A_0$ into equation (5.27), the cross-track phase angle immediately before the first maneuver is

$$\psi_1^- = N\pi + \begin{cases} \frac{1}{2}(\pi - \Delta E) & \Delta E > 0 \\ -\frac{1}{2}(\pi + \Delta E) & \Delta E < 0, \end{cases} \qquad N \in \mathbb{Z} \tag{8.2}$$

Equation (8.2) says that the first maneuver occurs at the point of largest cross-track separation, offset by $\Delta E/2$.

Substituting equation (8.1) into equation (5.109), the primer vector conditions are satisfied when

$$\cos^2\gamma_0 \geq 1 - \frac{4}{3}\frac{A_0^2}{a_0^2} \tag{8.3}$$

Equation (8.3) says that optimality depends on the safety ellipse's initial orientation and initial ratio of the cross-track amplitude to in-plane semi-major axis. The primer vector conditions are satisfied for all orientations when

$$\frac{A_0}{a_0} \geq \frac{\sqrt{3}}{2} \tag{8.4}$$

8.2.2 Numerical Validation

The primer vector analysis is validated numerically. A family of nominal phasing cases, distinguished by different values of γ_0 and A_0/a_0, are solved both numerically and analytically (as equation (8.3) shows, optimality is independent of ΔE). The problem is solved numerically using the SOCP in equation (4.52) with a fixed final time of multiple orbit periods to emulate the free-time problem. Figure 8.2 shows a contour plot with level sets that represent the ratio of the Δv from the SOCP solution to the Δv from the analytic solution as a function of γ_0 and A_0/a_0. This plot is identical when γ_0 is shifted by $\pm 180°$.

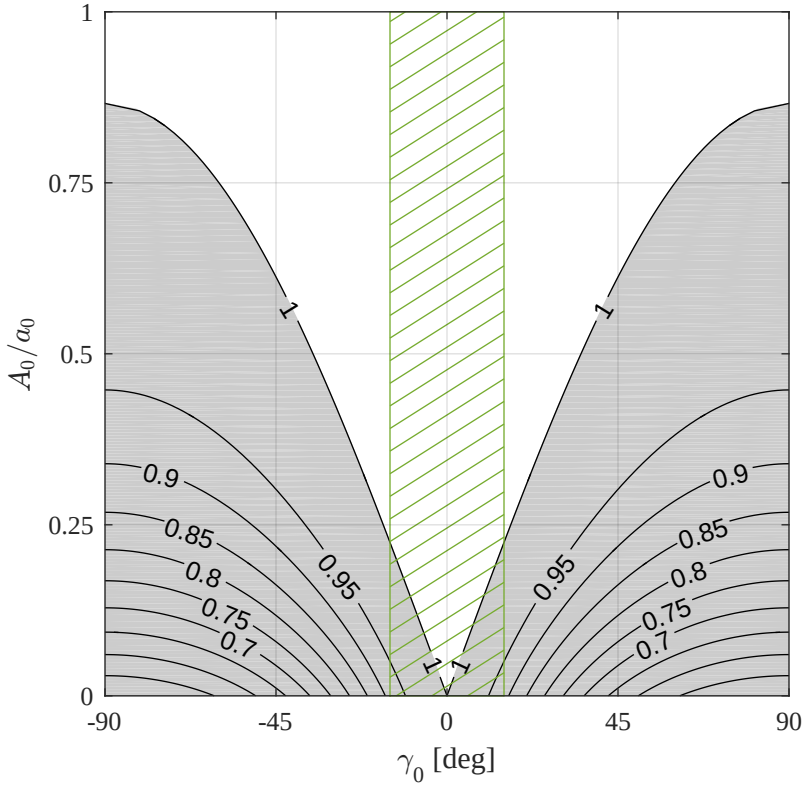

Fig. 8.2: Contours representing the ratio of the SOCP-optimal Δv to the analytic Δv as a function of γ_0 and A_0/a_0.

The contour line showing a 1:1 Δv ratio matches the solution to the equation

$$\cos^2 \gamma_0 = 1 - \frac{4}{3}\frac{A_0^2}{a_0^2} \tag{8.5}$$

which describes the boundary of equation (8.3). The white region outside this contour line shows the family of transfers, represented by $(\gamma_0, A_0/a_0)$ pairs, where the analytic solution is optimal. The grey region inside this contour line shows the family of transfers where the analytic solution is suboptimal. The peak of this contour line occurs at $A_0/a_0 = \sqrt{3}/2$, which matches equation (8.4). For an ideal orientation ($\gamma_0^{\text{ideal}} = 0°, \pm 180°$), the analytic solution is optimal for any A_0/a_0. The green hatched region shows what may be considered a desired operating range for the safety ellipse's orientation ($\gamma_0^{\text{ideal}} - 15° \leq \gamma_0 \leq \gamma_0^{\text{ideal}} + 15°$).

Figure 8.2 shows that as γ_0 increases, a larger A_0/a_0 is required for the analytic solution to remain optimal. Section 7.2.2 discusses the cause of this behavior, which is consistent for both resizing and phasing.

8.2.3 Passive Safety Analysis

This section analyzes the passive safety of transfer trajectories that result from an incomplete maneuver sequence. The cases under consideration are: 1) a transfer where only the first maneuver is performed and 2) a transfer where only the first and second maneuvers are performed. These trajectories are referred to as intermediate trajectories. The ROEs of the intermediate trajectories are computed by substituting equations (8.1) and (8.2) into equations (3.11) through (3.16). For this analysis, is assumed that the initial safety ellipse is stationary ($x_{r_0} = 0$).

The intermediate relative phase angles are

$$\gamma_k^+ = \gamma_0, \; k = 1, 2 \tag{8.6}$$

Equation (8.6) says that the maneuvers do not alter the safety ellipse's initial orientation. The intermediate in-plane semi-major axes and cross-track amplitudes are

$$a_k^+ = \frac{1}{2}a_0\sqrt{1+3\cos^2\left(\tfrac{1}{2}\Delta E\right)},\ k=1,2 \tag{8.7}$$

$$A_k^+ = \frac{1}{2}A_0\sqrt{1+3\cos^2\left(\tfrac{1}{2}\Delta E\right)},\ k=1,2 \tag{8.8}$$

Equations (8.7) and (8.8) indicate that $\min(a_k^+) = a_0/2$ and $\min(A_k^+) = A_0/2$, which occurs when $\Delta E = \pm 180°$. The intermediate radial components of the instantaneous center are

$$x_{r_1}^+ = -\eta_2\frac{1}{4}a_0|\sin\left(\tfrac{1}{2}\Delta E\right)|\cos\gamma_0 \tag{8.9}$$

$$x_{r_2}^+ = -x_{r_1}^+ \tag{8.10}$$

From equation (A.1), the intermediate radial separations between the in-track axis and point of relative apsides are

$$d_k^+ = \frac{1}{4}a_0\left[\sqrt{1+3\cos^2\left(\tfrac{1}{2}\Delta E\right)} - |\sin\left(\tfrac{1}{2}\Delta E\right)|\right]|\cos\gamma_0|,\ k=1,2 \tag{8.11}$$

d_k^+/a_0 as a function of $|\Delta E|$ for different values of γ_0 is plotted in Figure 8.3

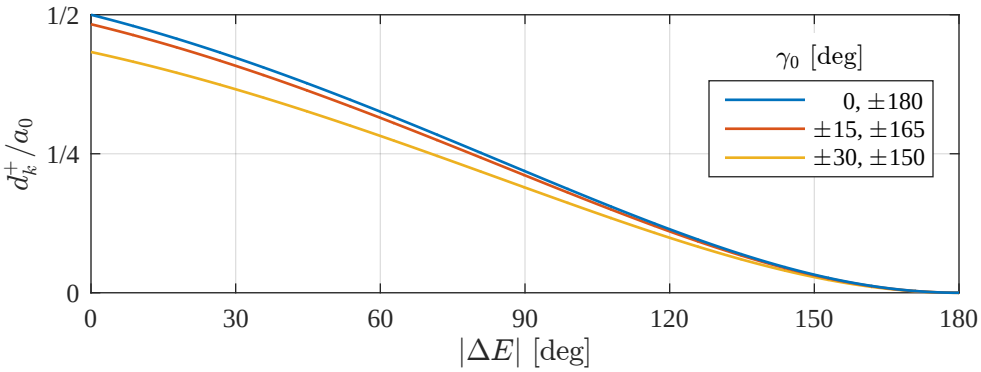

Fig. 8.3: d_k^+/a_0 as a function of ΔE for different values of γ_0.

Figure 8.3 shows that as ΔE approaches $\pm 180°$, d_k^+ approaches 0. It also shows that this trend has a low sensitivity to small values of γ_0. Therefore, for the intermediate trajectories to remain passively safe, desired phase angle changes near $\pm 180°$ should be avoided.

8.2.4 A Special Case of Combined Phasing and Resizing

In Section 8.2.1, equation (8.3) is derived by assuming $a_f = a_0$ and $A_f = A_0$. This section shows that equation (8.3) still holds when the initial and final ratios of the cross-track amplitude to in-plane semi-major axis are equal. The property $A_0/a_0 = A_f/a_f$, which does not require $a_0 = a_f$ and $A_0 = A_f$, applies to special cases of combined nominal phasing and resizing.

Substituting $\Delta\gamma = 0$ and $\Delta\psi = \Delta E$ into equations (5.63) and (5.62) results in

$$\Delta\tilde{v}_x = \frac{\Omega^2}{2\Delta\tilde{v}_z}\Big[\big(a_0A_0 + a_fA_f - (a_0A_f + a_fA_0)\cos\Delta E\big)\sin\gamma_0 + (a_0A_f - a_fA_0)\sin\Delta E\cos\gamma_0\Big] \tag{8.12}$$

$$\Delta\tilde{v}_z = \eta\Omega\sqrt{A_0^2 - 2A_0A_f\cos\Delta E + A_f^2} \tag{8.13}$$

Applying $A_0/a_0 = A_f/a_f$ to equation (8.12) leads to

$$\Delta\tilde{v}_x = \frac{\Omega^2}{2\Delta\tilde{v}_z}\frac{a_0}{A_0}\left(A_0^2 - 2A_0A_f\cos\Delta E + A_f^2\right)\sin\gamma_0 \tag{8.14}$$

Substituting equations (8.12) and (8.13) into equation (5.109), the primer vector conditions are satisfied when

$$\cos^2\gamma_0 \geq 1 - \frac{4}{3}\frac{A_0^2}{a_0^2} \tag{8.15}$$

which matches equation (8.3).

8.3 Off-Nominal

Figure 8.4 shows an example of off-nominal safety ellipse phasing. The sequence of events is the same as the description in Section 8.1. For clarity, the coasting motion of the initial safety ellipse is only plotted for three orbit periods.

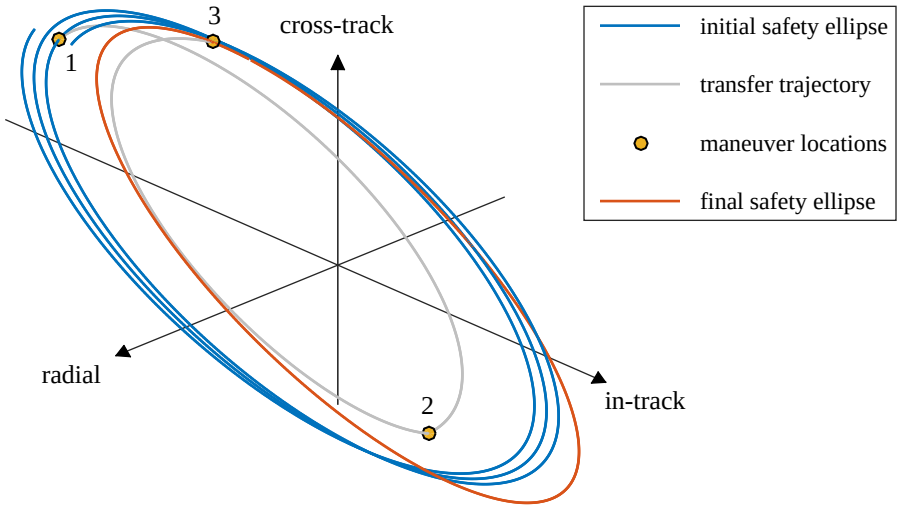

Fig. 8.4: An example of off-nominal safety ellipse phasing.

The off-nominal phasing scenario ignores the simplifying assumptions made in Section 8.2. In addition to changing the chaser's location along the initial safety ellipse, the maneuver sequence makes small changes to the instantaneous center, dimensions, and orientation. Changes to the instantaneous center are most apparent in Figure 8.4; the initial safety ellipse is drifting due to a nonzero radial offset, while the final safety ellipse is stationary and centered about the origin of the LVLH frame.

8.3.1 Instantaneous Center Changes and Optimality

Section 5.1.5 derived bounds on the allowable instantaneous center changes that do not affect optimality for a general reconfiguration. This section approximates these bounds specifically for phasing. Approximations are made to reduce the expressions for these bounds to functions of $x_{r_1}^-$, $y_{r_1}^-$, a_0, and ΔE. Due to the decoupling of in-plane and out-of-plane motion, instantaneous center changes are independent of cross-track maneuvers.

This analysis assumes that the maneuver sequence removes the drift rate at the final time ($x_{r_f} = 0$). It also assumes $\Delta a = \Delta A = \Delta\gamma = 0$ and $\gamma_0 = \gamma_0^{\text{ideal}}$. These assumptions

lead to

$$\Delta\tilde{v}_x = 0,\ \Delta\tilde{v}_y = \pm\eta_2 \frac{\Omega}{2} a_0 \left|\sin\left(\tfrac{1}{2}\Delta E\right)\right| \tag{8.16}$$

The sign ambiguity in equation (8.16) is due to whether $\gamma_0^{\text{ideal}} = 0°, \pm 180°$. Substituting equation (8.16) into equations (5.90) through (5.92), a costate solution exists when

$$\pm\frac{\eta_2}{\alpha}\left(3x_{r_1}^- + \frac{4}{3\pi}\Delta y_{r_1}^-\right) \leq 1 \tag{8.17}$$

$$\pm\frac{\eta_2}{\alpha} x_{r_1}^- \geq -1 \tag{8.18}$$

$$\pm\frac{\eta_2}{\alpha}\left(2x_{r_1}^- + \frac{4}{3\pi}\Delta y_{r_1}^-\right) \geq -1 \tag{8.19}$$

where

$$\alpha = a_0 \left|\sin\left(\tfrac{1}{2}\Delta E\right)\right| \tag{8.20}$$

$x_{r_1}^-$ is the radial component of the instantaneous center immediately before the first maneuver. $\Delta y_{r_1}^-$ is the difference between the desired in-track component of the instantaneous center and its value immediately before the first maneuver.

Equations (8.17) through (8.19) define polyhedrons in $(x_{r_1}^-, \Delta y_{r_1}^-)$ space that are functions of η_2, γ_0^{ideal}, and α. Figure 8.5 plots these polyhedrons. They represent, for particular values of η_2 and γ_0^{ideal}, an approximate region of allowable instantaneous center changes immediately before the first maneuver that do not affect optimality of the analytic solution.

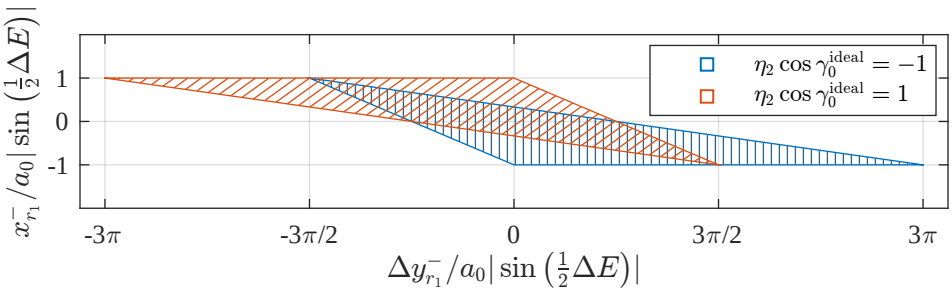

Fig. 8.5: Region approximating allowable $(x_{r_1}^-, \Delta y_{r_1}^-)$ pairs that do not affect optimality for particular values of η_2 and γ_0^{ideal}.

The intersection of these sets is shown in Figure 8.6. This region is independent of the sign of the maneuver direction.

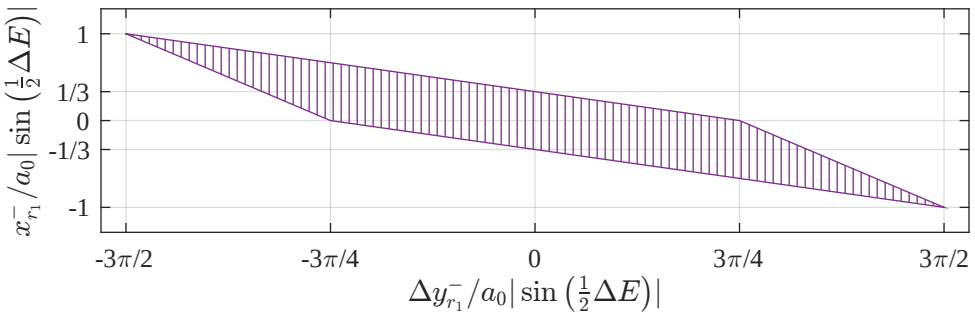

Fig. 8.6: Region approximating allowable $(x_{r_1}^-, y_{r_1}^-)$ pairs that do not affect optimality.

Figure 7.5 shows that the allowable instantaneous center changes are proportional to a_0 and ΔE. It also shows that optimality is less sensitive to changes in y_r than x_r.

8.3.2 Monte Carlo Analysis

Off-nominal phasing is a general reconfiguration where the dominant component is a change in the chaser's location along the safety ellipse. The maneuver sequence is computed using the equations in Sections 5.1.2 through 5.1.4. Compared to nominal phasing, these equations are much more difficult to analyze analytically. Instead, Monte Carlo methods are used to analyze optimality and passive safety. Six test cases are conducted with each test case consisting of 250 samples.

Each individual Monte Carlo sample is a particular off-nominal phasing scenario, and the transfer trajectory is computed both numerically and analytically. The problem is solved numerically using the SOCP in equation (4.52) with a fixed final time of multiple orbit periods to emulate the free-time problem.

General Setup

The Monte Carlo simulation relies on first defining an initial nominal safety ellipse. Table 8.1 lists the ROEs of the initial nominal safety ellipse that are consistent across all test cases.

Table 8.1: ROEs of the initial nominal safety ellipse for all test cases.

$x_{r_0}^n$ [m]	$y_{r_0}^n$ [m]	E_0^n [deg]	γ_0^n [deg]
0	0	$\mathcal{U}(-180, 180)$	0

The subscript 'n' denotes a nominal value. The initial nominal safety ellipse is always stationary, centered, and ideally oriented. The initial in-plane phase angle is drawn from a uniform distribution, $\mathcal{U}$, which randomizes the chaser's initial location along the safety ellipse.

The ROEs of the initial off-nominal safety ellipse are computed by adding dispersions to the ROEs of the initial nominal safety ellipse. The dispersions are drawn from zero-mean Gaussian distributions. The ROEs of the off-nominal safety ellipse are

$$x_{r_0} = x_{r_0}^n + \delta x_{r_0} \tag{8.21}$$

$$y_{r_0} = y_{r_0}^n + \delta y_{r_0} \tag{8.22}$$

$$a_0 = a_0^n + \delta a_0 \tag{8.23}$$

$$E_0 = E_0^n + \delta \Delta E \tag{8.24}$$

$$A_0 = A_0^n + \delta A_0 \tag{8.25}$$

$$\gamma_0 = \gamma_0^n + \delta \gamma_0 \tag{8.26}$$

where the variable $\delta(\cdot)$ is defined as a normally distributed random variable with zero mean and a variance denoted by $\sigma_{(\cdot)}^2$:

$$\delta(\cdot) := \mathcal{N}\left(0, \sigma_{(\cdot)}^2\right) \tag{8.27}$$

From the information in Table 8.1, equations (8.21), (8.22), and (8.26) simplify to

$$x_{r_0} = \delta x_{r_0},\ y_{r_0} = \delta y_{r_0},\ \gamma_0 = \delta\gamma_0 \tag{8.28}$$

Computing a transfer trajectory requires defining a final desired safety ellipse. Table 8.2 lists the ROEs of the desired final safety ellipse that are consistent across all test cases.

Table 8.2: ROEs of the final desired safety ellipse for all test cases.

x_{r_f} [m]	y_{r_f} [m]	a_f [m]	E_f [deg]	A_f [m]	γ_f [deg]
0	0	a_0^n	$E_f^n + \Delta E^n$	A_0^n	0

The final safety ellipse is always stationary, centered, and ideally oriented. Also, its final dimensions are equal to the initial nominal dimensions. ΔE^n is the nominal desired change in the in-plane phase angle, and its value varies by test case. The variable E_f^n is defined as

$$E_f^n := E_0^n + \tau_f - \tau_0 \tag{8.29}$$

Substituting E_f from Table 8.2 and equation (8.24) into equation (4.9), the desired change in the in-plane phase angle is

$$\Delta E = \Delta E^n - \delta\Delta E \tag{8.30}$$

Substituting x_{r_0} from equation (8.28) into equation (5.84), the radial component of the instantaneous center immediately before the first maneuver is

$$x_{r_1}^- = \delta x_{r_0} \tag{8.31}$$

Substituting x_{r_0} and y_{r_0} from equation (8.28) into equation (5.86) and applying the information from Table 8.2, the difference between the desired final in-track component of the

instantaneous center and its value immediately before the first maneuver is

$$\Delta y_{r_1}^{-} = \frac{3}{2}(\tau_{\text{wait}})\delta x_{r_0} - \delta y_{r_0} \tag{8.32}$$

Test Cases

Table 8.3 lists the initial nominal in-plane semi-major axis and cross-track amplitude, the ratio of these values, and the nominal desired change in the in-plane phase angle for each test case.

Table 8.3: Nominal in-plane semi-major axis and cross-track amplitude values and the nominal desired change in the in-plane phase angle for each test case.

case #	a_0^n [m]	A_0^n [m]	A_0^n/a_0^n	ΔE^n [deg]
1	1000	500	0.50	45
2	1000	250	0.25	45
3	1000	250	0.25	30
4	100	50	0.50	45
5	100	25	0.25	30
6	1000	500	0.50	15

Table 8.4 lists the variances of the Gaussian distributions in equations (8.21) through (8.26) in terms of 3-σ values for each test case.

Table 8.4: 3-σ ROE dispersions for each test case.

case #	x_{r_0} [m]	y_{r_0} [m]	a_0 [m]	ΔE [deg]	A_0 [m]	γ_0 [deg]
1	50	100	100	15	50	15
2-3	50	100	100	15	25	15
4	5	10	10	15	5	15
5	5	10	10	15	2.5	15
6	50	100	100	5	50	5

The dispersions on x_{r_0}, y_{r_0}, and a_0 are proportional to a_0^n, and the dispersions on A_0 are proportional to A_0^n. In contrast, the dispersions on ΔE and γ_0 are independent of the safety ellipse's dimensions.

Test cases 1 through 5 focus on optimality in terms of the primer vector conditions. For nominal phasing, the primer vector conditions were shown to be a function of only γ_0 and A_0/a_0. Figure 8.2 also showed that there are regions in $(\gamma_0, A_0/a_0)$ space where the analytic solution is suboptimal but requires nearly the same Δv as the numerical solution. The test cases are chosen to show how additional parameters affect optimality. More importantly, they indicate whether the nominal primer vector conditions and trends shown in Figure 8.2 remain a good approximation for off-nominal scenarios that are dispersed about nominal conditions.

Test case 6 focuses on the effect of instantaneous center changes on optimality. For cases 1 through 5, ΔE^n is specified such that the 3-σ bounds on $x_{r_1}^-$ and $\Delta y_{r_1}^-$ are inside the region shown in Figure 8.6. For case 6, the 3-σ bounds on $x_{r_1}^-$ and $\Delta y_{r_1}^-$ exceed this region. Figure 8.7 shows the 3-σ bounds on $x_{r_1}^-$ and $\Delta y_{r_1}^-$ for $\tau_{\text{wait}} = 0$ (solid) and $\tau_{\text{wait}} = \pi$ (dashed) plotted over the approximate allowable $(x_{r_1}^-, \Delta y_{r_1}^-)$ region for test cases 1 (blue) and 6 (red). These regions are computed using a_0^n and ΔE^n. The covariance ellipses are computed from equations (8.31) and (8.32).

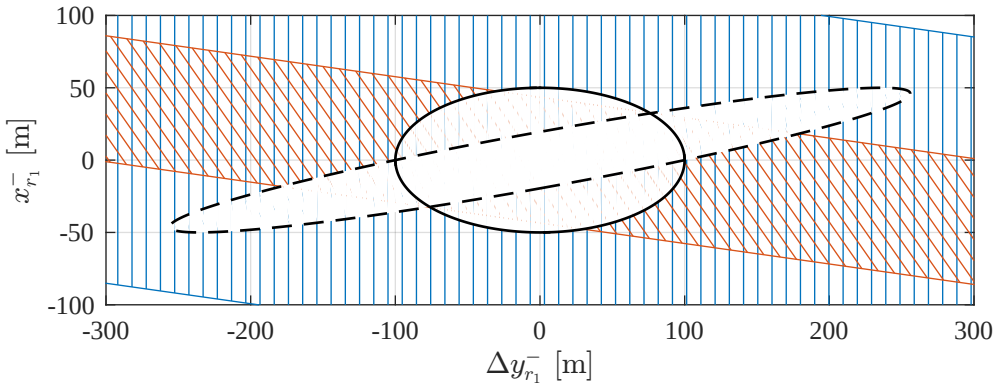

Fig. 8.7: 3-σ bounds on $x_{r_1}^-$ and $\Delta y_{r_1}^-$ for $\tau_{\text{wait}} = 0$ (solid) and $\tau_{\text{wait}} = \pi$ (dashed) plotted over the approximate allowable $(x_{r_1}^-, \Delta y_{r_1}^-)$ region for test cases 1 (blue) and 6 (red).

Figure 8.7 shows that for test case 6, a large initial radial offset is required for a sample to fall outside the $(x_{r_1}^-, \Delta y_{r_1}^-)$ region, and the combination of a large $|x_{r_0}|$ and τ_{wait} increases the likelihood of a suboptimal analytic solution.

Results

Table 8.5 lists the percentage of samples in which the analytic solution is optimal and the minimum ratio of the Δv from the SOCP solution to the Δv from the analytic solution for each test case.

Table 8.5: Percentage of optimal samples and minimum ratio of the numerical Δv to the analytic Δv for each test case.

case #	% of optimal samples	$\min(\Delta v_{\text{num}}/\Delta v_{\text{ana}})$
1	100	1.0000
2	100	1.0000
3	98.4	0.9881
4	100	1.0000
5	97.2	0.9634
6	95.6	0.6920

The suboptimal samples in test cases 3 and 5 are caused by violating the primer vector condition $p \leq 1$. The resulting Δv penalty is small–a maximum of roughly 4% across these test cases. This is consistent with the trends of Figure 8.2. The consistency between cases 1 and 4 and cases 3 and 5 agrees with the scaling property shown in Section 5.1.3. Comparing cases 2 and 3 and cases 4 and 5 shows that the primer vector conditions are affected by parameters other than γ_0 and A_0/a_0, however, their effects are small. The key takeaway from these cases is that the analytic solution requires nearly the same Δv as the numerical solution across all samples.

For test case 6, all but one of the suboptimal samples is caused by too large an instantaneous center correction which results in a nonexistent costate solution. The resulting

Δv penalty can be much larger than in cases that violate the primer vector conditions–a maximum of roughly 30% for this test case.

Figure 8.8 shows each sample of $x_{r_1}^-$ and $\Delta y_{r_1}^-$ plotted over the region approximating their allowable values for case 6. The markers indicate whether the analytic solution is optimal (dot = optimal, x's = suboptimal), and the colors denote the sign of the maneuver direction (black = positive, blue = negative).

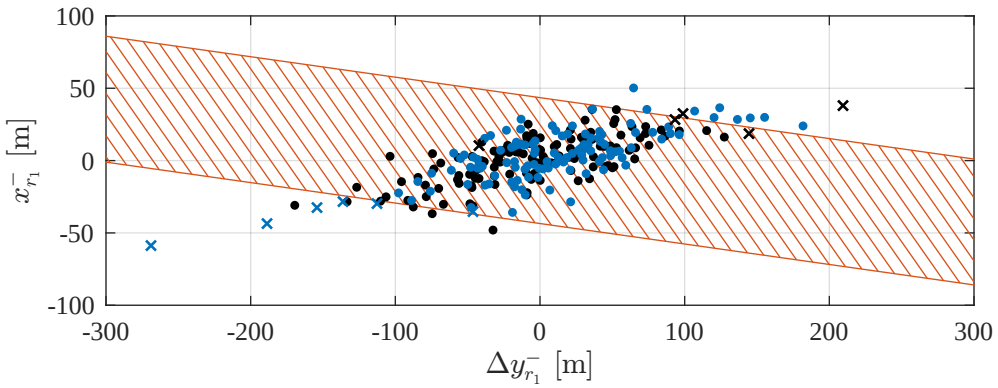

Fig. 8.8: $x_{r_1}^-$ and $\Delta y_{r_1}^-$ samples plotted over the approximate allowable $(x_{r_1}^-, \Delta y_{r_1}^-)$ region for test case 6. The markers denote optimality (dots = optimal, x's = suboptimal), and the colors denote the sign of the maneuver direction (blue = positive, black = negative)

Figure 8.8 shows that the suboptimal samples are generally located near the border or outside the approximate allowable $(x_{r_1}^-, \Delta y_{r_1}^-)$ region. However, not all samples outside this region are suboptimal. One of the reasons for this trend is that, as Figure 8.5 shows, the $(x_{r_1}^-, \Delta y_{r_1}^-)$ region is the intersection of two larger regions that depend on the sign of the maneuver direction. This explains the correlation between the sign of the maneuver direction and whether a sample located outside the $(x_{r_1}^-, \Delta y_{r_1}^-)$ region is optimal.

Table 8.6 lists the minimum radial separation between the in-track axis and point of relative apsides and the maximum relative phase angle for each test case.

Table 8.6: Passive safety parameters for each test case.

case #	$\min(d_k^+/a_0)$	$\max(\lvert\gamma_k^+\rvert)$ [deg]
1	0.29	13.3°
2	0.31	13.6°
3	0.36	11.7°
4	0.33	11.3°
5	0.38	11.9°
6	0.40	4.4°

The results in Table 8.6 shows that the intermediate trajectories across all test cases are passively safe.

8.4 Summary

This chapter focused on safety ellipse phasing, which is a reconfiguration where the dominant component is a change in the chaser's location along the safety ellipse. A simplified version of the problem, referred to as nominal resizing, was first considered. The simplifying assumptions allow for an analytic analysis of optimality and passive safety. One key result from this analysis is an equation that relates optimality to the safety ellipse's initial orientation and initial ratio of the cross-track amplitude to in-plane semi-major axis. This analysis also showed that the nominal transfer trajectories are passively safe as long as the desired phase angle change is not near $\pm 180°$. A version of this problem without simplifying assumptions, referred to as off-nominal phasing, was then considered. Monte Carlo methods were used to analyze optimality and passive safety. The results showed that the analytic solution performs well, either generating an optimal solution or one that requires only slightly more Δv than a numerical solution. The results showed that the analytic solution generated both fuel-optimal and passively safe transfer trajectories for a range of practical off-nominal phasing scenarios.

CHAPTER 9

SAFETY ELLIPSE INGRESS

9.1 Overview

Figure 9.1 shows an example of a nominal safety ellipse ingress where the chaser transfers from a nominal v-bar stationkeep to an offset safety ellipse. The maneuver sequence is indicated by the numbers above each maneuver location. Before maneuver 1, the chaser sits on the in-track axis, typically at a large distance from the origin (this type of holding strategy commonly referred to as a v-bar stationkeep [1, 22]). Maneuver 1 initiates the transfer trajectory. Maneuver 2 alters the transfer trajectory to make it intersect the final safety ellipse at the time of maneuver 3. Maneuver 3 establishes the final safety ellipse. The chaser remains on the final safety ellipse, traveling clockwise, until another maneuver is performed.

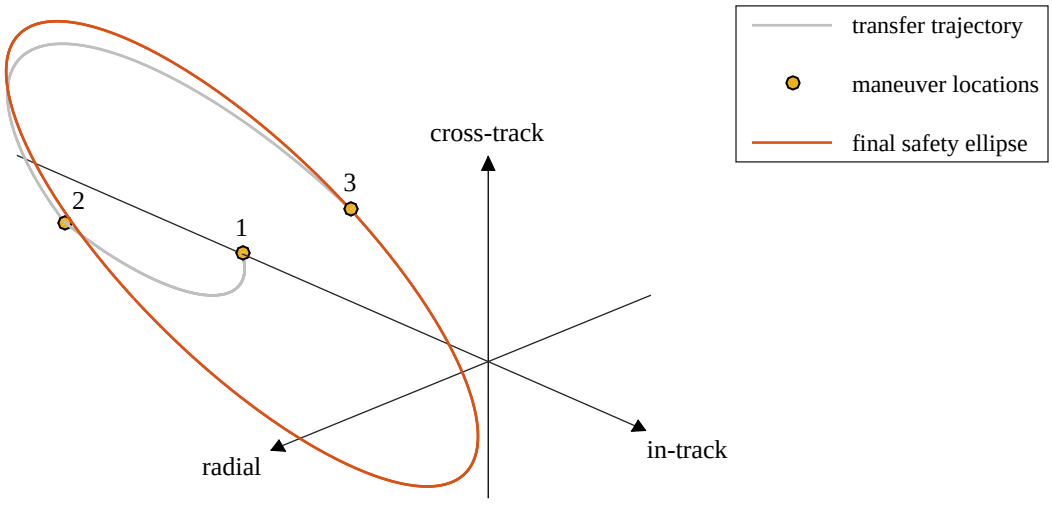

Fig. 9.1: An example of nominal safety ellipse ingress: nominal v-bar stationkeep to offset safety ellipse.

This chapter focuses specifically on establishing an offset safety ellipse from a v-bar stationkeep, and this scenario will be referred to as ingress unless otherwise specified. The problem is analyzed by dividing it into two categories: nominal and off-nominal.

The nominal ingress scenario involves simplifying assumptions that lead to an idealized version of the problem. Although these assumptions remove realism, they also simplify the expressions for the Δv vectors and maneuver times to where analysis of optimality and passive safety can be performed analytically. One key result from this analysis is an equation that relates optimality to the safety ellipse's final orientation and final ratio of the cross-track amplitude to in-plane semi-major axis. It says that the analytic solution is optimal for any final ratio when the final orientation is ideal. This equation is presented in Section 9.2.1 and numerically validated in Section 9.2.2. Section 9.2.3 shows that a maneuver sequence with passively safe intermediate trajectories is achieved by considering the initial in-track location and the orientation of the final desired safety ellipse.

The off-nominal ingress scenario makes no simplifying assumptions. It is a general reconfiguration where the safety ellipse's initial dimensions are much smaller than its final dimensions. Section 9.3.1 shows that a passively safe maneuver sequences requires waiting up to one orbit period before initiating the first maneuver. Section 9.3.2 presents equations which approximate the allowable changes to the instantaneous center that do not affect optimality of the analytic solution. Section 9.3.3 analyzes the optimality and passive safety of off-nominal scenarios using Monte Carlo methods.

9.2 Nominal

Nominal ingress is a simplified case of a general reconfiguration. It has the following characteristics:

1) The instantaneous center after the transfer trajectory is equal to the instantaneous center if no maneuvers had occurred ($\Delta x_r = 0$ and $\Delta y_r = 0$). Additionally, for an initial nominal v-bar stationkeep, $x_{r_0} = 0$.

2) The initial in-plane semi-major axis and cross-track amplitude are zero.

9.2.1 Maneuver Sequence and Primer Vector Analysis

Substituting $\Delta x_r = \Delta y_r = a_0 = A_0 = 0$ into equations (5.62) through (5.64) and equations (5.74) and (5.76), the Δv vectors are

$$\Delta \boldsymbol{v}_1 = \eta \frac{\Omega}{16} \begin{bmatrix} 2a_f \sin\gamma_f & a_f \cos\gamma_f & 4A_f \end{bmatrix}^T, \; \Delta \boldsymbol{v}_2 = -2\Delta \boldsymbol{v}_1, \; \Delta \boldsymbol{v}_3 = \Delta \boldsymbol{v}_1 \tag{9.1}$$

Since the chaser is initially stationary, the first maneuver can occur at any time. Also, E and ψ are undefined until the first maneuver occurs. Substituting the components of $\Delta \boldsymbol{v}_1$ into equations (3.14) and (3.16), E and ψ immediately after the first maneuver are

$$E_1^+ = \begin{cases} \gamma_f & \eta = 1 \\ \gamma_f \pm \pi & \eta = -1, \end{cases} \qquad \psi_1^+ = \begin{cases} 0 & \eta = 1 \\ \pi & \eta = -1 \end{cases} \tag{9.2}$$

Substituting equation (9.1) into equations (5.2) and (5.4), E and ψ immediately after the third maneuver are

$$E_3^+ = E_1^+, \quad \psi_3^+ = \psi_1^+ \tag{9.3}$$

Equations (9.3) and (9.2) show that η affects the chaser's location along the safety ellipse once it has been established, and these two possible locations mirror each other.

Substituting equation (9.1) into equation (5.109), the primer vector conditions are satisfied when

$$\cos^2\gamma_f \geq 1 - \frac{4}{3}\frac{A_f}{a_f} \tag{9.4}$$

Equation (9.4) says that optimality depends on the safety ellipse's final orientation and final ratio of the cross-track amplitude to in-plane semi-major axis. The primer vector conditions are satisfied for all orientations when

$$\frac{A_f}{a_f} \geq \frac{\sqrt{3}}{2} \tag{9.5}$$

More importantly, these conditions are satisfied for all A_f/a_f when $\gamma_f = \gamma_f^{\text{ideal}} = 0°, \pm 180°$.

9.2.2 Numerical Validation

The primer vector analysis is validated numerically. A family of nominal ingress cases, distinguished by different values of γ_f and A_f/a_f, are solved both numerically and analytically. The problem is solved numerically using the SOCP in equation (4.46) with a fixed final time of multiple orbit periods to emulate the free-time problem. Figure 9.2 shows a contour plot with level sets that represent the ratio of the Δv from the SOCP solution to the Δv from the analytic solution as a function of γ_f and A_f/a_f. This plot is identical when γ_f is shifted by $\pm 180°$.

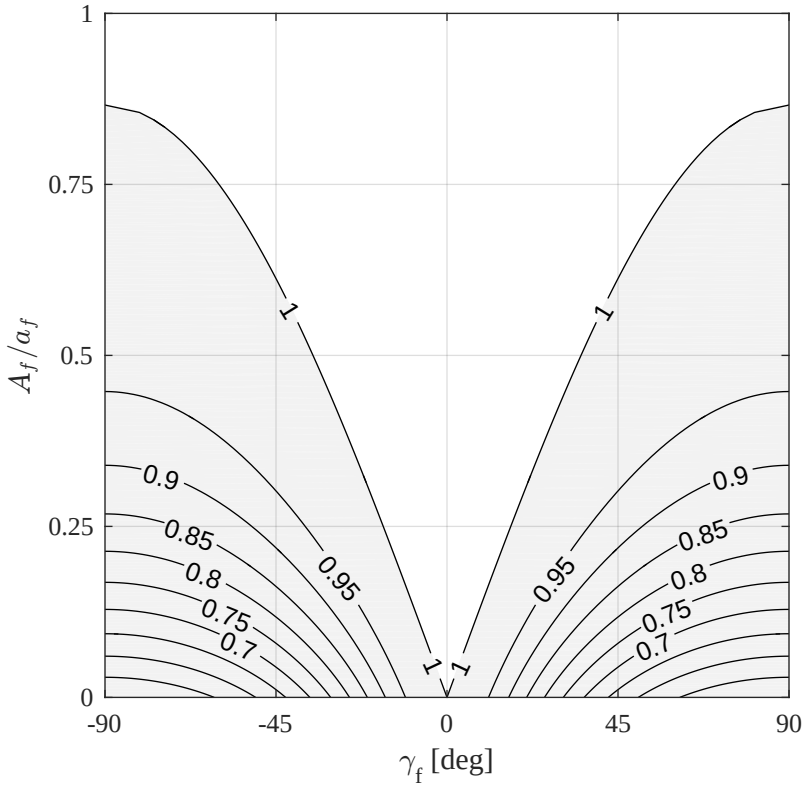

Fig. 9.2: Contours representing the ratio of the SOCP-optimal Δv to the analytic Δv as a function of γ_f and A_f/a_f.

The contour line showing a 1:1 Δv ratio matches the solution to the equation

$$\cos^2 \gamma_0 = 1 - \frac{4}{3}\frac{A_f^2}{a_f^2} \tag{9.6}$$

which describes the boundary of equation (9.4). The white region outside this contour line shows the family of transfers, represented by $(\gamma_f, A_f/a_f)$ pairs, where the analytic solution is optimal. The grey region inside this contour line shows the family of transfers where the analytic solution is suboptimal. The peak of this contour line occurs at $A_f/a_f = \sqrt{3}/2$, which matches equation (9.5). The contours confirm that the analytic solution is optimal for all A_f/a_f when $\gamma_f = \gamma_f^{\text{ideal}}$.

Figure 9.2 shows that as γ_f increases, a larger A_f/a_f is required for the analytic solution to remain optimal. Section 7.2.2 discusses the cause of this behavior.

9.2.3 Passive Safety Analysis

This section analyzes the passive safety of transfer trajectories that result from an incomplete maneuver sequence. The cases under consideration are: 1) a transfer where only the first maneuver is performed and 2) a transfer where only the first and second maneuvers are performed. These trajectories are referred to as intermediate trajectories. The ROEs of the intermediate trajectories are computed by substituting equation (9.1) into equations (3.11) through (3.16).

The intermediate relative phase angles are

$$\gamma_k^+ = \gamma_f,\ k = 1, 2 \tag{9.7}$$

Equation (9.7) says that the orientation of the final safety ellipse establishes the orientations of the intermediate trajectories. The intermediate in-plane semi-major axes, cross-track amplitudes, and radial components of the instantaneous center are

$$a_1^+ = \frac{1}{4}a_f \tag{9.8}$$

$$a_2^+ = \frac{3}{4}a_f \tag{9.9}$$

$$A_1^+ = \frac{1}{4}A_f \tag{9.10}$$

$$A_2^+ = \frac{3}{4}A_f \tag{9.11}$$

$$x_{r_1}^+ = \eta\frac{1}{8}a_f\cos\gamma_f \tag{9.12}$$

$$x_{r_2}^+ = -\eta\frac{1}{8}a_f\cos\gamma_f \tag{9.13}$$

From equation (A.1), the intermediate radial separations between the in-track axis and point of relative apsides are

$$d_1^+ = 0 \tag{9.14}$$

$$d_2^+ = \frac{1}{4}a_f|\cos\gamma_f| \tag{9.15}$$

Equation (9.14) says that there are locations along the first intermediate trajectory where the chaser intersects the in-track axis (see Appendix A for more details). This makes the first intermediate trajectory potentially unsafe. However, depending on η, it is possible for the sign of $x_{r_1}^+$ to oppose the sign of the initial in-track offset. This results in the first intermediate trajectory safely drifting away from the target. The second intermediate trajectory then brings the chaser back safely towards the target assuming γ_f is near γ_f^{ideal}.

The desired value of η that maintains passive safety, denoted η^{des}, depends on the sign of the initial in-track offset and the final desired orientation:

$$\eta^{\text{des}} = \begin{cases} -1 & \text{sgn}(y_{r_0}) > 0,\ -\frac{\pi}{2} < \gamma_f < \frac{\pi}{2} \\ -1 & \text{sgn}(y_{r_0}) < 0,\quad \gamma_f < -\frac{\pi}{2} \text{ OR } \gamma_f > \frac{\pi}{2} \\ 1 & \text{sgn}(y_{r_0}) < 0,\ -\frac{\pi}{2} < \gamma_f < \frac{\pi}{2} \\ 1 & \text{sgn}(y_{r_0}) > 0,\quad \gamma_f < -\frac{\pi}{2} \text{ OR } \gamma_f > \frac{\pi}{2} \end{cases} \tag{9.16}$$

Equations (9.2) and (9.3) show that η affects the chaser's location along the safety ellipse once it has been established. This means that for a passively safe maneuver sequence,

the sign of the initial in-track offset and the final desired orientation dictate the chaser's in-plane phase angle immediately after the third maneuver.

9.3 Off-Nominal

Figure 9.3 shows an example of an off-nominal safety ellipse ingress where the chaser transfers from an off-nominal v-bar stationkeep to an offset safety ellipse. The off-nominal stationkeep is a trajectory with a large in-track offset relative to its drift rate, in-plane semi-major axis, and cross-track amplitude–in effect, a small drifting ellipse. The chaser travels along this drifting ellipse before the first maneuver. The sequence of maneuvers to establish the final safety ellipse is described in Section 9.1.

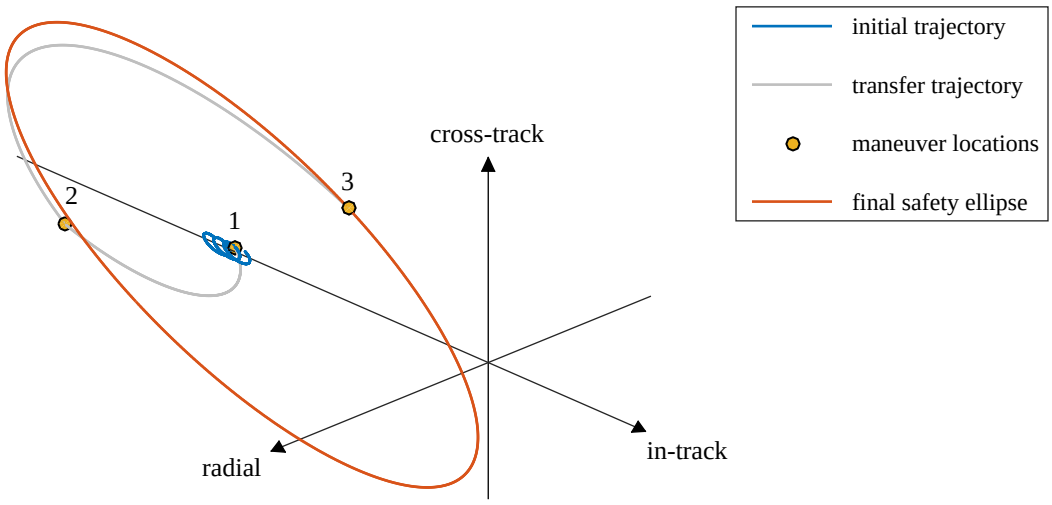

Fig. 9.3: An example of off-nominal safety ellipse ingress: off-nominal v-bar stationkeep to offset safety ellipse.

The off-nominal ingress scenario ignores the simplifying assumptions made in Section 9.2. The maneuver sequence establishes a safety ellipse with dimensions that are much larger than its initial dimensions.

9.3.1 Wait Time and Passive Safety

The following approach assumes that the analysis of Section 9.2.3 is an adequate approximation for off-nominal scenarios. For a nominal ingress scenario, η can be selected from equation (9.16) to meet passive safety requirements. For an off-nominal ingress scenario, η is dependent on properties of the initial relative motion trajectory and the final safety ellipse. From Section 5.1.3, η is a function of desired changes to the cross-track parameters and the initial cross-track phase angle. However, without affecting the final desired safety ellipse, the sign of η can be changed implicitly by increasing the wait time until the first maneuver. Upon initially computing η, if η and η^{des} are unequal, changing the sign of η is achieved using the following logic:

$$\tau_{\text{wait}} = \begin{cases} \tau_{\text{wait}} & \eta = \eta^{\text{des}} \\ \tau_{\text{wait}} + \pi & \eta \neq \eta^{\text{des}} \end{cases} \tag{9.17}$$

Incrementing τ_{wait} by π effectively increments ψ_1^- by π, which flips the sign of η. Equation (9.17) extends the possible wait time until the first maneuver by an additional half-orbit period. Therefore, an opportunity for a passively safe ingress occurs every orbit period.

9.3.2 Instantaneous Center and Optimality

Section 5.1.5 derived bounds on the allowable changes to the instantaneous center that do not affect optimality for a general reconfiguration. This section approximates these bounds specifically for ingress. Approximations are made to reduce the bounds to functions of $x_{r_1}^-$, $y_{r_1}^-$, η, γ_f, and a_f. Due to the decoupling of in-plane and out-of-plane motion, instantaneous center changes are independent of cross-track maneuvers.

This analysis assumes that the maneuver sequence removes the drift rate at the final time ($x_{r_f} = 0$). It also assumes $a_0 = A_0 = 0$ and $\gamma_f = \gamma_f^{\text{ideal}}$. These assumptions lead to

$$\Delta\tilde{v}_x = 0,\ \Delta\tilde{v}_y = \pm\frac{1}{4}\eta\Omega a_f \tag{9.18}$$

The sign ambiguity in equation (9.18) is due to whether $\gamma_f = 0°$ or $\pm 180°$. Substituting equation (9.18) into equations (5.90) through (5.92), a costate solution exists when

$$\pm\frac{\eta}{a_f}\left(6x_{r_1}^- + \frac{8}{3\pi}\Delta y_{r_1}^-\right) \leq 1 \tag{9.19}$$

$$\pm\frac{\eta}{a_f}2x_{r_1}^- \geq -1 \tag{9.20}$$

$$\pm\frac{\eta}{a_f}\left(2x_{r_1}^- + \frac{8}{3\pi}\Delta y_{r_1}^-\right) \geq -1 \tag{9.21}$$

$x_{r_1}^-$ is the radial component of the instantaneous center immediately before the first maneuver. $\Delta y_{r_1}^-$ is the difference between the desired final in-track component of the instantaneous center and its value immediately before the first maneuver.

Equations (9.19) through (9.21) define polyhedrons in $(x_{r_1}^-, \Delta y_{r_1}^-)$ space that are functions of η, γ_f^{ideal}, and a_f. Figure 9.4 plots these polyhedrons. They represent, for particular values of η and γ_f^{ideal}, an approximate region of allowable instantaneous center changes immediately before the first maneuver that do not affect optimality of the analytic solution.

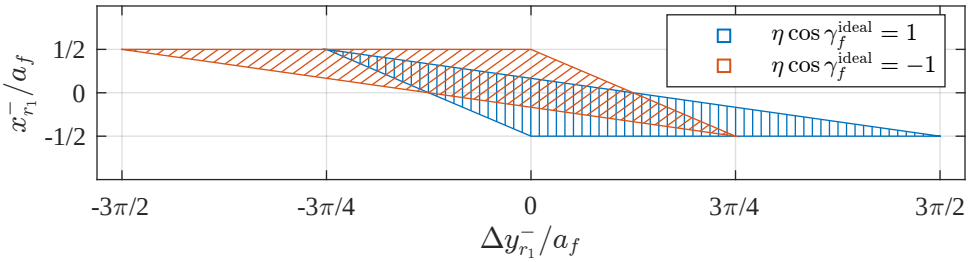

Fig. 9.4: Region approximating allowable $(x_{r_1}^-, \Delta y_{r_1}^-)$ pairs that do not affect optimality for particular values of η and γ_f^{ideal}.

The intersections of these sets was plotted for both resizing and phasing. For ingress, however, a passively safe maneuver sequence requires a specific η, which makes the intersection of these sets less relevant. Figure 9.4 shows that the allowable instantaneous center changes are proportional to a_f.

9.3.3 Monte Carlo Analysis

Off-nominal ingress is a general reconfiguration that establishes an offset safety ellipse. The maneuver sequence is computed using the equations in Sections 5.1.2 through 5.1.4. Compared to nominal ingress, these equations are much more difficult to analyze analytically. Instead, Monte Carlo methods are used to analyze optimality and passive safety. Four test cases are conducted with each test case consisting of 250 samples.

Each individual Monte Carlo sample is a particular off-nominal ingress scenario, and the transfer trajectory is computed both numerically and analytically. The problem is solved numerically using the SOCP in equation (4.52) with a fixed final time of multiple orbit periods to emulate the free-time problem.

General Setup

The Monte Carlo simulation relies on first defining an initial nominal v-bar stationkeep. Table 9.1 lists the ROEs of the initial nominal v-bar stationkeep that are consistent across all test cases.

Table 9.1: ROEs of the initial nominal v-bar stationkeep for all test cases.

$x_{r_0}^n$ [m]	$y_{r_0}^n$ [m]	a_0^n [m]	A_0^n [m]
0	-5000	0	0

The superscript 'n' denotes a nominal value. The ROEs of the initial off-nominal v-bar stationkeep are computed by adding dispersions to the nominal. Since a_0 and A_0 become nonzero, the initial phase angles must also be defined. The ROEs of the initial off-nominal v-bar stationkeep are

$$x_{r_0} = x_{r_0}^n + \delta x_{r_0} \tag{9.22}$$

$$y_{r_0} = y_{r_0}^n + \delta y_{r_0} \tag{9.23}$$

$$a_0 = a_0^n + \mathcal{U}\left(0, a_0^{\max}\right) \tag{9.24}$$

$$E_0 = \mathcal{U}\left(-180^\circ, 180^\circ\right) \tag{9.25}$$

$$A_0 = A_0^n + \mathcal{U}\left(0, A_0^{\max}\right) \tag{9.26}$$

$$\psi_0 = \mathcal{U}\left(-180^\circ, 180^\circ\right) \tag{9.27}$$

where the variable $\delta(\cdot)$ is defined as a normally distributed random variable with zero mean and a variance denoted by $\sigma^2_{(\cdot)}$:

$$\delta(\cdot) := \mathcal{N}\left(0, \sigma^2_{(\cdot)}\right) \tag{9.28}$$

and $\mathcal{U}$ denotes a uniform distribution. $a_0^{\max}$ and $A_0^{\max}$ are the maximum initial in-plane semi-major axis and cross-track amplitude. From equations (9.25) and (9.27), $\gamma_0 = \mathcal{U}\left(-180^\circ, 180^\circ\right)$. Using the information in Table 9.1, equations (9.22), (9.24), and (9.26) simplify to

$$x_{r_0} = \delta x_{r_0},\ a_0 = \mathcal{U}\left(0, a_0^{\max}\right),\ A_0 = \mathcal{U}\left(0, A_0^{\max}\right) \tag{9.29}$$

Computing a transfer trajectory requires defining a final desired safety ellipse. Table 9.2 lists the ROEs of the final desired safety ellipse that are consistent across all test cases.

Table 9.2: ROEs of the final desired safety ellipse for all test cases.

x_{r_f} [m]	y_{r_f} [m]	E_f [deg]	γ_f [deg]
0	$y_{r_0}^n$	$\mathcal{U}(-180, 180)$	0

The final safety ellipse is always stationary and ideally oriented, and its final in-track offset is equal to the initial nominal in-track offset. The final desired in-plane phase angle can also be written as

$$E_f = E_0^{\text{des}} + \tau_f - \tau_0 \tag{9.30}$$

where E_0^{des} is the desired in-plane phase angle at the initial time, which may represent, for example, desired lighting conditions that are known at the initial time. From Table 9.2 and

equation (9.30), $E_0^{\text{des}} = \mathcal{U}(-180°, 180°)$. Substituting equation (9.30) into equation (4.9) leads to

$$\Delta E = E_0^{\text{des}} - E_0 = \mathcal{U}(-180°, 180°) \tag{9.31}$$

Substituting x_{r_0} from equation (9.29) into equation (5.84), the radial component of the instantaneous center immediately before the first maneuver is

$$x_{r_1}^- = \delta x_{r_0} \tag{9.32}$$

Substituting x_{r_0} from equation (9.29) and equation (9.23) into equation (5.86) and applying the information from Table 9.2, the difference between the desired final in-track component of the instantaneous center and its value immediately before the first maneuver is

$$\Delta y_{r_1}^- = \frac{3}{2}(\tau_{\text{wait}})\delta x_{r_0} - \delta y_{r_0} \tag{9.33}$$

Test Cases

Table 9.3 lists the final desired and maximum initial in-plane semi-major axis and cross-track amplitude for each test case.

Table 9.3: Ingress test case parameters.

case #	a_f [m]	A_f [m]	$a_0^{\max}$ [m]	$A_0^{\max}$ [m]
1	1000	500	100	100
2	750	375	100	100
3	750	250	100	100
4	250	125	12.5	6.25

Table 9.4 lists the 3-σ dispersions on the instantaneous center. These are consistent across all test cases.

Table 9.4: Instantaneous center 3-σ dispersions for all test cases.

x_{r_0} [m]	y_{r_0} [m]
50	100

Test cases 1 through 3 focus on optimality in terms of the primer vector conditions. For nominal ingress, the primer vector conditions were shown to be a function of only γ_f and A_f/a_f. Figure 9.2 also showed that there are regions in $(\gamma_f, A_f/a_f)$ space where the analytic solution is suboptimal but requires nearly the same Δv as the numerical solution. The test cases are chosen to show how additional parameters affect optimality. More importantly, they indicate whether the nominal primer vector conditions and trends shown in Figure 9.2 remain a good approximation for off-nominal scenarios that are dispersed about nominal conditions.

Test case 4 focuses on the effect of instantaneous center changes on optimality. For cases 1 through 3, a_f is specified such that the 3-σ bounds on $x_{r_1}^-$ and $\Delta y_{r_1}^-$ are inside the region shown in Figure 9.4. For case 4, the 3-σ bounds exceed this region. Figure 9.5 shows the 3-σ bounds on $x_{r_1}^-$ and $\Delta y_{r_1}^-$ for $\tau_{\text{wait}} = 0$ (solid) and $\tau_{\text{wait}} = 2\pi$ (dashed) over the approximate allowable $(x_{r_1}^-, \Delta y_{r_1}^-)$ region for test cases 3 (blue) and 4 (red). The covariance ellipses are computed from equations (9.32) and (9.33). The maximum value of τ_{wait} is based upon the analysis of Section 9.3.1.

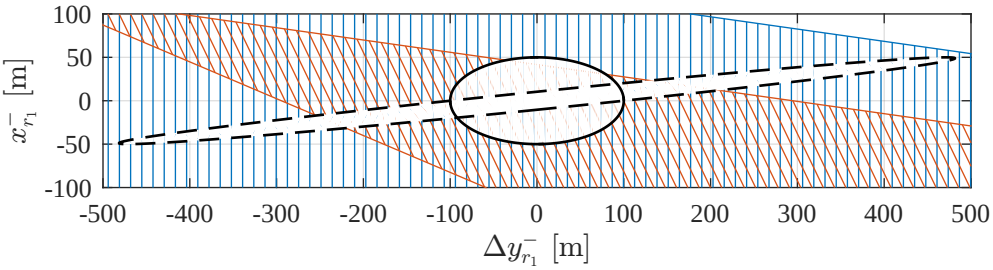

Fig. 9.5: 3-σ bounds on $x_{r_1}^-$ and $\Delta y_{r_1}^-$ for $\tau_{\text{wait}} = 0$ (solid) and $\tau_{\text{wait}} = 2\pi$ (dashed) plotted over the approximate allowable $(x_{r_1}^-, \Delta y_{r_1}^-)$ region for test cases 3 (blue) and 4 (red).

The $(x_{r_1}^-, \Delta y_{r_1}^-)$ regions are plotted for $\eta = 1$. From equation (9.16), this is the desired maneuver direction sign based upon the initial in-track offset and final desired orientation. Figure 9.5 shows that for test case 4, a large initial radial offset is required for a sample to fall outside the $(x_{r_1}^-, \Delta y_{r_1}^-)$ region, and a combination of a large $|x_{r_0}|$ and τ_{wait} increases the likelihood of a suboptimal analytic solution.

Results

Table 9.5 lists the percentage of Monte Carlo samples in which the analytic solution is optimal and the minimum ratio of the Δv from the SOCP solution to the Δv from the analytic solution for each test case.

Table 9.5: Percentage of optimal samples and minimum ratio of the numerical Δv to the analytic Δv for each test case.

case #	% of optimal samples	$\min(\Delta v_{\text{num}}/\Delta v_{\text{ana}})$
1	100	1.0000
2	100	1.0000
3	97.6	0.9969
4	92.0	0.6988

For test case 3, every suboptimal sample is caused by violating the primer vector condition $p \leq 1$. This shows that the primer vector conditions are affected by parameters other than γ_f and A_f/a_f. However, the resulting Δv penalty is less than 1%, which is consistent with the trends in Figure 9.2.

For test case 4, every suboptimal sample is caused by too large an instantaneous center change which results in a nonexistent costate solution. The maximum Δv penalty across all samples is roughly 30%. Figure 9.6 shows each sample of $x_{r_1}^-$ and $\Delta y_{r_1}^-$ plotted over the region approximating their allowable values for test case 4. The colors indicate whether the analytic solution is optimal (blue = optimal, black = suboptimal).

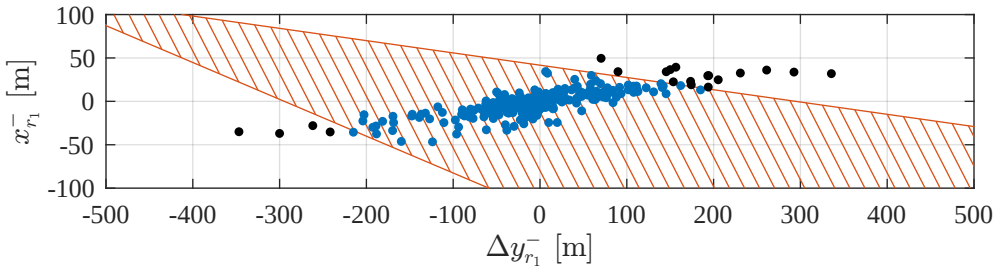

Fig. 9.6: $x_{r_1}^-$ and $\Delta y_{r_1}^-$ samples plotted over the approximate allowable $(x_{r_1}^-, \Delta y_{r_1}^-)$ region for test case 4. The colors denote optimality (blue = optimal, black = suboptimal).

Figure 9.6 shows that the suboptimal samples are outside the approximate allowable $(x_{r_1}^-, \Delta y_{r_1}^-)$ region. These are samples that have both a large initial radial offset and a long wait time until the first maneuver.

Since $\text{sgn}(y_{r_0}) < 0$ across all test cases, $x_{r_1}^+$ must be positive for a passively safe maneuver sequence. This value, along with d_2^+/a_f and γ_2^+, are parameters that indicate the passive safety of the intermediate trajectories. Table 9.6 lists these passive safety parameters for each test case.

Table 9.6: Passive safety parameters for each test case.

case #	$\min(x_{r_1}^+)$ [m]	$\min(\lvert d_2^+\rvert/a_f)$	$\max(\lvert\gamma_2^+\rvert)$ [deg]
1	98.68	0.15	5.38
2	62.89	0.12	6.72
3	66.16	0.11	9.32
4	4.42	0.01	5.79

The results from test case 4 indicate that too large an instantaneous center change results in a potentially unsafe transfer trajectory. This is caused by the maneuver scale factors deviating far from their nominal 1:2:1 ratio. Test cases 1 through 3 show that when the instantaneous center change is within its allowable $(x_{r_1}^-, \Delta y_{r_1}^-)$ region, the intermediate trajectories remain passively safe.

9.4 Summary

This chapter focused on safety ellipse ingress, which was defined as a maneuver sequence that establishes an offset safety ellipse from an initial v-bar stationkeep. A simplified version of the problem, referred to as nominal ingress, was first considered. The simplifying assumptions allow for analytic analysis of optimality and passive safety. One key result from this analysis is an equation that says that the analytic solution is optimal when the orientation of the final safety ellipse is ideal. This analysis also showed that a maneuver sequence with passively safe intermediate trajectories is achieved by considering the initial in-track location and the final orientation. A version of the problem without simplifying assumptions, referred to as off-nominal ingress, was then considered. Monte Carlo methods were used to analyze optimality and passive safety. Results showed that the analytic solution performs well when changes to the instantaneous center are not too large–either generating an optimal solution or one that requires only slightly more Δv than a numerical solution. The results also showed that the off-nominal intermediate trajectories are passively safe when the changes to the instantaneous are within their allowable bounds.

CHAPTER 10
SAFETY ELLIPSE EGRESS

10.1 Overview

Figure 10.1 shows an example of safety ellipse egress where the chaser transfers from an offset safety ellipse to a v-bar stationkeep. The maneuver sequence is indicated by the numbers above each maneuver location. Before maneuver 1, the chaser travels clockwise along an initial safety ellipse, which may be off-nominal. Maneuver 1 initiates the transfer trajectory. Maneuver 2 alters the transfer trajectory to make it intersect the in-track axis at the time of maneuver 3. Maneuver 3 establishes the final v-bar stationkeep. The chaser sits on the in-track axis until another maneuver is performed.

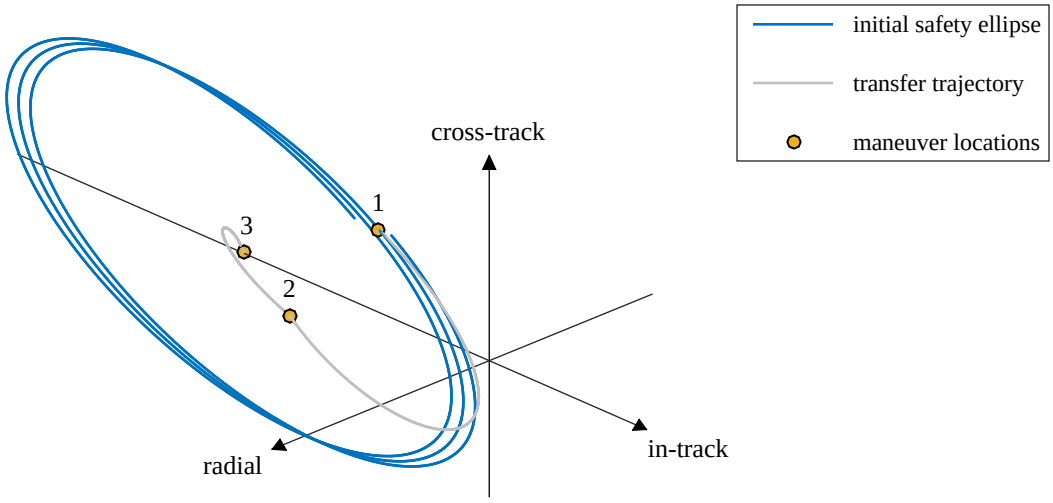

Fig. 10.1: An example of safety ellipse egress: offset safety ellipse to v-bar stationkeep.

In this chapter, safety ellipse egress refers to a maneuver sequence that transfers a safety ellipse to another relative motion trajectory with zero in-plane semi-major axis and

cross-track amplitude. Two egress scenarios are analyzed: an offset safety ellipse to v-bar stationkeep and a safety ellipse to co-elliptic flyby. Although these scenarios have different final trajectories, the equations for computing the maneuver direction are the same and directly follow from Section 5.1.3.

This chapter begins by analyzing the maneuver sequence and primer vector. Unlike resizing, phasing, and ingress, no simplifying assumptions are made. The primer vector analysis results in an equation that relates optimality to the safety ellipse's initial orientation and ratio of the initial cross-track amplitude to in-plane semi-major axis. This equation is presented in Section 10.2 and numerically validated in Section 10.3.

Next, the scenario involving an offset safety ellipse to v-bar stationkeep is analyzed. Section 10.4.1 shows that a maneuver sequence with passively safe intermediate trajectories requires waiting up to one orbit period before initiating the first maneuver. Section 10.4.2 presents equations which approximate the allowable changes to the instantaneous center that do not affect optimality of the analytic solution. Section 10.4.3 analyzes optimality and passive safety using Monte Carlo methods.

Section 10.5 presents an egress scenario involving a safety ellipse to co-elliptic flyby that requires only one maneuver. It is shown that the radial and in-track coordinates of the flyby immediately after the maneuver are dictated by properties of the initial safety ellipse.

10.2 Maneuver Sequence and Primer Vector

Substituting $A_f = a_f = 0$ into equations (5.62) through (5.64), $\Delta\tilde{\boldsymbol{v}}$ is

$$\Delta\tilde{\boldsymbol{v}} = \eta\frac{\Omega}{4}\begin{bmatrix}2a_0\sin\gamma_0 & a_0\cos\gamma_0 & 4A_0\end{bmatrix}^T \tag{10.1}$$

The maneuver direction is

$$\Delta\hat{\boldsymbol{v}} = \eta\frac{1}{\|\Delta\tilde{\boldsymbol{v}}\|}\frac{\Omega}{4}\begin{bmatrix}2a_0\sin\gamma_0 & a_0\cos\gamma_0 & 4A_0\end{bmatrix}^T \tag{10.2}$$

Substituting $A_f = 0$ into equation (5.27), the cross-track phase angle immediately before the first maneuver is

$$\psi_1^- = N\pi,\ N \in \mathbb{Z} \tag{10.3}$$

Equation (10.3) says that the first maneuver occurs when the chaser crosses the target's orbital plane.

Substituting equation (10.2) into equation (5.109), the primer vector conditions are satisfied when

$$\cos^2 \gamma_0 \geq 1 - \frac{4}{3}\frac{A_0}{a_0} \tag{10.4}$$

Equation (10.4) says that optimality depends on the safety ellipse's initial orientation and initial ratio of the cross-track amplitude to in-plane semi-major axis. The primer vector conditions are satisfied for all orientations when

$$\frac{A_0}{a_0} \geq \frac{\sqrt{3}}{2} \tag{10.5}$$

Unlike resizing, phasing, and ingress, the primer vector analysis does not rely on simplifying assumptions. Therefore equations (10.4) and (10.5) are valid for any off-nominal safety ellipse, assuming that a costate exists.

10.3 Numerical Validation

The primer vector analysis is numerically validated. A family of egress cases, distinguished by different values of γ_0 and A_0/a_0, are solved both numerically and analytically. The problem is solved numerically using the SOCP in equation (4.52) with a fixed final time of multiple orbit periods to emulate the free-time problem. Figure 10.2 shows a contour plot with level sets that represent the ratio of the Δv from the SOCP solution to the Δv from the analytic solution as a function of γ_0 and A_0/a_0. This plot is identical when γ_0 is shifted by $\pm 180°$.

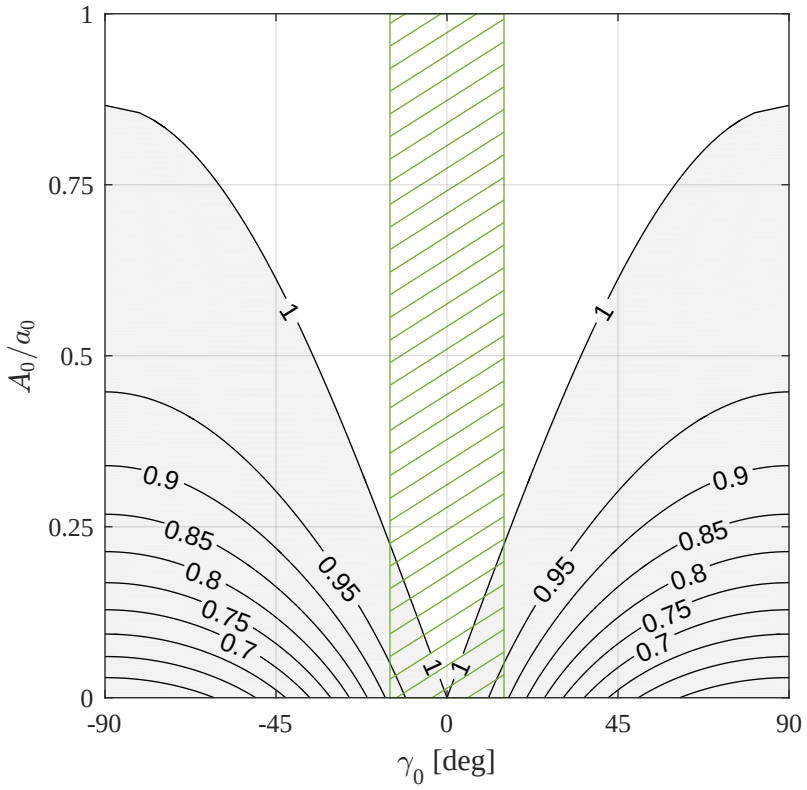

Fig. 10.2: Contours representing the ratio of the SOCP-optimal Δv to the analytic Δv as a function of γ_0 and A_0/a_0.

The contour line showing a 1:1 Δv ratio matches the solution to the equation

$$\cos {\gamma_0}^2 = 1 - \frac{4}{3}\frac{A_0^2}{a_0^2} \tag{10.6}$$

which describes the boundary of equation 10.4. The white region outside this contour line shows the family of transfers, represented by $(\gamma_0, A_0/a_0)$ pairs, where the analytic solution is optimal. The grey region inside this contour line shows the family of transfers where the analytic solution is suboptimal. The peak of this contour line occurs at $A_0/a_0 = \sqrt{3}/2$, which matches equation (10.5). For an ideal orientation ($\gamma_0^{\text{ideal}} = 0°, \pm 180°$), the analytic solution is optimal for any A_0/a_0. The green hatched region shows what may be considered a desired operating range for the safety ellipse's orientation ($\gamma_0^{\text{ideal}} - 15° \leq \gamma_0 \leq \gamma_0^{\text{ideal}} + 15°$).

Figure 10.2 shows that as γ_0 increases, a larger A_0/a_0 is required for the analytic solution to remain optimal. Section 7.2.2 discusses the cause of this behavior.

10.4 Offset Safety Ellipse to V-bar Stationkeep

This section analyzes the egress scenario involving an offset safety ellipse to v-bar stationkeep. An illustration of this scenario is shown in Figure 10.1.

10.4.1 Passive Safety Analysis

This section analyzes the passive safety of transfer trajectories that result from an incomplete maneuver sequence. The cases under consideration are: 1) a transfer where only the first maneuver is performed and 2) a transfer where only the first and second maneuvers are performed. These trajectories are referred to as intermediate trajectories. The ROEs of the intermediate trajectories are computed by substituting equations (10.1) and (10.3) into equations (3.11) through (3.16). This analysis assumes that the initial safety ellipse is stationary ($x_{r_0} = 0$). It also assumes that the desired changes to y_r are relatively small, which means that the maneuver magnitude ratios are approximately 1:2:1.

The intermediate relative phase angles are

$$\gamma_k^+ = \gamma_0,\ k = 1, 2 \tag{10.7}$$

Equation (10.7) says that the orientation of the initial safety ellipse establishes the orientations of the intermediate trajectories. The intermediate in-plane semi-major axes, cross-track amplitudes, and radial components of the instantaneous center are

$$a_1^+ = \frac{3}{4}a_0 \tag{10.8}$$

$$a_2^+ = \frac{1}{4}a_0 \tag{10.9}$$

$$A_1^+ = \frac{3}{4}A_0 \tag{10.10}$$

$$A_2^+ = \frac{1}{4}A_0 \tag{10.11}$$

$$x_{r_1}^{+} = \eta \frac{1}{8} a_0 \cos\gamma_0 \tag{10.12}$$

$$x_{r_2}^{+} = -\eta \frac{1}{8} a_0 \cos\gamma_0 \tag{10.13}$$

From equation (A.1), the intermediate radial separations between the in-track axis and point of relative apsides are

$$d_1^{+} = \frac{1}{4} a_0 |\cos\gamma_0| \tag{10.14}$$

$$d_2^{+} = 0 \tag{10.15}$$

Equation (10.15) says that there are locations along the second intermediate trajectory where the chaser intersects the in-track axis (see Appendix A for more details). This makes the second intermediate trajectory potentially unsafe. However, depending on η, it is possible for the sign of $x_{r_2}^{+}$ to oppose the sign of the initial in-track offset. This results in the second intermediate trajectory safely drifting away from the target. The first intermediate trajectory brings the chaser safety towards the target assuming γ_0 is near γ_0^{ideal}.

The desired value of η that maintains passive safety, denoted η^{des}, depends on the sign of the initial in-track offset and the initial orientation:

$$\eta^{\text{des}} = \begin{cases} -1 & \text{sgn}(y_{r_0}) < 0, \ -\frac{\pi}{2} < \gamma_0 < \frac{\pi}{2} \\ -1 & \text{sgn}(y_{r_0}) > 0, \quad \gamma_0 < -\frac{\pi}{2} \text{ OR } \gamma_0 > \frac{\pi}{2} \\ 1 & \text{sgn}(y_{r_0}) > 0, \ -\frac{\pi}{2} < \gamma_0 < \frac{\pi}{2} \\ 1 & \text{sgn}(y_{r_0}) < 0, \quad \gamma_0 < -\frac{\pi}{2} \text{ OR } \gamma_0 > \frac{\pi}{2} \end{cases} \tag{10.16}$$

From Section 5.1.3, η is a function of desired changes to the cross-track parameters and the initial cross-track phase angle. However, without affecting the final desired trajectory, the sign of η can be changed implicitly by increasing the wait time until the first maneuver. Upon initially computing η, if η and η^{des} are unequal, changing the sign of η is achieved

using the following logic:

$$\tau_{\text{wait}} = \begin{cases} \tau_{\text{wait}} & \eta = \eta^{\text{des}} \\ \tau_{\text{wait}} + \pi & \eta \neq \eta^{\text{des}} \end{cases} \tag{10.17}$$

Incrementing τ_{wait} by π effectively increments ψ_1^- by π, which flips the sign of η. Equation (10.17) extends the possible wait time until the first maneuver by an additional half-orbit period. Therefore, an opportunity for a passively safe egress occurs every orbit period.

10.4.2 Instantaneous Center and Optimality

Section 5.1.5 derived bounds on the allowable changes to the instantaneous center that do not affect optimality for a general reconfiguration. This section approximates these bounds specifically for an offset safety ellipse to v-bar stationkeep. Approximations are made to reduce the expressions for these bounds to functions of $x_{r_1}^-$, $y_{r_1}^-$, η, γ_0, and a_0. Due to the decoupling of in-plane and out-of-plane motion, instantaneous center changes are independent of cross-track maneuvers.

To a attain a v-bar stationkeep, $x_{r_f} = 0$. This analysis assumes $\gamma_0 = \gamma_0^{\text{ideal}}$ (as well as $a_f = A_f = 0$), which leads to

$$\Delta\tilde{v}_x = 0,\ \Delta\tilde{v}_y = \pm\frac{1}{4}\eta\Omega a_0 \tag{10.18}$$

The sign ambiguity in equation (10.18) is due to whether $\gamma_0 = 0°$ or $\pm 180°$. Substituting equation (10.18) into equations (5.90) through (5.92), a costate solution exists when

$$\pm\frac{\eta}{a_0}\left(6x_{r_1}^- + \frac{8}{3\pi}\Delta y_{r_1}^-\right) \leq 1 \tag{10.19}$$

$$\pm\frac{\eta}{a_0}2x_{r_1}^- \geq -1 \tag{10.20}$$

$$\pm\frac{\eta}{a_0}\left(2x_{r_1}^- + \frac{8}{3\pi}\Delta y_{r_1}^-\right) \geq -1 \tag{10.21}$$

$x_{r_1}^-$ is the radial component of the instantaneous center immediately before the first maneuver. $\Delta y_{r_1}^-$ is the difference between the desired final in-track component of the instantaneous center and its value immediately before the first maneuver.

Equations (10.19) through (10.21) define polyhedrons in $(x_{r_1}^-, \Delta y_{r_1}^-)$ space that are functions of η, γ_0^{ideal}, and a_0. Figure 10.3 plots these polyhedrons. They represent, for particular values of η and γ_0^{ideal}, an approximate region of allowable instantaneous center changes immediately before the first maneuver that do not affect optimality of the analytic solution.

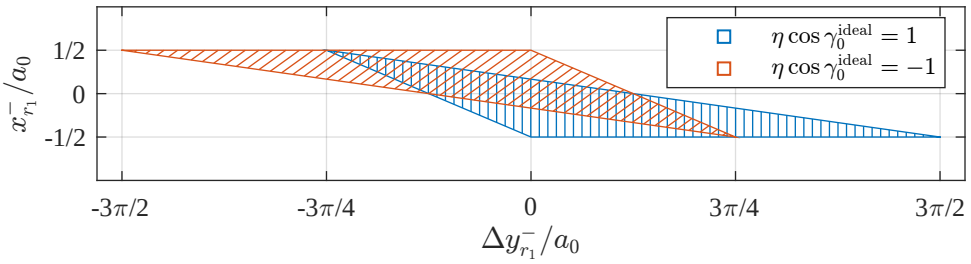

Fig. 10.3: Region approximating allowable $(x_{r_1}^-, \Delta y_{r_1}^-)$ pairs that do not affect optimality for particular values of η and γ_0^{ideal}.

The intersection of these sets was plotted for both resizing and phasing. For egress, however, a passively safe maneuver sequence requires a specific η, which makes the intersection of these sets less relevant. Figure 10.3 shows that the allowable instantaneous center changes are proportional to a_0.

10.4.3 Monte Carlo Analysis

Monte Carlo methods are used to validate optimality and analyze passive safety. Three test cases are conducted with each test case consisting of 250 samples.

Each individual Monte Carlo sample is an egress scenario involving a transfer from an offset safety ellipse to a v-bar stationkeep, and the transfer trajectory is computed both numerically and analytically. The problem is solved numerically using the SOCP in equation (4.52) with a fixed final time of multiple orbit periods to emulate the free-time problem.

General Setup

The Monte Carlo simulation relies on first defining an initial nominal safety ellipse. Table 10.1 lists the ROEs of the initial nominal safety ellipse that are consistent across all test cases.

Table 10.1: ROEs of the initial nominal safety ellipse for all test cases.

$x_{r_0}^n$ [m]	$y_{r_0}^n$ [m]	E_0^n [deg]	γ_0^n [deg]
0	-5000	$\mathcal{U}(-180, 180)$	0

The superscript 'n' denotes a nominal value. The initial nominal safety ellipse is always stationary, offset, and ideally oriented. The initial in-plane phase angle is drawn from a uniform distribution, $\mathcal{U}$, which randomizes the chaser's initial location along the safety ellipse.

The ROEs of the initial off-nominal safety ellipse are computed by adding dispersions to the nominal. The dispersions are drawn from zero-mean Gaussian distrbutions. The ROEs of the initial off-nominal safety ellipse are

$$x_{r_0} = x_{r_0}^n + \delta x_{r_0} \tag{10.22}$$

$$y_{r_0} = y_{r_0}^n + \delta y_{r_0} \tag{10.23}$$

$$a_0 = a_0^n + \delta a_0 \tag{10.24}$$

$$A_0 = A_0^n + \delta A_0 \tag{10.25}$$

$$\gamma_0 = \gamma_0^n + \delta \gamma_0 \tag{10.26}$$

where the variable $\delta(\cdot)$ is defined as a normally distributed random variable with zero mean and a variance denoted by $\sigma_{(\cdot)}^2$:

$$\delta(\cdot) := \mathcal{N}\left(0, \sigma_{(\cdot)}^2\right) \tag{10.27}$$

From the information in Table 10.1, equations (10.22) and (10.26) simplify to

$$x_{r_0} = \delta x_{r_0},\ \gamma_0 = \delta\gamma_0 \tag{10.28}$$

Computing a transfer trajectory requires defining the final desired v-bar stationkeep. Table 10.2 lists the ROEs of the final desired v-bar stationkeep that are consistent across all test cases.

Table 10.2: ROEs of the final desired v-bar stationkeep for all test cases.

x_{r_f} [m]	y_{r_f} [m]	a_f [m]	A_f [m]
0	$y^n_{r_0}$	0	0

By specifying $a_f = A_f = 0$, E_f and ψ_f become undefined. From equation (10.2), the maneuver direction is independent of ΔE and $\Delta\psi$. Substituting x_{r_0} from equation (10.28) into equation (5.84), the radial component of the instantaneous center immediately before the first maneuver is

$$x^-_{r_1} = \delta x_{r_0} \tag{10.29}$$

Substituting x_{r_0} from equation (10.28) and equation (10.23) into equation (5.86) and applying the information from Table 10.2, the difference between the desired final in-track component of the instantaneous center and its value immediately before the first maneuver is

$$\Delta y^-_{r_1} = \frac{3}{2}(\tau_{\text{wait}})\delta x_{r_0} - \delta y_{r_0} \tag{10.30}$$

Test Cases

Table 10.3 lists the initial nominal in-plane semi-major axis and cross-track amplitude for each test case.

Table 10.3: Egress test case parameters.

case #	a_0^n [m]	A_0^n [m]
1	1000	500
2	1000	250
3	250	125

Table 10.4 lists the variances of the Gaussian distributions in equations (10.22) through (10.26) in terms of 3-σ values for each test case.

Table 10.4: 3-σ ROE dispersions for each test case.

case #	x_{r_0} [m]	y_{r_0} [m]	a_0 [m]	A_0 [m]	γ_0 [deg]
1	50	100	100	50	15
2	50	100	100	25	15
3	50	100	25	12.5	5

Test cases 1 and 2 focus on analyzing optimality in terms of the primer vector conditions. Test case 3 focuses on the effect of instantaneous center changes on optimality. For test cases 1 and 2, a_0 is specified such that the 3-σ bounds on $x_{r_1}^-$ and $\Delta y_{r_1}^-$ are inside the region shown in Figure 10.3. For case 3, the 3-σ bounds exceed this region. Figure 10.4 shows the 3-σ bounds on $x_{r_1}^-$ and $\Delta y_{r_1}^-$ for $\tau_{\text{wait}} = 0$ (solid) and $\tau_{\text{wait}} = 2\pi$ (dashed) over the approximate allowable $(x_{r_1}^-, \Delta y_{r_1}^-)$ region for test cases 2 (blue) and 3 (red). The covariance ellipses are computed from equations (10.29) and (10.30). The maximum value of τ_{wait} is based upon the analysis of Section 10.4.1.

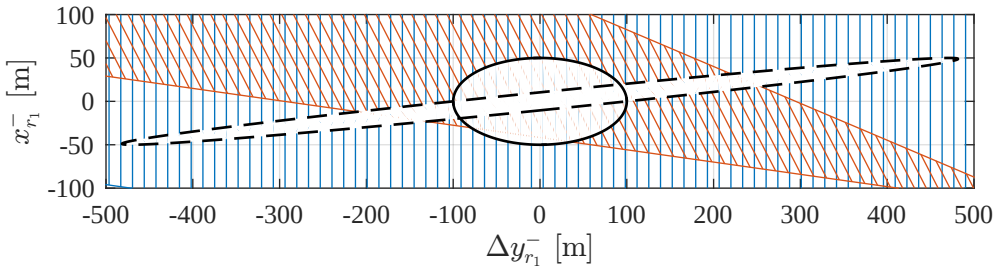

Fig. 10.4: 3-σ bounds on x_r^- and Δy_r^- for $\tau_{\text{wait}} = 0$ (solid) and for $\tau_{\text{wait}} = 2\pi$ (dashed) plotted over the approximate allowable $(x_{r_1}^-, \Delta y_{r_1}^-)$ region for test case 1 (blue) and 3 (red)

The $(x_{r_1}^-, \Delta y_{r_1}^-)$ regions are plotted for $\eta = -1$. From equation (10.16), this is the desired maneuver direction sign based upon the initial in-track offset and initial orientation. Figure 10.4 shows that a large initial radial offset is required to be outside the $(x_{r_1}^-, \Delta y_{r_1}^-)$ region, and a combination of a large $|x_{r_0}|$ and τ_{wait} increases the likelihood of a suboptimal analytic solution.

Results

Table 10.5 lists the percentage of Monte Carlo samples in which the analytic solution is optimal and the minimum ratio of the Δv from the SOCP solution to the Δv from the analytic solution for each test case.

Table 10.5: Percentage of optimal samples and minimum ratio of the numerical Δv to the analytic Δv for each test case.

case #	% of optimal samples	$\min(\Delta v_{\text{num}}/\Delta v_{\text{ana}})$
1	100	1.0000
2	99.2	0.9999
3	92.4	0.6487

For test case 2, the suboptimal samples are caused by violating equation (10.4). For both of these samples, $\gamma_0 > 15°$. As Figure 10.2 shows, slightly violating the primer vector conditions results in a marginal Δv penalty.

For test case 3, every suboptimal sample is caused by too large an instantaneous center change which results in a nonexistent costate solution. The maximum Δv penalty across all samples is roughly 30%. Figure 10.5 shows each sample of $x_{r_1}^-$ and $\Delta y_{r_1}^-$ plotted over the region approximating their allowable values for test case 3. The colors indicate whether the analytic solution is optimal (blue = optimal, black = suboptimal).

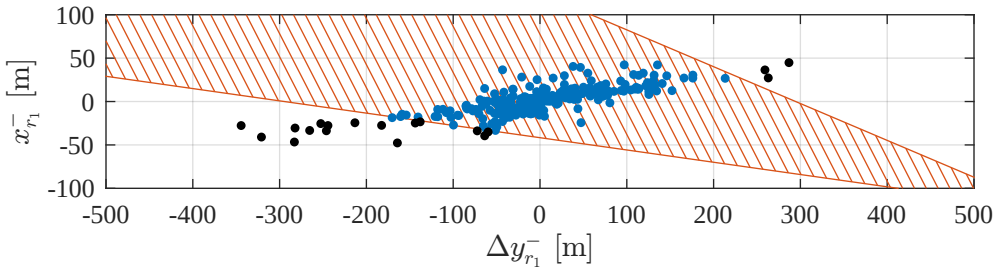

Fig. 10.5: $x_{r_1}^-$ and $\Delta y_{r_1}^-$ samples plotted over the approximate allowable $(x_{r_1}^-, \Delta y_{r_1}^-)$ region for test case 3. The colors denote optimality (blue = optimal, black = suboptimal)

Figure 10.5 shows that the suboptimal samples are outside the approximate allowable $(x_{r_1}^-, \Delta y_{r_1}^-)$ region. These are samples that have both a large initial radial offset and a long wait time until the first maneuver.

Since $\text{sgn}(y_{r_0}) < 0$ across all test cases, $x_{r_2}^+$ must be positive for a passively safe maneuver sequence. This value, along with d_1^+/a_0 and γ_1^+, are parameters that indicate the passive safety of the intermediate trajectories. Table 10.6 lists these passive safety parameters for each test case.

Table 10.6: Parameters indicating passive safety of the intermediate trajectories for each test case.

case #	$\min(x_{r_2}^+)$ [m]	$\min(\lvert d_1^+\rvert/a_0)$	$\max(\lvert\gamma_1^+\rvert)$ [deg]
1	79.00	0.16	17.6
2	78.96	0.16	17.5
3	-11.78	0.02	4.2

The results from test case 3 indicate that too large an instantaneous center change results in a potentially unsafe transfer trajectory. This is caused by the maneuver magnitudes deviating far from their nominal 1:2:1 ratios. Test cases 1 and 2 show that when the instantaneous center change is within its allowable $(x_{r_1}^-, \Delta y_{r_1}^-)$ region, the intermediate trajectories remain passively safe.

10.5 A Special Case of Safety Ellipse Egress to Co-Elliptic Flyby

Another possible egress scenario involves transfering from a safety ellipse to co-elliptic flyby. This section derives and analyzes a special case where the transfer is completed using only one maneuver. Figure 10.6 illustrates this scenario.

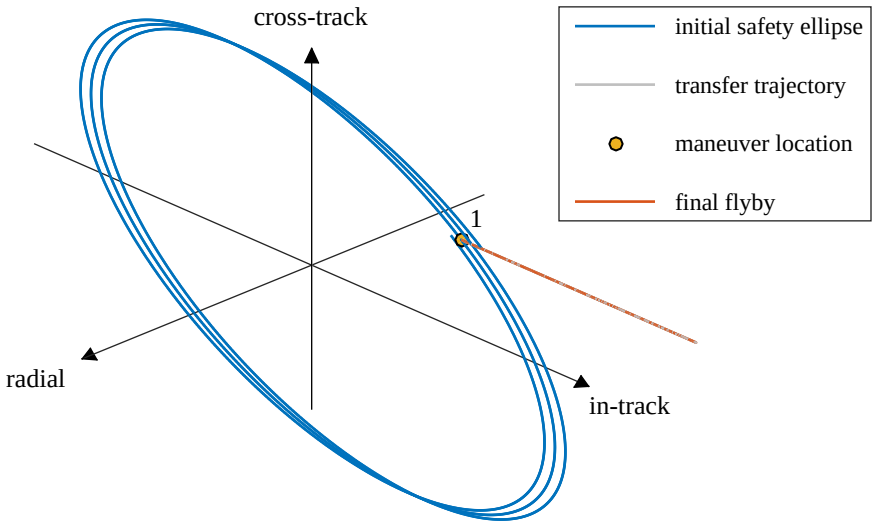

Fig. 10.6: An example of safety ellipse egress: safety ellipse to co-elliptic flyby.

A maneuver "sequence" consisting of a single maneuver requires two of the scale factors (maneuver magnitudes) in equations (5.78) through (5.80) to equal zero. The derivation in this section sets $\alpha_2 = \alpha_3 = 0$, which means that the desired changes to the safety ellipse are made entirely with the first maneuver. It is equally valid to set $\alpha_1 = \alpha_2 = 0$, however, this requires waiting an additional orbit period before the maneuver is performed, as the

chaser coasts through the times of the first two maneuvers.

Setting equation (5.79) equal to zero and solving for Δx_r results in

$$\Delta x_r = \frac{2}{\Omega}\Delta\tilde{v}_y \tag{10.31}$$

Substituting equation (10.31) into equation (5.80), setting it equal to zero, and solving for Δy_r results in

$$\Delta y_r = -\frac{1}{\Omega}6\pi\Delta\tilde{v}_y\left(\frac{1}{4} + \frac{1}{12\pi\Delta\tilde{v}_y}\left[4\Delta\tilde{v}_x + \big(6(\tau_f - \tau_3) + 9\pi\big)\Delta\tilde{v}_y\right]\right) \tag{10.32}$$

Substituting equations (10.31) and (10.32) into equation (5.78) confirms that the magnitude of the first maneuver equals the total required Δv:

$$\alpha_1 = \|\Delta\tilde{\boldsymbol{v}}\| \tag{10.33}$$

Substituting $\Delta\tilde{v}_y$ from equation (10.1) into equation (10.31), the flyby radial separation is

$$x_{r_f} = \eta\frac{1}{2}a_0\cos\gamma_0 + x_{r_0} \tag{10.34}$$

Equation (10.34) shows that the flyby radial separation depends on the state of the initial safety ellipse and cannot be arbitrarily specified. It also says that the sign of the radial separation, which dictates the direction of the chaser's flyby trajectory, depends on the sign of η. Equation (10.44) at the end of this section shows how to compute η given a desired flyby direction.

Substituting $\Delta\tilde{v}_x$ and $\Delta\tilde{v}_y$ from equation (10.1) and equation (4.7) into equation (10.32) and evaluating about τ_{wait}, the in-track offset immediately after the first maneuver is

$$y_{r_1}^{+} = y_{r_0} - \frac{3}{2}(\tau_{\text{wait}})x_{r_0} - \eta a_0\sin\gamma_0 \tag{10.35}$$

Equation (10.35) indicates the in-track offset at the time when the flyby begins. Like the radial offset, $y_{r_1}^+$ cannot be arbitrarily specified.

The ROEs immediately before the first maneuver are

$$x_{r_1}^- = x_{r_0} \tag{10.36}$$

$$y_{r_1}^- = y_{r_0} - \frac{3}{2}(\tau_{\text{wait}})x_{r_0} \tag{10.37}$$

$$a_1^- = a_0 \tag{10.38}$$

$$E_1^- = \gamma_0 + n\pi \tag{10.39}$$

$$A_1^- = A_0 \tag{10.40}$$

$$\psi_1^- = N\pi \tag{10.41}$$

where equation (10.39) follows from equation (10.3). The position vector immediately before the first maneuver is

$$\boldsymbol{r}_1^- = \begin{bmatrix} x_{r_0} - \frac{1}{2}a_0 \cos(\gamma_0 + N\pi) \\ y_{r_0} - \frac{3}{2}(\tau_{\text{wait}})x_{r_0} + a_0 \sin(\gamma_0 + N\pi) \\ 0 \end{bmatrix} \tag{10.42}$$

The cross-track position is zero because the maneuver occurs at the target's orbit plane crossing. From equations (10.34) and (10.35), the position vector immediately after the first maneuver is

$$\boldsymbol{r}_1^+ = \begin{bmatrix} x_{r_0} + \eta\frac{1}{2}a_0 \cos\gamma_0 \\ y_{r_0} - \frac{3}{2}(\tau_{\text{wait}})x_{r_0} - \eta a_0 \sin\gamma_0 \\ 0 \end{bmatrix} \tag{10.43}$$

$\boldsymbol{r}_1^-$ must equal $\boldsymbol{r}_1^+$, which means that η^{des} depends on the desired final flyby and initial orientation:

$$\eta^{\text{des}} = \begin{cases} -1 & \text{sgn}(x_{r_f}) < 0, \ -\frac{\pi}{2} < \gamma_0 < \frac{\pi}{2} \\ -1 & \text{sgn}(x_{r_f}) > 0, \quad \gamma_0 < -\frac{\pi}{2} \text{ OR } \gamma_0 > \frac{\pi}{2} \\ 1 & \text{sgn}(x_{r_f}) > 0, \ -\frac{\pi}{2} < \gamma_0 < \frac{\pi}{2} \\ 1 & \text{sgn}(x_{r_f}) < 0, \quad \gamma_0 < -\frac{\pi}{2} \text{ OR } \gamma_0 > \frac{\pi}{2} \end{cases} \tag{10.44}$$

Following the same procedure as equation (10.17), η^{des} is achieved by increasing τ_{wait} by a half orbit period when initially $\eta \neq \eta^{\text{des}}$. This means that the opportunity to initiate the maneuver sequence occurs every orbit period.

10.6 Summary

This chapter focused on safety ellipse egress, which was defined as a maneuver sequence that transfers a safety ellipse to another relative motion trajectory with zero in-plane semi-major axis and cross-track amplitude. The maneuver sequence and primer vector for a general egress were first analyzed. The key result from this analysis is an equation that relates optimality to the safety ellipse's initial orientation and initial ratio of the cross-track amplitude to in-plane semi-major axis. Next a scenario involving an offset safety ellipse to v-bar stationkeep was analyzed. It was shown that waiting up to an orbit period before the first maneuver is required for the intermediate trajectories to remain passively safe. Monte Carlo methods were used to validate optimality and analyze passive safety. Finally, a special egress case was presented, which showed that a transfer from a safety ellipse to co-elliptic flyby can be achieved using only one maneuver.

CHAPTER 11
ALGORITHM PERFORMANCE WITHIN A NONLINEAR SIMULATION

11.1 Overview

The derivations, analysis, and results from the proceeding chapters all assumed linear relative motion dynamics governed by the HCW equations and instantaneous and infinite control authority with impulsive Δv vectors. This chapter shows the implementation and performance of the maneuver sequence within a nonlinear orbit environment. The simulation specifically tests the viability of implementing the maneuver sequence as a waypoint generator and using analytic guidance laws to compute closed-loop, finite-thrust maneuvers between each waypoint.

The simulation only considers translational motion. It propagates the inertial states of the target and chaser using an orbit model with relevant perturbations. Maneuver planning and execution is computed closed-loop based upon current and desired relative states. Closed-loop maneuver computation is required to correct state dispersions, which are mainly caused by: 1) modeling errors between the linear HCW dynamics and nonlinear orbital dynamics and 2) conversion errors from inertial to linearized relative states. A commanded Δv is approximated by applying a constant thrust acceleration across the time of the impulse. Section 11.2.1 describes these processes in more detail, including the general simulation architecture and specific roles of the dynamics, targeting, guidance, and control functions.

Monte Carlo methods are applied to analyze safety ellipse resizing and phasing scenarios for both LEO and GEO regimes. Section 11.3.1 describes the specific simulation parameters and setup for each test case. Section 11.3.2 presents results showing the final relative state dispersions and statistics on the Δv required by the closed-loop system.

11.2 Implementation

This section presents the simulation architecture and setup. Here, architecture refers to defining and describing the general functions that are used within the simulation, and setup refers to the parameters and models used within each function.

11.2.1 Simulation Architecture

Figure 11.1 shows the simulation block diagram at its highest level. The dotted lines denote that the initialization block is called only once.

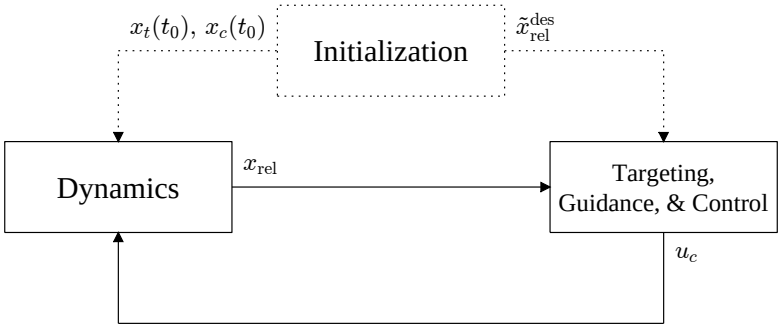

Fig. 11.1: Simulation block diagram.

$\boldsymbol{x}_t(t_0)$ and $\boldsymbol{x}_c(t_0)$ are the inertial state vectors of the target and chaser at the initial time, $\boldsymbol{x}_{\text{rel}}$ is the current relative state vector, and $\boldsymbol{u}_c$ is the chaser's thrust acceleration. $\tilde{\boldsymbol{x}}_{\text{rel}}^{\text{des}}$ contains desired relative states after the final maneuver and desired changes to relative states written in terms of the ROEs (see equations (4.6) through (4.11)). The elements of $\boldsymbol{x}_{\text{rel}}$ are shown in equation (3.17). Figure 11.1 shows a combined targeting, guidance, and control block. This block contains separate targeting, guidance, and control functions that are described later in this section.

Initialization

The simulation is initialized by specifying $\boldsymbol{x}_t(t_0)$, $\boldsymbol{x}_{\text{rel}}(t_0)$, and $\boldsymbol{x}_{\text{rel}}^{\text{des}}$. $\boldsymbol{x}_c(t_0)$ is computed from $\boldsymbol{x}_t(t_0)$ and $\boldsymbol{x}_{\text{rel}}(t_0)$ using Algorithm 48 from Vallado [65] which applies curvilinear corrections to improve the conversion accuracy. However, small conversion errors still exist.

Dynamics

The dynamics block propagates $\boldsymbol{x}_t$ and $\boldsymbol{x}_c$. Encke's method is used to formulate the differential equations of motion [66]. The environment models for each orbit regime are discussed in Section 11.2.2. After each propagation cycle, $\boldsymbol{x}_{\text{rel}}$ is computed from $\boldsymbol{x}_t$ and $\boldsymbol{x}_c$ using Algorithm 49 from Vallado [65]. Like Algorithm 48, curvilinear corrections are used to mitigate conversion errors.

Targeting

Figure 11.2 shows the block diagram within the targeting, guidance, and control block in Figure 11.1.

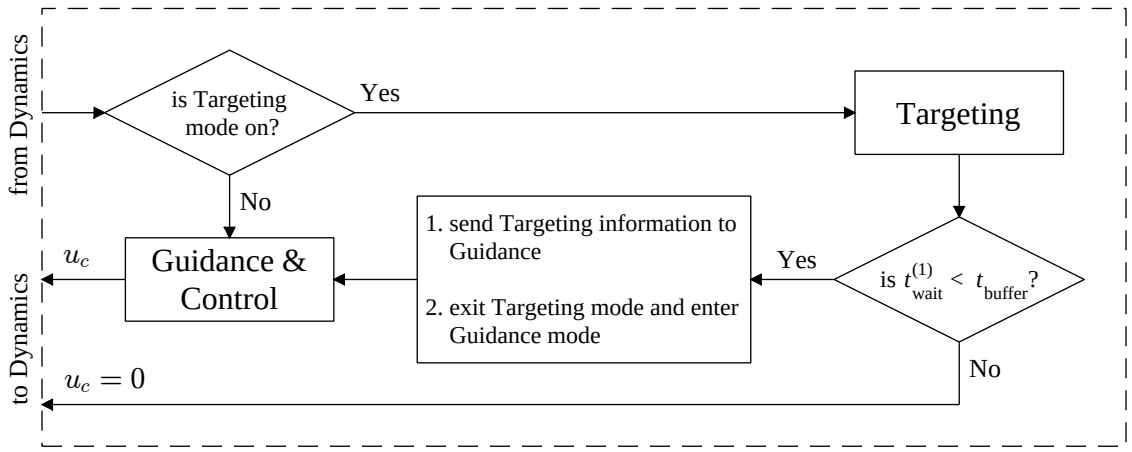

Fig. 11.2: Targeting, guidance, and control block diagram.

The targeting mode is turned on at the beginning of the simulation and is never reactivated once it is turned off. Table 11.1 lists the information received by the targeting block after each propagation cycle.

Table 11.1: Information sent to the targeting block from the dynamics and initialization blocks.

Parameter	Description
t	Current time
$\boldsymbol{x}_{\text{rel}}$	Current relative state vector
$\tilde{\boldsymbol{x}}_{\text{rel}}^{\text{des}}$	Desired relative state vector after the final maneuver (sent once from the initialization block)

Table 11.2 lists the information computed within the targeting block. Not all of this information is sent to guidance.

Table 11.2: Information computed within the targeting block.

Parameter	Description
$\Delta\boldsymbol{v}_k,\ k = 1, 2, 3$	Δv vectors at each maneuver time
$t_{\text{wait}}^{(1)}$	Wait time until the first maneuver
$t_k,\ k = 1, 2, m, 3$	Times of each maneuver, including a midcourse correction between maneuvers 2 and 3
$\boldsymbol{x}_{\text{rel}}^{\text{des}}(t_k),\ k = 2, m, 3$	Desired relative state vectors

The Δv vectors, maneuver times, and wait time until the first maneuver are computed using the equations in Sections 5.1.2 through 5.1.4.

The midcourse correction is a small maneuver that allows the chaser to correct its state dispersion. The time of the midcourse correction is

$$t_m = \frac{1}{2}(t_2 + t_3) \tag{11.1}$$

Although Table 11.2 lists a single midcourse correction, the number of midcourse corrections and their locations can be arbitrarily chosen.

The desired relative state vectors are computed by propagating a reference transfer trajectory that assumes HCW motion. For example, $\boldsymbol{x}_{\text{rel}}^{\text{des}}(t_k)$ is

$$\boldsymbol{x}_{\text{rel}}^{\text{des}}(t_k) = \Phi(t_k, t_1)\boldsymbol{x}_{\text{rel}}(t_1) + \sum_{j=1}^{k} \Phi(t_k, t_j) G \Delta \boldsymbol{v}_1 \tag{11.2}$$

where Φ and G are given in Section 3.1.2. Since the midcourse correction is not required under HCW dynamics, $\Delta \boldsymbol{v}_m = 0$ when computing the reference trajectory.

The desired relative state vectors act as waypoints located along the reference trajectory. Figure 11.3 illustrates this concept for a nominal resizing scenario (although $\boldsymbol{x}_{\text{rel}}$ is described in terms of LROEs, it can be readily converted to a relative position and velocity using equation (3.18)).

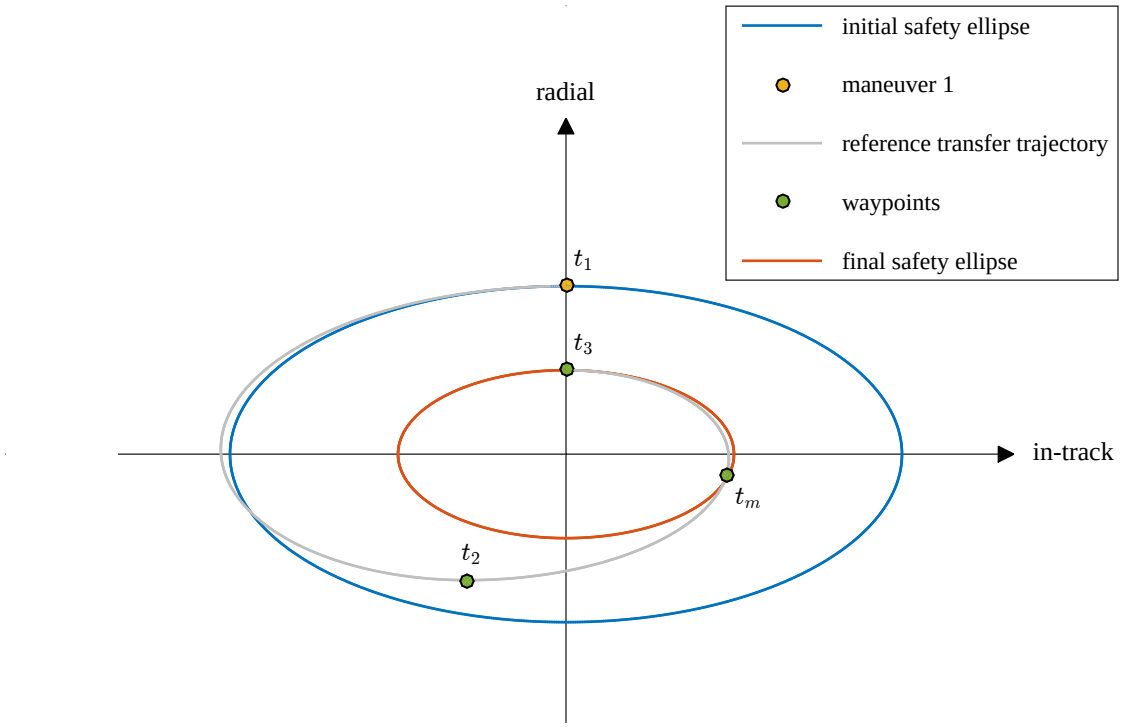

Fig. 11.3: An example of waypoints along a reference transfer trajectory plotted in the radial/in-track plane.

Errors due to dynamics modeling, state conversions, and finite-thrust maneuvers cause the chaser to deviate from the reference trajectory. The waypoints allow the chaser to compute closed-loop maneuvers to mitigate state dispersions.

As time increments with each propagation cycle, $t_{\text{wait}}^{(1)}$ decreases. When $t_{\text{wait}}^{(1)}$ is below a certain threshold (t_{buffer}), the targeting mode is permanently turned off and the guidance mode is turned on. t_{buffer} emulates a period of time required before a maneuver for attitude slewing, thruster preparation, etc. Table 11.3 lists the information that the targeting block sends the guidance block upon exiting the targeting mode.

Table 11.3: Information output from the targeting block.

Parameter	Description
$\Delta \boldsymbol{v}_1$	Maneuver 1
$t_k,\ k = 1, 2, m, 3$	Maneuver times
$\boldsymbol{x}_{\text{rel}}^{\text{des}}(t_k),\ k = 2, m, 3$	Desired relative state vectors

Guidance

Figure 11.4 shows the block diagram within the guidance and control block in Figure 11.2.

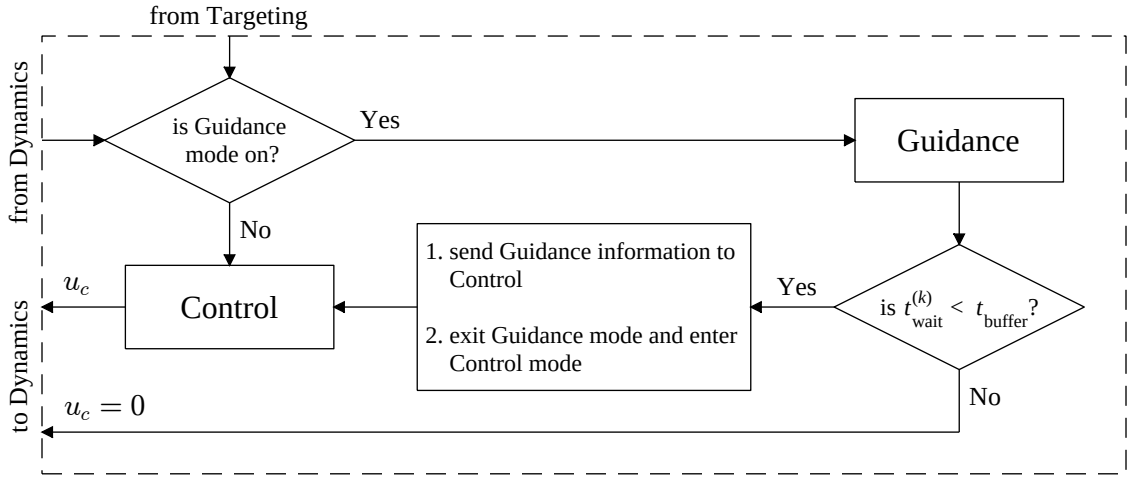

Fig. 11.4: Guidance and control block diagram.

The guidance mode does not turn on until the targeting mode is exited. After that, the mode toggles between guidance and control. Table 11.3 lists the information that is sent to the guidance block when it is initially activated. Table 11.1 lists the additional information received by the guidance block after each propagation cycle, except for $\boldsymbol{x}_{\text{rel}}^{\text{des}}$.

Table 11.4 lists the information computed within the guidance block. For every variable, $k = 1, 2, m, 3$.

Table 11.4: Information computed within the guidance block.

Parameter	Description
$\Delta\hat{\boldsymbol{v}}_k$	Direction of the kth Δv vector
$t_{\text{wait}}^{(k)}$	Wait time until the kth maneuver
$t_{\text{start}}^{(k)}$	Start time of the chaser's thrust acceleration for the kth maneuver
$t_{\text{stop}}^{(k)}$	Stop time of the chaser's thrust acceleration for the kth maneuver

The wait time until the kth maneuver is

$$t_{\text{wait}}^{(k)} = t_k - t \tag{11.3}$$

To compute the start and stop times of the chaser's thrust acceleration, first the maneuver duration (Δt_k) is computed:

$$\Delta t_k = \frac{\|\Delta \boldsymbol{v}_k\|}{u_{\max}} \tag{11.4}$$

where $u_{\max}$ is a specified maximum thrust acceleration. The start and stop times are then

$$t_{\text{start}}^{(k)} = t_k - \frac{1}{2}\Delta t_k, \quad t_{\text{stop}}^{(k)} = t_k + \frac{1}{2}\Delta t_k \tag{11.5}$$

From equation (11.5), the duration of the thrust acceleration is centered about the time of the impulse. The computation of $\Delta\hat{\boldsymbol{v}}_k$ depends on the maneuver number. Table 11.5 shows how the guidance procedure varies with maneuver number.

Table 11.5: Guidance procedures for each maneuver (or set of maneuvers).

Maneuver	Procedure
1 (initial)	$\Delta \boldsymbol{v}_1$ computed by targeting
$2, m$ (intermediate)	Two-impulse targeting between waypoints
3 (final)	Least-squares approach to minimize final dispersion

The first maneuver is not changed from targeting because $t_{\text{wait}}^{(1)} < t_{\text{buffer}}$. At this point, the guidance mode is exited and the control mode is activated.

The intermediate maneuvers are computed using two-impulse targeting. As the chaser approaches t_k, it computes the two-impulse solution to achieve the desired state at t_{k+1}:

$$\begin{bmatrix} \Delta \boldsymbol{v}_k \\ \Delta \boldsymbol{v}_{k+1} \end{bmatrix} = M^{-1} \left(\boldsymbol{x}_{\text{rel}}^{\text{des}}(t_k) - \Phi(t_{k+1}, t) \boldsymbol{x}_{\text{rel}}(t) \right) \tag{11.6}$$

where

$$M = \begin{bmatrix} \Phi(t_{k+1}, t_k) G & G \end{bmatrix} \tag{11.7}$$

Equation (11.6) is updated with each propagation cycle as t and $\boldsymbol{x}_{\text{rel}}(t)$ are received from the dynamics block. Although equation (11.6) computes two Δv vectors, only $\Delta \boldsymbol{v}_k$ is used.

The final maneuver is computed using a least-squares approach. Due to errors from dynamics modeling, state conversions, and finite-thrust maneuvers, the chaser is not at its desired final state at the time of the final maneuver. With only one maneuver, the chaser cannot instantaneously change its entire state vector. Immediately after the final maneuver

$$\delta \boldsymbol{x}_{\text{rel}}^{+}(t_3) = \delta \boldsymbol{x}_{\text{rel}}^{-}(t_3) + G \Delta \boldsymbol{v}_3 \tag{11.8}$$

where

$$\delta \boldsymbol{x}_{\text{rel}}(t_3) = \boldsymbol{x}_{\text{rel}}^{\text{des}}(t_3) - \boldsymbol{x}_{\text{rel}}(t_3) \tag{11.9}$$

$\boldsymbol{x}_{\text{rel}}(t_3)$ is update each propagation cycle by

$$\boldsymbol{x}_{\text{rel}}(t_3) = \Phi(t_3, t)\boldsymbol{x}_{\text{rel}}(t) \tag{11.10}$$

The objective of the maneuver is to minimize the state dispersion:

$$\underset{\Delta \boldsymbol{v}}{\text{minimize}} \, \|\delta \boldsymbol{x}^{+}_{\text{rel}}(t_3)\| \tag{11.11}$$

Equation (11.11) is a least-squares problem with the solution

$$\Delta \boldsymbol{v}_3 = -\left(G^T G\right)^{-1} G^T \delta \boldsymbol{x}^{-}_{\text{rel}}(t_3) \tag{11.12}$$

When $t^{(k)}_{\text{wait}} < t_{\text{buffer}}$, the guidance mode is turned off and the control mode is activated. At that time, the guidance block sends $\Delta\hat{\boldsymbol{v}}_k$, $t^{(k)}_{\text{start}}$, $t^{(k)}_{\text{stop}}$ (see Table 11.4) to the control block.

Control

Figure 11.5 shows the block diagram within the control block in Figure 11.4.

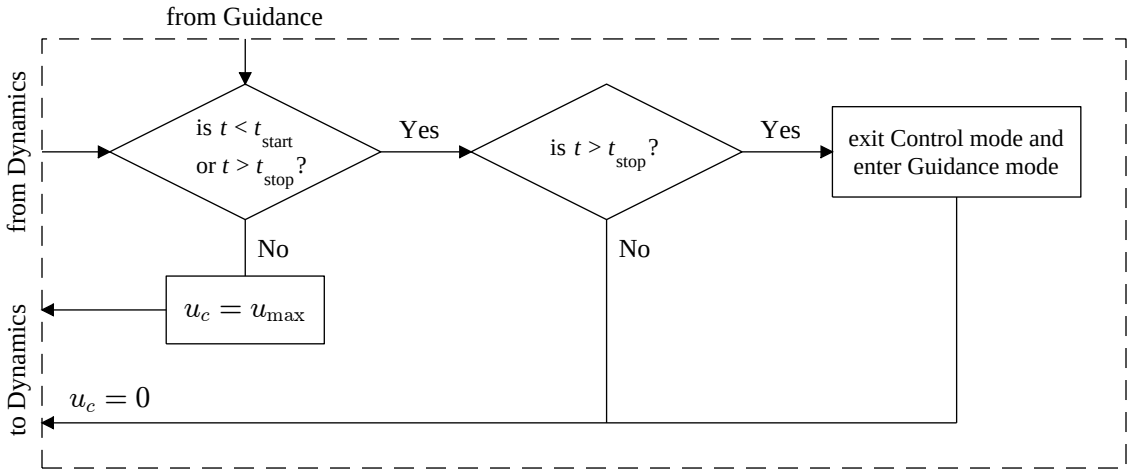

Fig. 11.5: Control block diagram

The control mode is turned on when $t_{\text{wait}}^{(k)} < t_{\text{buffer}}$. At that time, the control block receives $\Delta\hat{\boldsymbol{v}}_k$, $t_{\text{start}}^{(k)}$, $t_{\text{stop}}^{(k)}$ from the guidance block. Depending on the propagation step size (Δt) and the length of t_{buffer}, there may be multiple propagation cycles where the control mode is active but the chaser's thrust acceleration is turned off. When t_{start} is within the next propagation cycle, outside of the control block, Δt is adjusted such that $t_{\text{start}} = t + \Delta t$ and $t_{\text{stop}} = t_{\text{start}} + \Delta t_k$. When $t = t_{\text{start}}$, the chaser's thrust acceleration is set to $u_{\max}$, and the differential equations are integrated over Δt_k. When $t > t_{\text{stop}}$, the control mode is exited, the guidance mode is reactivated, and Δt is adjusted back to its default value.

11.2.2 Setup

Table 11.6 lists the simulation parameters and models. The superscript denotes the particular orbit regime. a_p denotes the perturbing accelerations included in the differential equations of motion.

Table 11.6: Simulation parameters and models.

parameter	value
t_{buff}	300 s
$u_{\max}$	5 mm/s^2
Δt^{LEO}	10 s
Δt^{GEO}	100 s
a_p^{LEO}	8×8 gravity, drag, lunisolar
a_p^{GEO}	4×4 gravity, lunisolar

The perturbations are selected based upon Figure 3.1 from [67] which plots the approximate relative acceleration of various perturbations as a function of the distance from the center of the Earth. Equations for computing these perturbations can be found in Chapter 8 of Vallado [65]. For the drag model, the 1976 U.S. Standard Atmosphere [68] lookup table is used to determine atmospheric density.

11.3 Monte Carlo Analysis

Monte Carlo methods are applied to the nonlinear simulation. Each Monte Carlo simulation involves a combination of a safety ellipse reconfiguration, orbit regime, perturbation environment, and target eccentricity. For example, one Monte Carlo simulation consists of a centered resizing scenario, in GEO, for 2-body motion, with a target eccentricity of 1×10^{-4}. The perturbation environment is either 2-body motion or the model listed in Table 11.6. Eccentricity is varied because it also affects the accuracy of the HCW equations. Each Monte Carlo simulation consists of 250 samples.

11.3.1 Setup and Test Cases

Table 11.7 lists the target's inertial orbital elements at the initial time. Ω_{RA_0} is the initial right ascension of the ascending node, ω_0 is the initial argument of perigee, and ν_0 is the initial true anomaly. $\mathcal{U}$ denotes a uniform distribution.

Table 11.7: Target's inertial orbital elements at the initial time.

parameter	value(s)
a_0^{LEO}	6878 km
a_0^{GEO}	42 167 km
i_0^{LEO}	$45^\circ + \mathcal{U}(0, 45^\circ)$
i_0^{GEO}	$\mathcal{U}(0, 10^\circ)$
e_0	$1 \times \{10^{-5}, 10^{-4}, 10^{-3}, 10^{-2}$ (LEO only)$\}$
Ω_{RA_0}	$\mathcal{U}(0, 360^\circ)$
ω_0	$\mathcal{U}(0, 360^\circ)$
ν_0	$\mathcal{U}(0, 360^\circ)$

The initial altitude of the LEO regime is approximately 500 km. The orbital elements involving angles are all randomized. These angles do not directly affect the accuracy of the HCW equations, but they do alter the direction and magnitude of the gravitational and

third body perturbing accelerations.

Table 11.8 lists spacecraft parameters pertinent to the drag model. AMR denotes the area-to-mass ratio, and C_d denotes the coefficient of drag. $\mathcal{N}$ denotes a uniform distribution.

Table 11.8: Spacecraft parameters.

parameter	value
AMR	$\mathcal{N}(\text{AMR}^n, \sigma^2_{\text{AMR}})$
AMR^n	$0.01\,\text{m}^2/\text{kg}$
3-σ_{AMR}	0.1AMR^n
C_d	$\mathcal{N}(C_d^n, \sigma^2_{C_d})$
C_d^n	2.2
3-σ_{C_d}	$0.1C_d^n$

The initial area-to-mass ratios and coefficients of drag are randomized for both the target and chaser.

There are three reconfiguration cases: centered resizing, centered phasing, and offset resizing. Tables 11.9 through 11.11 list, for each reconfiguration case, the initial nominal safety ellipse, initial dispersions, and desired final safety ellipse in terms of the ROEs.

Table 11.9: Initial nominal ROEs, initial ROE dispersions, and final ROEs for centered resizing.

	x_r [m]	y_r [m]	a [m]	E [deg]	A [m]	γ [deg]
nominal	0	0	1000	$\mathcal{U}(-180, 180)$	500	0
3-σ dispersion	50	100	100	15	50	15
final	0	0	500	E^n	250	0

Table 11.10: Initial nominal ROEs, initial ROE dispersions, and final ROEs for centered phasing.

	x_r [m]	y_r [m]	a [m]	E [deg]	A [m]	γ [deg]
nominal	0	0	500	$\mathcal{U}(-180, 180)$	250	0
3-σ dispersion	25	50	50	15	25	15
final	0	0	500	$E^n + 60$	250	0

Table 11.11: Initial nominal ROEs, initial ROE dispersions, and final ROEs for offset resizing.

	x_r [m]	y_r [m]	a [m]	E [deg]	A [m]	γ [deg]
nominal	0	-5000	1000	$\mathcal{U}(-180, 180)$	500	0
3-σ dispersion	50	100	100	15	50	15
final	0	-5000	500	E^n	250	0

The parameters for centered resizing and offset resizing are identical, except for y_{r_0}. Comparing Tables 11.9 and 11.10, the dimensions of the final desired safety ellipses are the equal. With no dispersions (and assuming HCW motion), the total Δv for each reconfiguration case is identical.

11.3.2 Results

The results shown in this section are categorized by reconfiguration type and orbit regime. Each category shows a plot of the 3-σ ROE dispersions after the final maneuver and statistics on the ratio of the total Δv to open-loop Δv as a function of target eccentricity. This is shown for both 2-body (blue) and perturbed (red) orbital motion.

The total Δv is the sum of the Δv vectors computed by guidance. The open-loop Δv is the sum of the Δv vectors computed by targeting at the time of its final cycle (see Table 11.2). Without errors due to dynamics modeling, state conversions, and finite-thrust maneuvers, $\Delta v = \Delta v^{\mathrm{open-loop}}$.

Centered Resizing in GEO

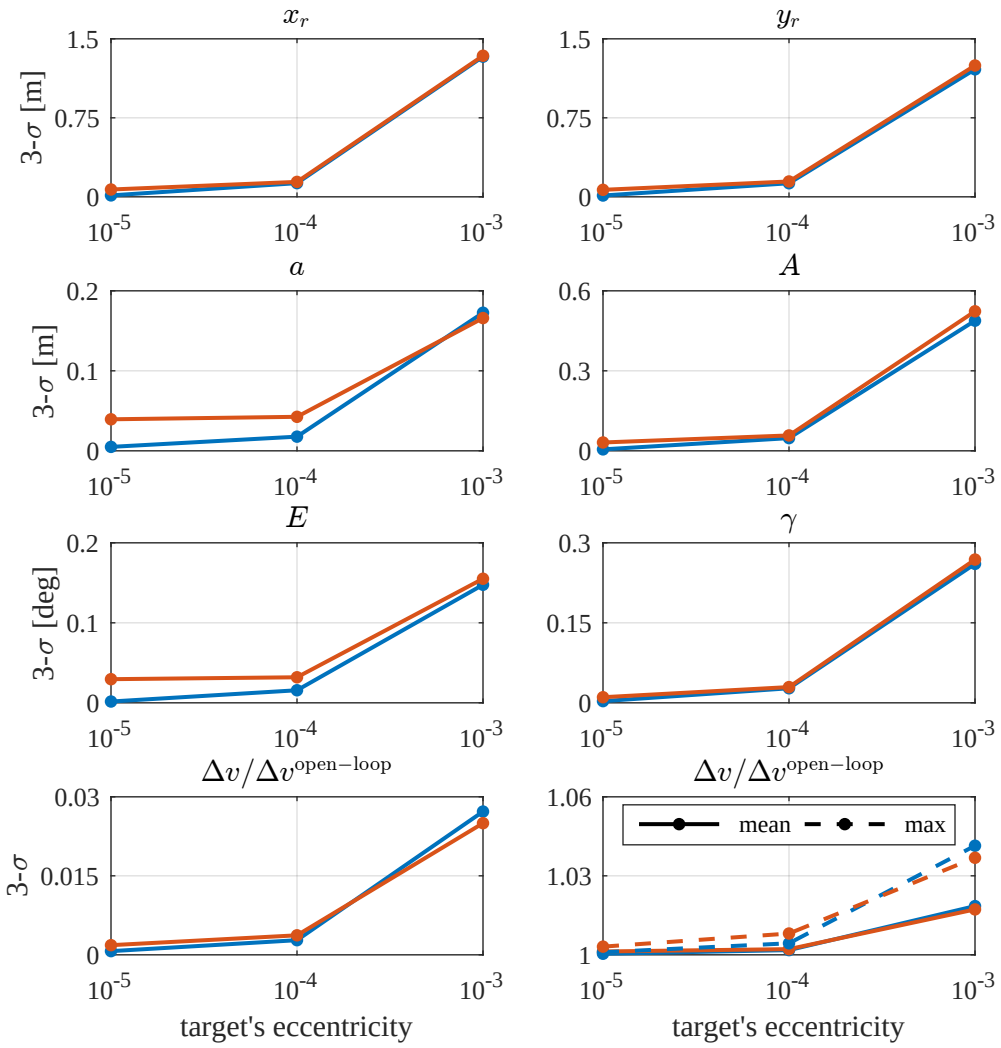

Fig. 11.6: 3-σ ROE dispersions and statistics on the ratio of the total Δv to open-loop Δv as a function of target eccentricity for 2-body (blue) and perturbed (red) orbit environments.

Figure 11.6 shows that for this test case, the dominant source of modeling error is eccentricity rather than non-Keplerian motion. This is indicated by the overall similarity between the data points for 2-body and perturbed orbital motion. The guidance system performs well even for a large GEO eccentricity ($e = 1 \times 10^{-3}$) and perturbed orbit environment, resulting in maximum individual ROE dispersions of 1.5 m and 0.3° and requiring at most 5% more Δv than the open-loop.

Centered Resizing in LEO

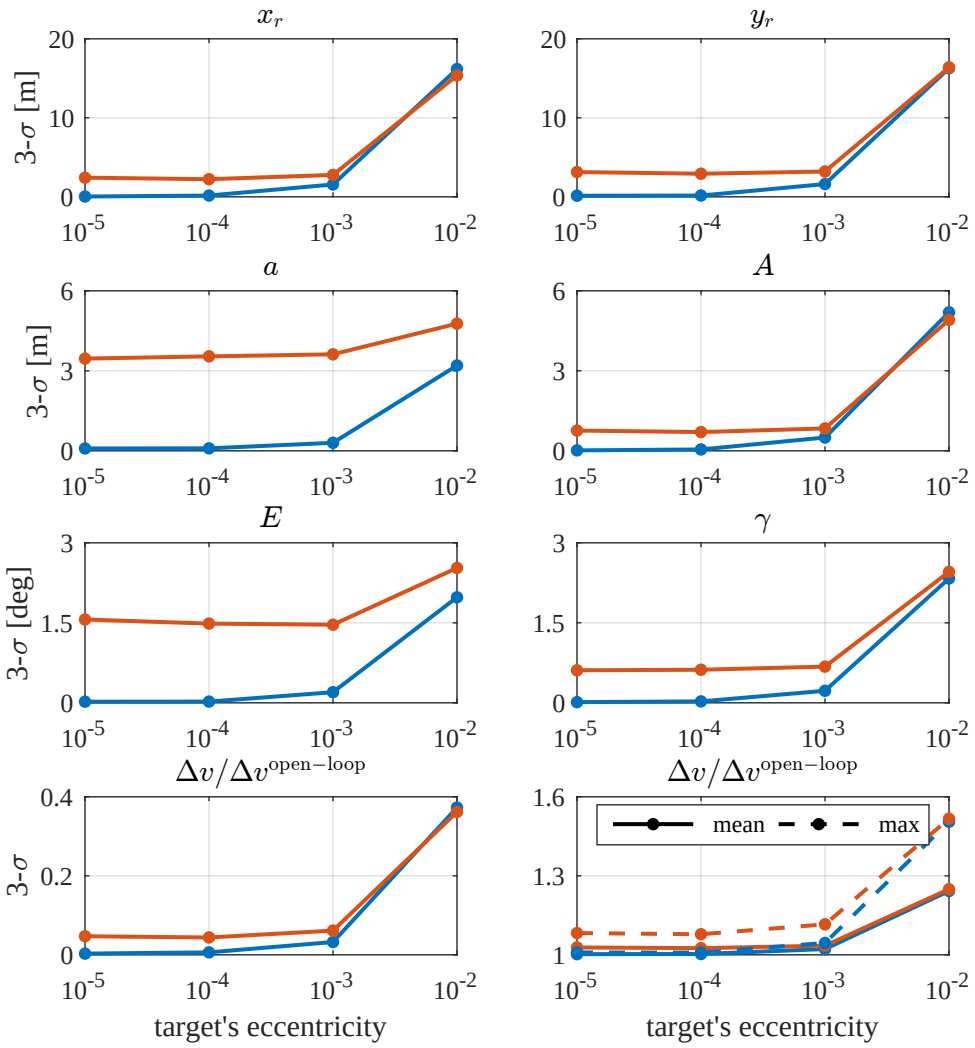

Fig. 11.7: 3-σ ROE dispersions and statistics on the ratio of the total Δv to open-loop Δv as a function of target eccentricity for 2-body (blue) and perturbed (red) orbit environments.

Figure 11.7 shows that, unlike GEO resizing, the dominant source of modeling error is non-Keplerian motion for $e \leq 1 \times 10^{-3}$, as those data points for perturbed orbital motion are nearly constant. This is because the strongest LEO perturbations (J_2, drag) are orders of magnitude larger than the strongest GEO perturbations (J_2, lunisolar) [67]. Although the results seem to indicate an inflection point at $e = 1 \times 10^{-3}$, more data is needed to confirm this trend. At that point, the guidance system results in maximum individual ROE dispersions of 5 m and 1.5° and requires at most 15% more Δv than the open-loop.

Centered Phasing in GEO

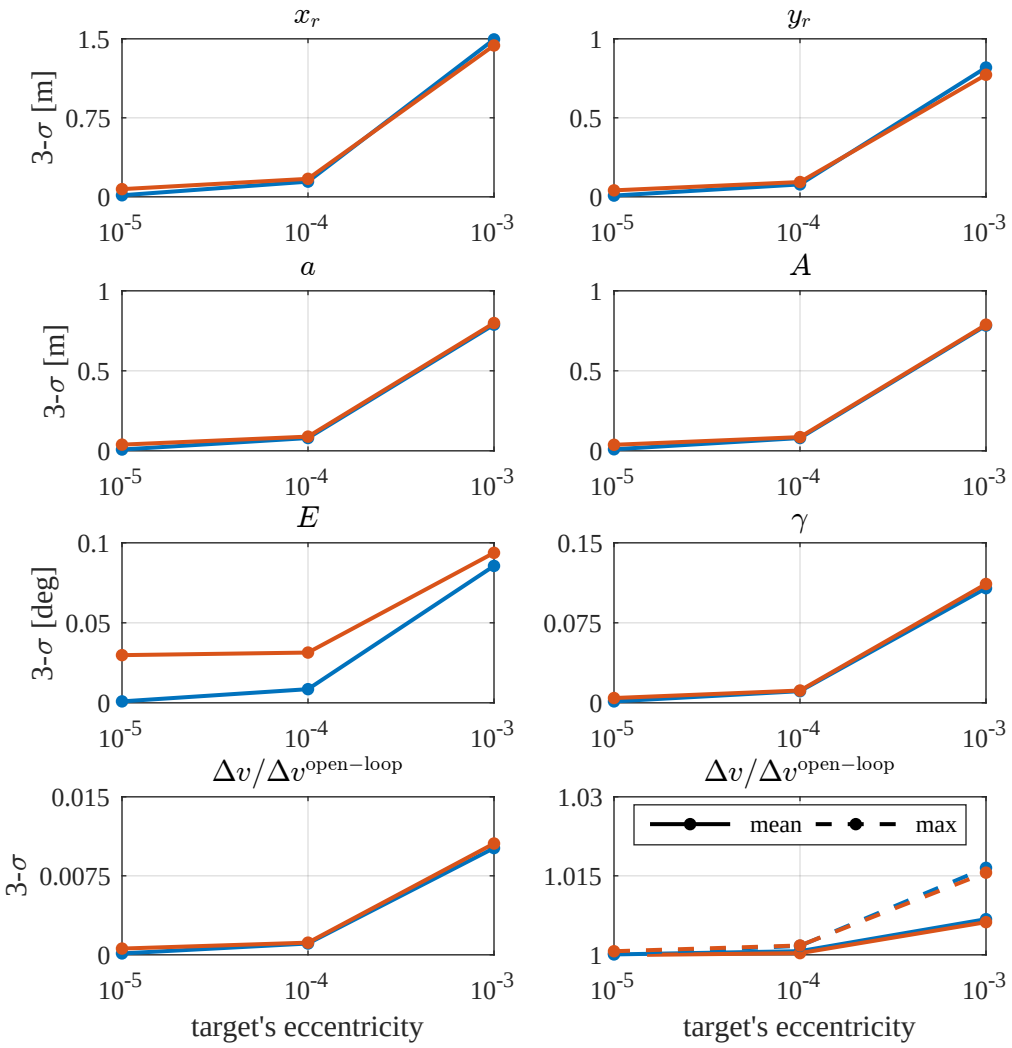

Fig. 11.8: 3-σ ROE dispersions and statistics on the ratio of the total Δv to open-loop Δv as a function of target eccentricity for 2-body (blue) and perturbed (red) orbit environments.

The results shown in Figure 11.8 mimic the results for GEO resizing: the dominant source of modeling error is eccentricity, and the guidance system results in small ROE dispersions and requires a marginal additional Δv. There are differences, however, in the individual ROE dispersions and Δv ratio statistics. For example, the standard deviation, mean, and maximum values of $\Delta v/\Delta v^{\text{open-loop}}$ are all roughly half that for resizing. More testing is needed to better understand this behavior.

Centered Phasing in LEO

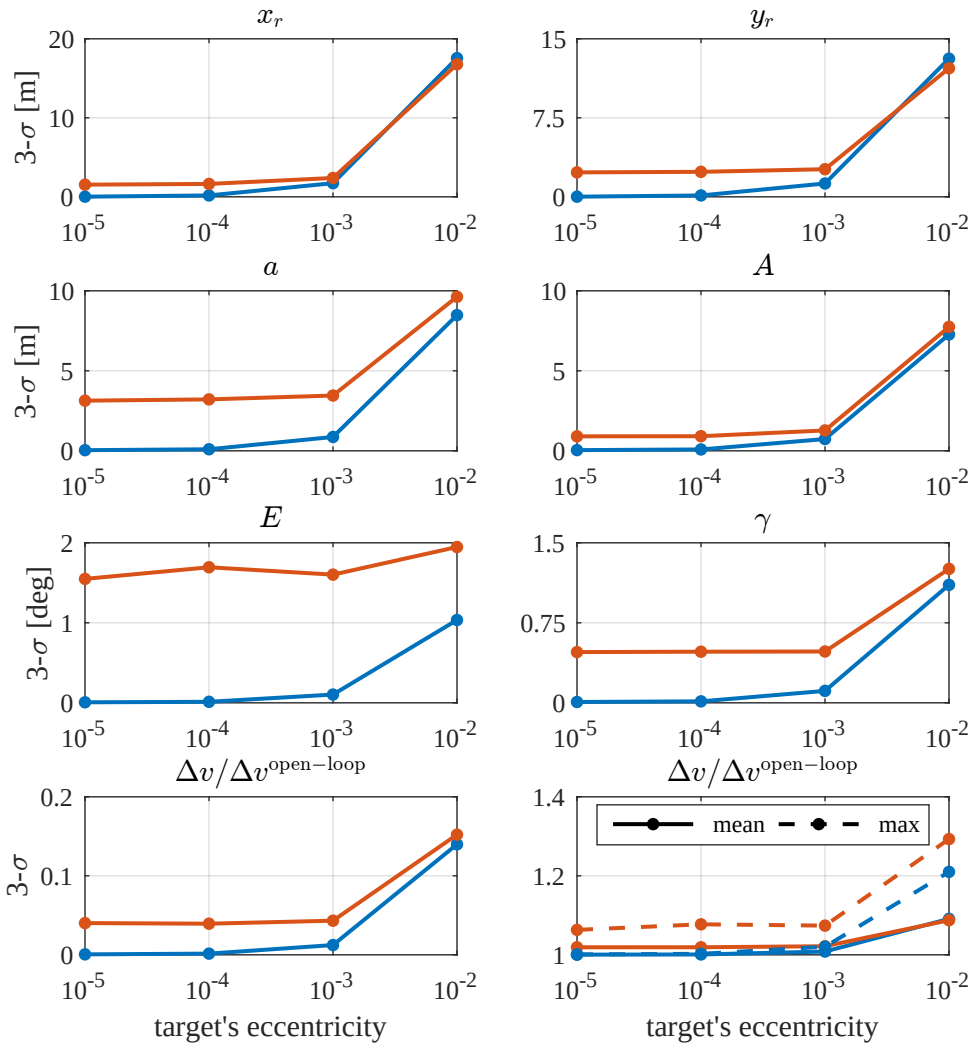

Fig. 11.9: 3-σ ROE dispersions and statistics on the ratio of the total Δv to open-loop Δv as a function of target eccentricity for 2-body (blue) and perturbed (red) orbit environments.

The results shown in Figure 11.9 mimic the results for LEO resizing: the dominant source of modeling error is non-Keplerian motion for $e \leq 1 \times 10^{-3}$, and the guidance system shows a sharp decline in performance from $e = 1 \times 10^{-3}$ to $e = 1 \times 10^{-2}$. The differences between LEO phasing and resizing are also similar to the differences between GEO phasing and resizing; for example, the standard deviation, mean, and maximum values of $\Delta v/\Delta v^{\text{open-loop}}$ are all roughly half that for resizing.

Offset Resizing in GEO

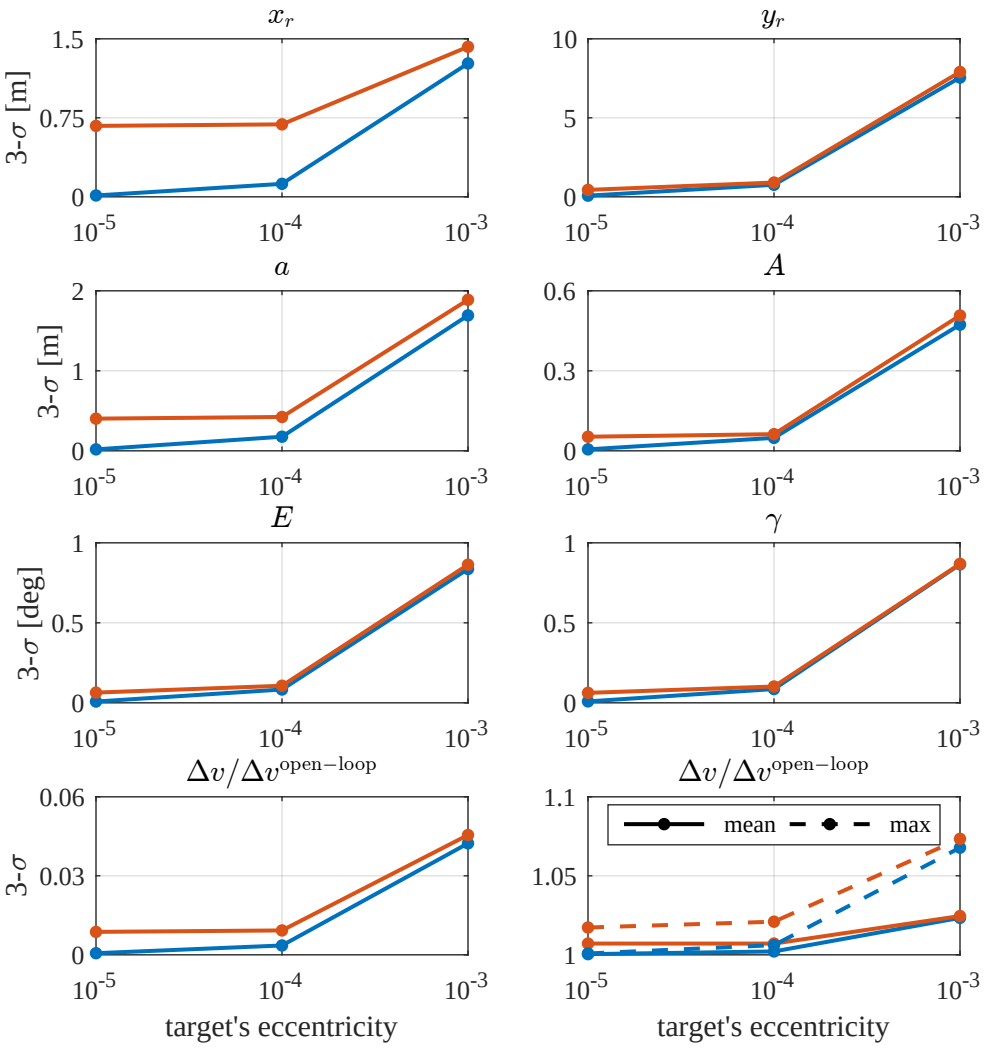

Fig. 11.10: 3-σ ROE dispersions and statistics on the ratio of the total Δv to open-loop Δv as a function of target eccentricity for 2-body (blue) and perturbed (red) orbit environments.

The only difference in setup between this test case and GEO centered resizing is a 5 km in-track offset. However, compared to Figure 11.6, there are larger dispersions in y_r, a, E, γ, and $\Delta v/\Delta v^{\text{open-loop}}$. Given the initial offset, larger y_r dispersions can be expected. However, the other increases suggest that conversion errors become more influential as the safety ellipse is moved away from the origin of the LVLH frame. Overall, the guidance system still performs well for $e = 1 \times 10^{-3}$ and a perturbed orbit environment, resulting in relatively small ROE dispersions and requiring at most 8% more Δv than the open-loop.

Offset Resizing in LEO

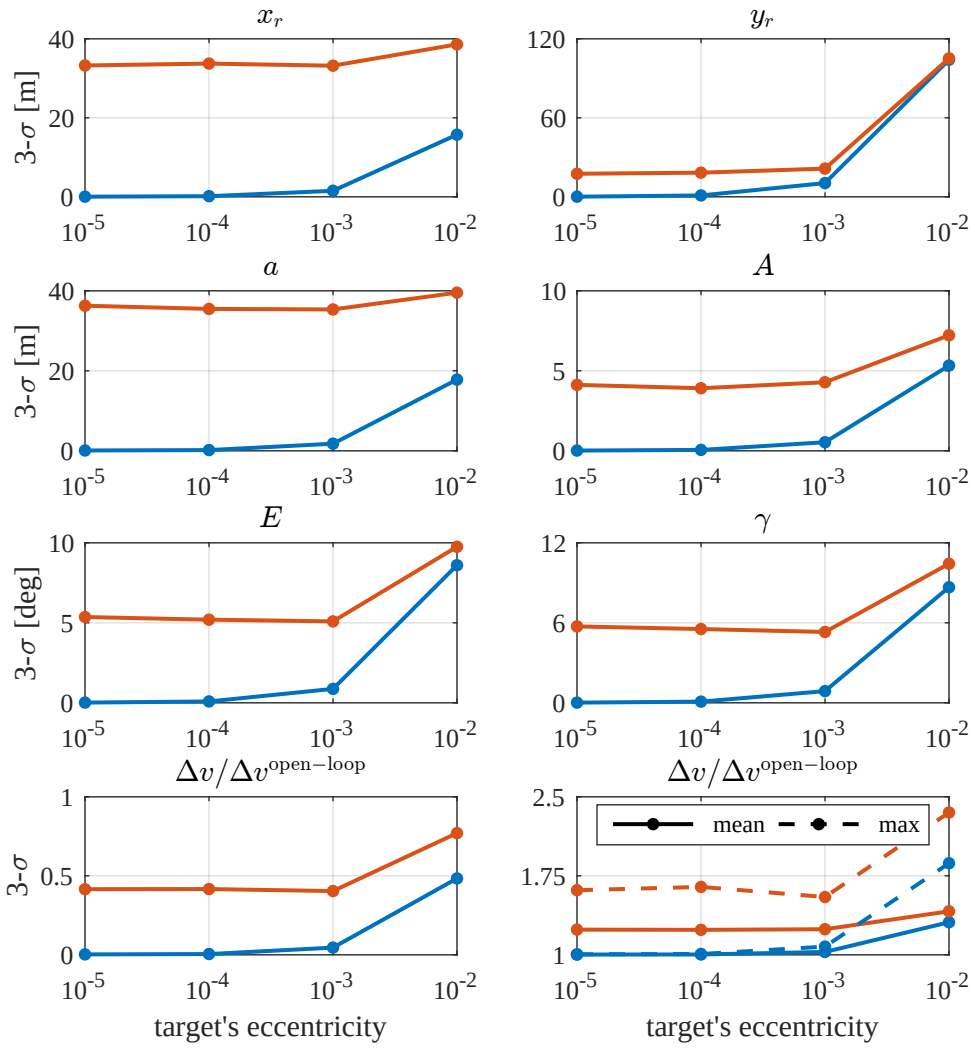

Fig. 11.11: 3-σ ROE dispersions and statistics on the ratio of the total Δv to open-loop Δv as a function of target eccentricity for 2-body (blue) and perturbed (red) orbit environments.

Similar to the differences between GEO centered resizing and GEO offset resizing, Figure 11.11 shows a degradation in performance compared to LEO centered resizing. Here the degradation is more severe, especially for perturbed orbital motion. The key takeaway from these results is that directly converting osculating inertial states to the relative state results in motion that deviates from the HCW equations as the separation between the target and chaser increases. This trend is amplified in LEO due to perturbations that cause short-period oscillations. Future work involves applying conversion techniques that

use mean orbital elements, as well as relative state representations that are better suited for LEO [15].

11.4 Summary

This chapter presented the implementation and performance of the maneuver sequence within a nonlinear orbit environment. The simulation introduced modeling, conversion, and finite-thrust errors to reconfiguration scenarios that had previously considered strictly HCW motion and impulsive control authority. The maneuver sequence was implemented as a waypoint generator and analytic guidance laws were used to compute closed-loop, finite-thrust maneuvers between each waypoint. A complete overview of the simulation was provided, including the specific computations within the targeting, guidance, and control functions. Monte Carlo methods were applied to analyze safety ellipse resizing and phasing scenarios for both LEO and GEO regimes. The guidance system performed well for scenarios that more closely resembled HCW motion– reconfigurations in GEO resulted in lower state dispersions and smaller differences in open and closed-loop Δv compared to the same scenarios in LEO. The offset resizing scenario in LEO showed that there is room for improvement with the conversion process from inertial to linearized relative states.

CHAPTER 12
CONCLUSIONS AND FUTURE WORK

12.1 Conclusions

This work presented the derivation, analysis, and application of analytic maneuver sequences for safety ellipse resizing, phasing, ingress, and egress scenarios. Mathematically, these scenarios all fall under the category of a general reconfiguration. In deriving the maneuver sequence for a general reconfiguration, it was proposed that the solution consists of three impulses spaced apart by a half-orbit period. By applying primer vector theory, it was then shown that an optimal solution candidate is comprised of colinear impulses, with the second maneuver pointing opposite the first and third maneuvers. Additional primer vector analysis established when the maneuver sequence satisfies the necessary conditions for optimality. For a standard reconfiguration scenario where both the in-plane and out-of-plane phase angles are specified, it was shown that satisfying the primer vector conditions is dependent on a relationship between the cross-track and radial components of the colinear maneuver direction. The necessary conditions also relied on the existence of a costate vector, which was shown to be violated when desired changes to the safety ellipse's instantaneous center are large relative to the reconfiguration component.

The general maneuver sequence was then separately analyzed for each reconfiguration scenario. The resizing, phasing, and ingress scenarios were separated into two categories: nominal and off-nominal. For nominal reconfigurations, an analytic expression was derived that describes the relationship between the necessary conditions for optimality and properties of the initial and final safety ellipses. This relationship was validated by solving families of safety ellipse transfers using convex optimization. The numerical analysis also provided strong evidence that satisfying the necessary conditions results in a globally optimal solution. Analytic analysis was conducted to determine the passive safety of transfer

trajectories that result from incomplete maneuver sequences. It was shown that across the various reconfiguration scenarios, nearly all transfer trajectories meet the requirements for passive safety (the exception being phasing scenarios that call for large phase angle changes). Off-nominal scenarios were analyzed using Monte Carlo methods. The Monte Carlo simulations showed that the nominal reconfiguration analysis is a good approximation for cases where the off-nominal corrections are small relative to the nominal reconfiguration. A number of test cases involving practical reconfigurations showed that the maneuver sequences remained optimal and generated passively safe transfer trajectories.

The maneuver sequences were then tested within a nonlinear orbit environment. The simulation introduced modeling, conversion, and finite-thrust errors to reconfiguration scenarios that previously considered HCW motion and impulsive control authority. A targeting algorithm implemented the maneuver sequence to generate waypoints along a reference transfer trajectory. Analytic guidance laws were then used to compute closed-loop, finite-thrust maneuvers between each waypoint. Safety ellipse resizing and phasing scenarios for both LEO and GEO environments were analyzed using Monte Carlo methods. The performance of the guidance system was directly related to how closely the orbit environment resembled HCW motion. In general, low-eccentricity target orbits with relatively weak perturbations saw the best performance (i.e., reconfigurations in GEO). This analysis highlighted areas for improvement with the inertial-to-relative conversion process as well as general relative motion modeling.

12.2 Future Work

Like most research problems, this work has revealed areas of further interest and potential improvement. The following section discusses some of these ideas.

Additional Analytic Maneuver Sequences

An intriguing question is whether a general closed-form solution exists that satisfies the necessary conditions when the current general maneuver sequence becomes suboptimal. Ideally, the primer vector associated with this hypothetical solution would hold for the con-

ditions opposite to equation (5.109), which would effectively "fill in" the current suboptimal regions in Figures 7.2, 8.2, 9.2, and 10.2.

Characteristics of the general maneuver sequence that were first proposed and later shown to satisfy the necessary conditions were initially observed in SOCP solutions to various safety ellipse reconfiguration problems. Figure B.1 in Appendix B shows the normalized time history of the Δv magnitude from the SOCP solution for two nominal resizing cases; the top plot is a case where the maneuver sequence is optimal, and the bottom plot is a case where it is suboptimal. The top plot shows three distinct impulses separated by a half-orbit period. The bottom plot, however, shows a distribution of impulses near the times of the three-impulse solution. This suggests that simply repeating the process of inferring solution characteristics using numerical results is much more challenging for cases in which the current maneuver sequence is suboptimal.

The bottom plot of Figure B.1 is also puzzling considering that Neustadt [69] along with Potter and Stern [70] showed that the maximum number of impulses along an optimal transfer is equal to the number of constraints on the state variables at the final time. Thus the maximum number of impulses for any safety ellipse transfer is six. However, the bottom plot of Figure B.1 shows well over six impulses. This seems to imply that for certain safety ellipse transfers cast as parameter optimization problems, the solution is not unique.

Global Optimality

In Section 4.1.2, it was shown that when the maneuver sequence satisfies the primer vector conditions, it also satisfies the free-time necessary conditions. However, these conditions are only necessary. Known sufficient conditions for global optimality have been developed for impulsive linear systems by Prussing [71] and Carter [72], but these proofs rely on the assumption that the final state is fixed. Some of the terminal constraint function in problem (4.3) either vary with time, are non-convex, or both. During the numerical validation process, the fixed final time was set to multiple orbit periods to emulate the free-time problem. Increasing the final time did not affect the total Δv, providing empirical evidence of global optimality. However, it would be beneficial to prove this mathematically.

Higher Fidelity Maneuver Sequences

To improve the applicability of the general maneuver sequence, a dynamics model with improved accuracy over the HCW equations could be considered. However, one must also consider the trade-off between complexity and added value. One approach would be to keep the problem formulated in term of relative motion and incorporate a higher-fidelity model that maintains linear dynamics. For example, the relative motion model used for Chernick and D'Amico's [45] guidance laws can account for the secular effects of some differential perturbations as well as the effects of an eccentric target orbit. Another approach would be to maintain the assumption of Keplerian motion, but formulate the problem in terms of inertial dynamics. This approach has the added complication of describing arbitrary safety ellipses in terms of inertial orbital elements. With either approach, one advantage is that the current solution provides a good starting point. However, moving beyond HCW motion quickly increases the complexity of the problem and subsequently complicates the development and analysis of any analytic solution.

Closed-Loop Guidance Improvements

The results of Chapter 11 indicated that the performance of the closed-loop guidance system was dependent on how closely the orbit environment resembled HCW motion. Without affecting the two-impulse guidance framework, one approach for improving accuracy is implementing a higher-fidelity (but still linear) dynamics model. That way, the motion between each waypoint is more accurately modeled. An incremental improvement over HCW motion would be the Yamanaka-Ankersen [73] model that describes unperturbed relative motion about an elliptical orbit.

The guidance system would also benefit from an improved conversion from inertial to linearized relative states. One approach would be to use D'Amico's ROEs as a conversion tool. These ROEs are directly related to the inertial orbital elements. There also exists a linear mapping from the ROEs to the relative position and velocity for near-circular orbits [15]. Additionally, the ROEs can be written in terms of mean orbital elements, which mitigates short and long-period oscillations due to differential gravity model perturbations.

REFERENCES

[1] Goodman, J., "History of Space Shuttle Rendezvous," Tech. rep., NASA JSC-63400, 2011.

[2] Labourdette, P., Julien, E., Chemama, F., and Carbonne, D., "ATV Joules Verne Mission Maneuver Plan," *21st International Symposium on Spaceflight Dynamics*, Toulouse, France, 2009.

[3] Miotto, P., Breger, L., Mitchell, I., and Ke, B., "Designing and Validating Proximity Operations Rendezvous and Approach Trajectories for the Cygnus Mission," *AIAA Guidance, Navigation, and Control Conference*, Toronto, Ontario, August 2010, AIAA 2019-8446.

[4] D'Amico, S., Ardaens, J.-S., Gaias, G., Benninghoff, H., Schlepp, B., and Jrgensen, J. L., "Nooncooperative Rendezvous Using Angles-Only Optical Navigation: System Design and Flight Results," *Journal of Guidance, Control, and Dynamics*, Vol. 36, No. 6, 2013, pp. 1576–1595.

[5] Gaias, G. and Ardaens, J.-S., "Design Challenges and Safety Concept for the AVANTI Experiment," *Acta Astronautica*, Vol. 123, 2016, pp. 409–419.

[6] Gaias, G. and Ardaens, J.-S., "Flight Demonstration of Autonomous Noncooperative Rendezvous in Low Earth Orbit," *Journal of Guidance, Control, and Dynamics*, Vol. 41, No. 6, 2018, pp. 1137–1154.

[7] Vavrina, M. A., Skelton, C. E., DeWeese, K. D., Naasz, B. J., Gaylor, D. E., and D'Souza, C., "Safe Rendezvous Trajectory Design for the Restore-L Mission," *AAS/AIAA Spaceflight Mechanics Meeting*, Kaanapali, HI, 2019, AAS-19-410.

[8] Breger, L. S. and How, J. P., "Safe Trajectories for Autonomous Rendezvous of Spacecraft," *Journal of Guidance, Control, and Dynamics*, Vol. 31, No. 5, 2008, pp. 1478–1489.

[9] A. Richards, T. Schouwenaars, J. P. H. and Feron, E., "Spacecraft Trajectory Planning with Avoidance Constraints using Mixed-integer Linear Programming," *Journal of Guidance, Control, and Dynamics*, Vol. 25, No. 4, 2002, pp. 755–764.

[10] Tillerson, M., Inalhan, G., and How, J., "Coordination and Control of Distributed Spacecraft Systems Using Convex Optimization Techniques," *Internation Journal of Robust Nonlinear Control*, Vol. 12, No. 1, 2002, pp. 207–242.

[11] Liu, X., *Autonomous Trajectory Planning by Convex Optimization*, Ph.D. thesis, Iowa State University, 2013.

[12] Ortolano, N., *Autonomous Trajectory Planning for Satellite RPO and Safety of Flight Using Convex Optimization*, Ph.D. thesis, Utah State University, 2018.

[13] Hill, G. W., "Researches in Lunar Theory," *American Journal of Mathematics*, Vol. 1, 1878, pp. 5–26.

[14] Clohessy, W. H. and Wiltshire, R. S., "Terminal Guidance System for Satellite Rendezvous," *Journal of the Aerospace Sciences*, Vol. 27, No. 9, 1960, pp. 653–658.

[15] Joshua Sullivan, S. G. and D'Amico, S., "Comprehensive Survey and Assessment of Spacecraft Relative Motion Dynamics Models," *Journal of Guidance, Control, and Dynamics*, Vol. 40, No. 8, Aug. 2017, pp. 1837–1859.

[16] Prussing, J. E., "Optimal Four-Impulse Fixed-Time Rendezvous in the Vicinity of a Circular Orbit," *AIAA Journal*, Vol. 7, 1969, pp. 928–935.

[17] Prussing, J. E., "Optimal Two- and Three-Impulse Fixed-Time Rendezvous in the Vicinity of a Circular Orbit," *AIAA Journal*, Vol. 8, 1970, pp. 1211–1228.

[18] Jezewski, D. J. and Donaldson, J. D., "An Analytic Approach to Optimal Rendezvous Using the Clohessy-Wiltshire Equations," *Journal of the Astronautical Sciences*, Vol. 27, No. 3, 1979, pp. 293–310.

[19] Jezewski, D. J., "Primer Vector Theory Applied to the Linear Relative-Motion Equations," *Optimal Control Applications and Methods*, Vol. 1, No. 4, 1980, pp. 387–401.

[20] Carter, T. E., "Optimal Impulsive Spacecraft Trajectories Based on Linear Equations," *Journal of Optimization Theory and Applications*, Vol. 70, No. 2, 1991, pp. 277–297.

[21] Ichimura, Y. and Ichikawa, A., "Optimal Impulsive Relative Orbit Transfer Along a Circular Orbit," *Journal of Guidance, Control, and Dynamics*, Vol. 31, No. 4, 2008, pp. 1014–1027.

[22] Woffinden, D., *Angles-Only Navigation for Autonomous Orbital Rendezvous*, Ph.D. thesis, Utah State University, 2008.

[23] Flores-Abad, A., Ma, O., Pham, K., and Ulrich, S., "A Review of Space Robotics Technologies for On-Orbit Servicing," *Progress in Aerospace Sciences*, Vol. 68, 2014, pp. 1–26.

[24] Davis, J. P., Mayberry, J. P., and Penn, J. P., "On-orbit Dervicing: Inspection, Repair, Refuel, Upgrade, and Assembly of Satellites in Space," Tech. rep., The Aerospace Corporation Center for Space Policy and Strategy, 2019.

[25] Reed, B. J., Smith, R. C., Naasz, B., Pellegrino, J., and Baron, C., "The Restore-L Servicing Mission," *AIAA SPACE Forum*, Long Beach, CA, 13-16 Sep. 2016, AIAA 2016-5478.

[26] Roesler, G., "Robotic Servicing of Geosynchronous Satellites (RSGS) Program Overview," *Future In-Space Operations (FISO) Colloquium, DARPA*, June 2016.

[27] Biesbroek, R., Innocenti, L., Wolahan, A., and Serrano, S. M., "e.Deorbit–ESA's Active Debris Removal Mission," *Proceedings of the 7th European Conference on Space Debris*, Darmstadt, Germany, 18-21 April 2017, published by the ESA Space Debris Office.

[28] Alfriend, K. T., Vadali, S. R., Gurfil, P., How, J. P., and Breger, L. S., *Spacecraft Formation Flying: Dynamics, Control, and Navigation*, Oxford, U. K.: Elsevier, 2009.

[29] Karlgaard, C. D. and Lutze, F. H., "Second-Order Relative Motion Equations," *Journal of Guidance, Control, and Dynamics*, Vol. 26, No. 1, 2003, pp. 41–49.

[30] Geller, D. K. and Lovell, T. A., "Relative Orbital Motion and Angles-Only Relative State Observability in Cylindrical Coordinates," *Proceedings of the AAS-AIAA Space Flight Mechanics Meeting*, Santa Fe, NM, Jan, 2014, AAS-2014-211.

[31] Fehse, W., *Automated Rendezvous and Docking of Spacecraft*, Cambridge University Press, Cambridge, U.K., 2003.

[32] Montenbruck, O., Kirschner, M., D'Amico, S., and Bettadpur, S., "E/I-Vector Separation for Safe Switching of the GRACE Formation," *Aerospace Science and Technology*, Vol. 10, No. 7, 2006, pp. 628–635.

[33] D'Amico, S. and Montenbruck, O., "Proximity Operations of Formation-Flying Spacecraft Using an Eccentricity/Inclination Vector Separation," *Journal of Guidance, Control, and Dynamics*, Vol. 29, No. 3, 2006, pp. 554–563.

[34] Naasz, B., "Safety Ellipse Motion with Course Sun Angle Optimization," *NASA GSFC Flight Mechanics Symposium, Greenbelt, MD*, 2005.

[35] Gaylor, D. E. and Barbee, B. W., "Algorithms for Safe Spacecraft Proximity Operations," *AAS/AIAA Spaceflight Mechanics Meeting*, Sedona, AZ, 2007, AAS-2007-107.

[36] Barbee, B. W., Carpenter, J. R., Heatwole, S., Markley, F. L., Moreau, M., Naasz, B. J., and Eeepoel, J. V., "A Guidance and Navigation Stragety for Rendezvous and Proximity Operations with a Noncooperative Spacecraft in Geosynchronous Orbit," *The Journal of the Astronautical Sciences*, Vol. 58, No. 3, 2011, pp. 389–408.

[37] Curtis, H. D., *Orbital Mechanics for Engineering Students*, Butterworth-Heinemann, UK, 2009.

[38] Greenwood, D. T., *Principles of Dynamics*, Prentice-Hall, Englewood Cliffs, NJ, 1965.

[39] Spencer, D., *Automoated Trajectory Control for Proximity Operations Using Relative Orbital Elements*, Ph.D. thesis, Georgia Institute of Technology, 2015.

[40] Spencer, D. and Lovell, T. A., "Maneuver Design Using Relative Orbital Elements," *Journal of the Astronautical Sciences*, Vol. 62, 315-350.

[41] Lovell, T. A. and Tragesser, S. G., "Guidance for Relative Motion of Low Earth Orbit Spacecraft Based on Relative Orbit Elements," *AIAA/AAS Astrodynamics Specialist Conference and Exhibit*, 2004, AIAA 2004-4988.

[42] Lovell, T. A., Tragesser, S. G., and Tollefson, M. V., "A Practical Guidance Methodology for Relative Motion of LEO Spacecraft Based on the Clohessy-Wiltshire Equations," *Advances in the Astronautical Sciences*, Vol. 119, 2005.

[43] Carter, T. E. and Brient, J., "Fuel-Optimal Rendezvous for Linearized Equations of Motion," *Journal of Guidance, Control, and Dynamics*, Vol. 15, No. 6, 1992, pp. 1411–1416.

[44] Carter, T. E. and Brient, J., "Linearized Impulsive Rendezvous Problem," *Journal of Optimization Theory and Applications*, Vol. 86, No. 3, 1995, pp. 553–584.

[45] Chernick, M. and D'Amico, S., "New Closed-Form Solutions for Optimal Impulsive Control of Spacecraft Relative Motion," *Journal of Guidance, Control, and Dynamics*, Vol. 41, No. 2, 2018, pp. 301–319.

[46] Gaias, G. and D'Amico, S., "Impulsive Maneuvers for Formation Reconfiguration Using Relative Orbital Elements," *Journal of Guidance, Control, and Dynamics*, Vol. 38, No. 6, 2015, pp. 1036–1049.

[47] Wang, J., Zhang, J., Cao, X., and Wang, F., "Optimal Satellite Formation Reconfiguration Strategy Based on Relative Orbital Elements," *Acta Astronautica*, Vol. 76, 2012, pp. 99–114.

[48] D'Amico, S., *Autonomous Formation Flying in Low Earth Orbit*, Ph.D. thesis, Delft University of Technology, 2010.

[49] Carter, T. and Humi, M., "Clohessy-Wiltshire Equations Modified to Include Quadratic Drag," *Journal of Guidance, Control, and Dynamics*, Vol. 25, No. 6, 2002, pp. 1058–1063.

[50] Chamberlin, J. A. and Rose, J. T., "Gemini Rendezvous Program," *Journal of Spacecraft and Rockets*, Vol. 1, No. 1, 1964, pp. 13–18.

[51] Lovell, T. A. and Spencer, D. A., "Relative Orbital Elements Formulation Based upon the Clohessy-Wiltshire Equations," *Journal of Astronautical Sciences*, Vol. 61, Dec. 2014, pp. 341–366.

[52] Ortolano, N. and Geller, D., "Optimal Maneuvers for Safe RPO based on Relative Orbital Elements," *Proceedings of the IWSCFF Conference*, Boulder, CO 2017, IWSCFF 17-54.

[53] Athans, M. and Falb, P. L., *Optimal Control: An Introduction to the Theory and its Applications*, chap. 5, Dover, 2007, pp. 350–351.

[54] Bryson, A. E. and Ho, Y. C., *Applied Optimal Control*, Blaisdell Publishing Co., 1969.

[55] Roscoe, C. W. T., Westphal, J. J., Griesbach, J. D., and Schaub, H., "Formation Establishment and Reconfiguration Using Differential Elements in J2-Perturbed Orbits," *Journal of Guidance, Control, and Dynamics*, Vol. 38, No. 9, Sep. 2015, pp. 1725–1740.

[56] Lawden, D. F., *Optimal Trajectories for Space Navigation*, Butterworths, London, 1963.

[57] Neustadt, L. W., "A General Theory of Minimum-Fuel Space Trajectories," *J. SIAM Control*, Vol. 3, No. 2, 1965, pp. 317–356.

[58] Rishel, R. W., "An Extended Pontryagin Principle for Control Systems Whose Control Laws Contain Measures," *J. SIAM Control*, Vol. 2, No. 2, 1965, pp. 191–205.

[59] Prussing, J. E. and Chiu, J.-H., "Optimal Multiple-Impulse Time-Fixed Rendezvous Between Circular Orbits," *Journal of Guidance, Control, and Dynamics*, Vol. 9, No. 1, 1986, pp. 17–22.

[60] Boyd, S. and Vandenberghe, L., *Convex Optimization*, Cambridge University Press, 2004.

[61] Grant, M. and Boyd, S., "CVX: Matlab Software for Disciplined Convex Programming, version 2.1," http://cvxr.com/cvx, March 2014.

[62] Tutuncu, R. H., Toh, K. C., and Todd, M. J., "SDPT3– a MATLAB Software Package for Semidefinite-Quadratic-Linear Programming, version 3.0," http://www.math.cmu.edu/~reha/Pss/guide3.0.pdf, Aug. 2001.

[63] Liu, X. and Lu, P., "Solving Nonconvex Optimal Control Problems by Convex Optimization," *Journal of Guidance, Control, and Dynamics*, Vol. 37, No. 3, 2014, pp. 750–765.

[64] Alizadeh, F. and Goldfarb, D., "Second-Order Cone Programming," *Mathematical Programming*, Vol. 95, 2003, pp. 3–51.

[65] Vallado, D. A., *Fundamentals of Astrodynamics and Applications*, chap. 6, Microcosm Press, 2007, p. 413.

[66] Battin, R. H., *An Introduction to the Mathematics and Methods of Astrodynamics*, AIAA Educational Series, 1999.

[67] Montenbruck, O. and Gill, E., *Satellite Orbits: Models, Methods, and Applications*, Springer, 2011.

[68] *U.S. Standard Atmosphere*, U.S. Government Printing Office, Washington, D.C., 1976.

[69] Neustadt, L. W., "Optimization, A Moment Problem, and Nonlinear Programming," *J.SIAM Control*, Vol. 2, No. 1, 1964, pp. 33–53.

[70] Potter, J. E. and Stern, R. G., "Optimization of Midcourse Velocity Corrections," *Proceedings of the IFAC Symposium on Automatic Control in the Peaceful Uses of Space*, Vol. 2, No. 1, 1965, pp. 70–84.

[71] Prussing, J. E., "Optimal Impulsive Linear Systems: Sufficient Conditions and Maximum Number of Impulses," *The Journal of the Astronautical Sciences*, Vol. 43, No. 2, 1995, pp. 195–206.

[72] Carter, T. E., "Necessary and Sufficient Conditions for Optimal Impulsive Rendezvous with Linear Equations of Motion," *Dynamics and Control*, Vol. 10, No. 3, 2000, pp. 219–227.

[73] Yamanaka, K. and Ankersen, F., "New State Transition Matrix for Relative Motion on an Arbitrary Elliptical Orbit," *Journal of Guidance, Control, and Dynamics*, Vol. 25, No. 1, 2002, pp. 60–66.

APPENDICES

APPENDIX A

Transfer Trajectory Passive Safety

Section 3.2 shows that, assuming the safety ellipse is periodic or near-periodic, the angle γ provides a measure of its passive safety. This section presents a more general description of passive safety for any HCW-based relative motion trajectory with non-zero out-of-plane motion.

The variable d is defined as the smaller radial separation between the in-track axis and point of relative nodes:

$$d := \left| \frac{1}{2}a|\cos\gamma| - |x_r| \right| \tag{A.1}$$

The geometry of equation (A.1) is shown in Figure A.1.

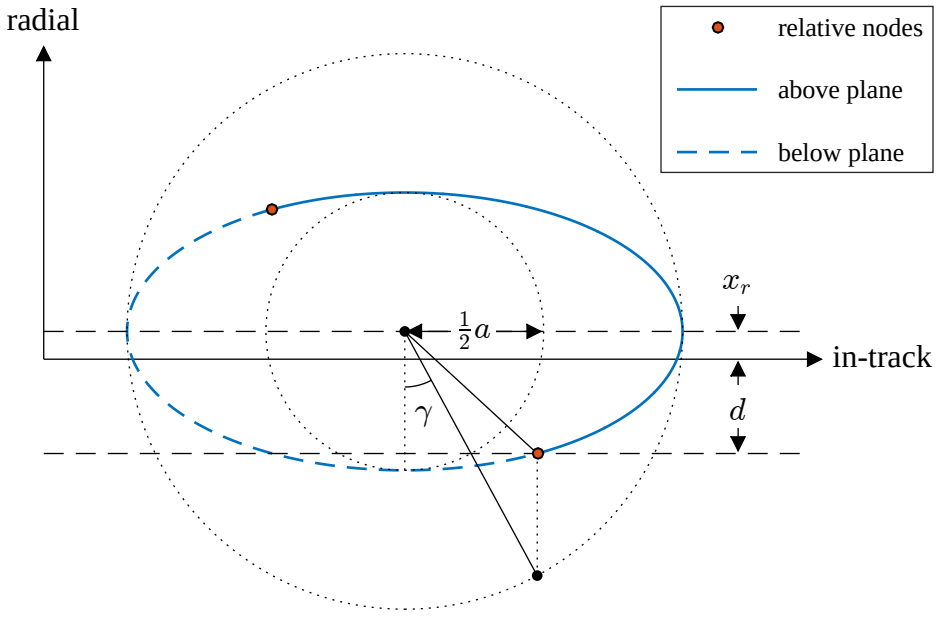

Fig. A.1: Geometry of the general passive safety parameter, d.

The passive safety margin is proportional to d, with a larger d indicating a larger passive safety margin. As d decreases, the chaser moves closer to intersecting the in-track

axis rather than passing above or below it. This can lead to an unsafe scenario depending on where the chaser intersects the in-track axis. Note that for a (near) periodic safety ellipse ($x_r \approx 0$), equation (A.1) indicates that d is maximized when $\gamma = \gamma^{\text{ideal}}$.

Figures A.2 and A.3 show a transfer trajectory where $\gamma = 180^\circ$ but d is small. A spherical keep-out zone centered about the origin of the LVLH frame represents a collision safety factor for the target spacecraft. The portion of the trajectory shown in red denotes where the chaser passes through the keep-out zone.

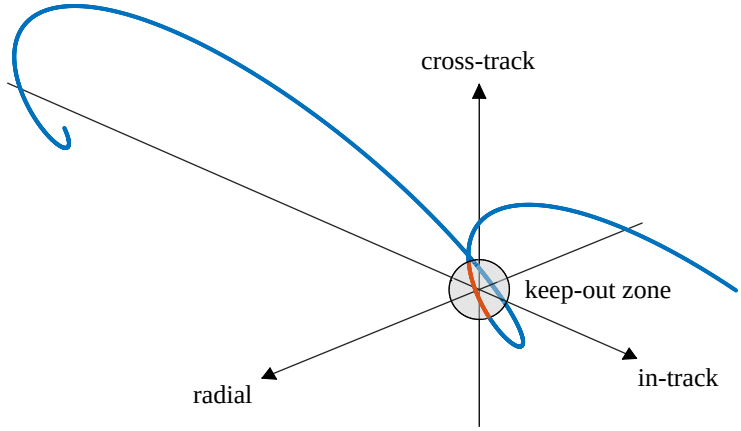

Fig. A.2: Example of an unsafe transfer trajectory.

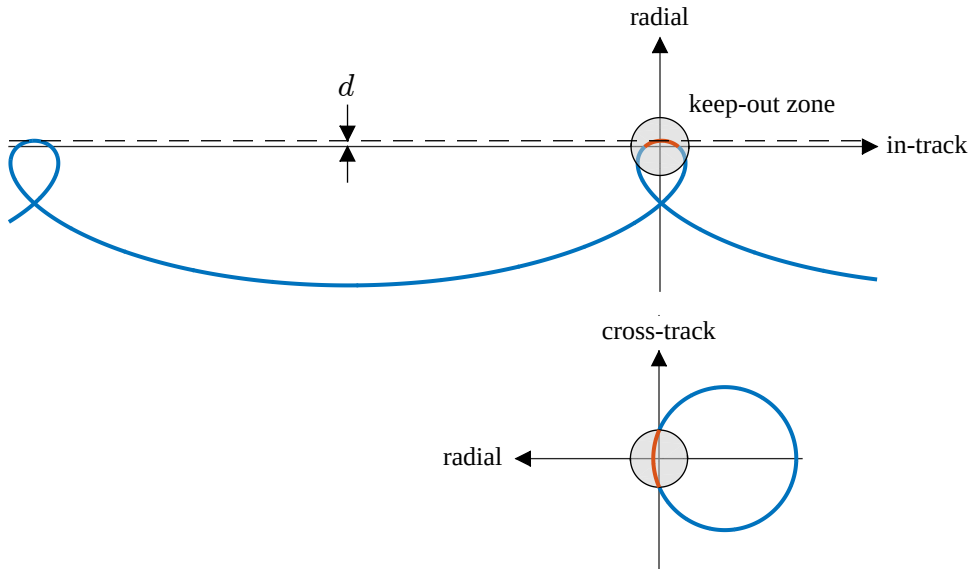

Fig. A.3: Radial, in-track and radial, cross-track projections of the unsafe trajectory.

APPENDIX B

Examples of SOCP Solutions

In this work, formulating and solving SOCPs is an essential tool for both validation and analysis. This section provides a brief look at the control profiles generated by the SOCP solver for two nominal safety ellipse resizing cases (see Section 7.2.2). The general trends shown here are identical for the other nominal reconfiguration scenarios.

Figure 7.2 plots the contours representing the ratio of the SOCP-optimal Δv to the analytic Δv as a function of γ_0 and $\Delta A/\Delta a$. Each point in $(\gamma_0, \Delta A/\Delta a)$ space represents a nominal resizing case. Figure B.1 shows the resulting Δv profile for two of these $(\gamma_0, \Delta A/\Delta a)$ pairs. The initial conditions used to generate Figures B.1 are: $\tau_0 = 0$, $a_0 = 1\,\text{km}$, $A_0 = 0.5\,\text{km}$, $\gamma_0 = 45°$, and $\psi_0 = -90°$. The dimensions of the final safety ellipse are $a_f = 0.5\,\text{km}$ and $A_f = 0.15\,\text{km}$ for the upper plot, and $a_f = 0.5\,\text{km}$ and $A_f = 0.25\,\text{km}$ for the lower plot. The results are consistent with the contours of Figure 7.2.

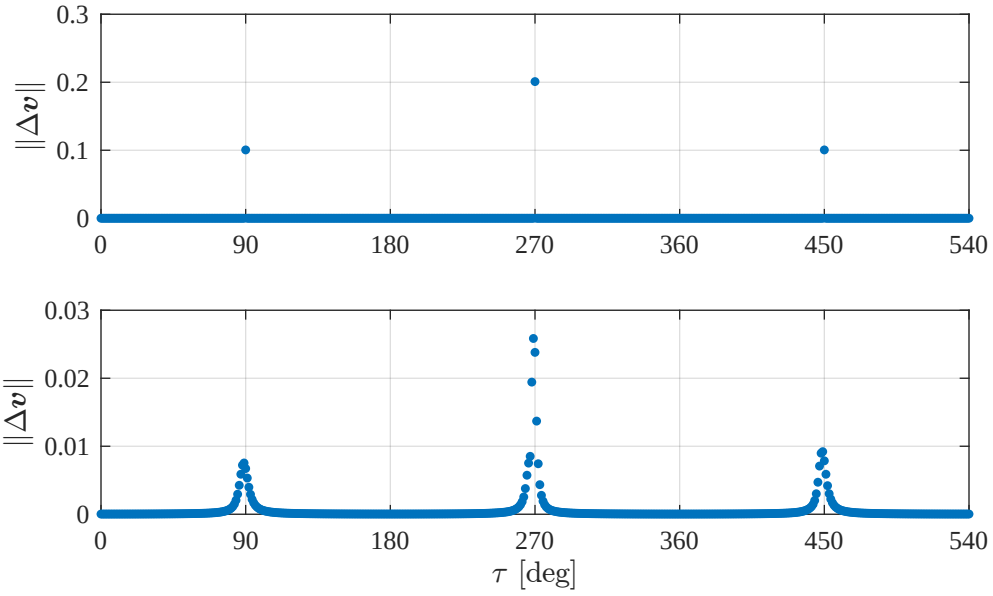

Fig. B.1: Δv as a function of τ for nominal resizing scenarios where $\gamma_0 = 45°$, $\Delta A/\Delta a = 0.7$ (top) and $\gamma_0 = 45°$, $\Delta A/\Delta a = 0.5$ (bottom).

CURRICULUM VITAE

Simon Shuster

Journal Articles

- **S. Shuster**, D. Geller, M. Harris "An Analytic Maneuver Sequence for Safety Ellipse Reconfigurations Using Relative Orbital Elements," Journal of Guidance, Control, and Dynamics, submitted.
- **S. Shuster**, D. Geller, M. Harris "Analytic Impulsive Maneuver Sequences for Nominal Safety Ellipse Reconfigurations," Journal of Guidance, Control, and Dynamics, Vol. 43, No. 10, Oct 2020, pp. 1837-1853.

Conference Papers

- **S. Shuster**, D. Geller, "An Analytic Guidance Law for Safety Ellipse Reconfigurations," AAS 20-148, AAS Guidance, Navigation, and Control Conference, Breckenridge, CO, February, 2020.
- N. Stastny, D. Geller, **S. Shuster**, "Optimal Relative Trajectory Design with Mission Constraints and Performance Requirements," AAS 20-138, AAS Guidance, Navigation, and Control Conference, Breckenridge, CO, February, 2020.
- **S. Shuster**, "Development and Analysis of NRHO Rendezvous Reference Trajectories Using Convex Optimization," AAS 19-014, AAS Guidance, Navigation, and Control Conference, Breckenridge, CO, February, 2019.
- **S. Shuster**, D. Geller, T. Smith, "A Performance Analysis of On-board Numerical Propgators," AAS 18-092, AAS Guidance, Navigation, and Control Conference, Breckenridge, CO, February, 2018.

- **S. Shuster**, A. Sinclair, T. A. Lovell, "Initial Relative Orbit Determination Using Heterogeneous TDOA," IEEE Aerospace Conference, Big Sky, MT, March, 2017.

- **S. Shuster**, A. Sinclair, T. A. Lovell, "Uncertainty Analysis for Initial Relative Orbit Determination Using Time Difference of Arrival Measurements," AAS 17-012, AAS Guidance, Navigation, and Control Conference, Breckenridge CO, February, 2017.